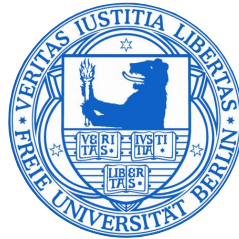


The Electronic Structure of Fluorinated Systems in the Liquid Phase

Dissertation



HZB Helmholtz
Zentrum Berlin

im
Fachbereich Physik
der Freien Universität Berlin
eingereichte Dissertation

zur Erlangung des akademischen Grades
eines Doktors der Naturwissenschaften (Dr. rer. nat.)

vorgelegt von

Tim Brandenburg

Berlin
August 2016

Gutachter (Appointed Examiners):

Erstgutachter (First Examiner):

Prof. Dr. Emad Flear Aziz

Institute Director of *Methods for Material Development*, Helmholtz-Zentrum Berlin

&

Professor at the Department of Physics

Freie Universität Berlin, Germany

Zweitgutachter (Second Examiner)

Prof. Dr. Jan-Erik Rubensson

Professor at Department of Physics and Astronomy, *Molecular and Condensed Matter Physics*

Uppsala University, Sweden

Tag der Disputation (Day of Disputation): 19.01.2017

Contents

Abstract

1	Preface	1
2	Introduction	3
3	Theoretical Introduction	7
3.1	X-Ray Spectroscopy	7
3.1.1	X-Ray Interaction with Matter	7
3.1.2	X-Ray Absorption	11
3.1.3	X-Ray Emission	12
3.1.4	Resonant Inelastic X-Ray Scattering	13
3.2	Theoretical Model Calculations	15
4	Experimental Methods and Instrumentation	17
4.1	Synchrotron Radiation	17
4.1.1	Basics of Synchrotron Radiation	17
4.1.2	Principle Sources of Synchrotron Radiation	19
4.1.3	Synchrotrons	24
4.2	Liquid Measurements and X-Ray Spectroscopy Techniques	29
4.2.1	Drop between two Membranes	29
4.2.2	Liquid Flow Cell	31
4.2.3	Liquid Microjet	32
4.2.4	Rowland Circle and X-Ray Emission	33
4.2.5	Experimental Setup: LiXEdrom	34
4.2.6	Experimental Setup: Transmission Flow Cell	35
5	Data Presentation and Discussion	37
5.1	Highly Fluorinated Materials	37

5.1.1	The Perfluoro Effect	38
5.1.2	Perfluorinated Liquids	38
5.2	Chain-Shaped Hydro- and Perfluorocarbons	43
5.3	Non-Aromatic Ring-Shaped Hydro- and Perfluorocarbons	63
5.3.1	Decalin and Perfluorodecalin	63
5.3.2	Cyclo-Hexane and Perfluoro-Cyclo-Hexane	77
5.4	Aromatic Ring-Shaped Hydro- and Perfluorocarbons	87
5.4.1	Benzene and Perfluorobenzene	87
5.4.2	Naphthalene and Perfluoronaphthalene	97
5.5	Methylated Ring-Shaped Hydro- and Perfluorocarbons	107
6	Summary and Conclusions	117
7	Outlook	121
	Bibliography	i
8	Appendix	xi
8.1	Benzene Calculations with Different Parameter Configurations . . .	xi
8.2	Supplementary Materials from the Contributed Articles	xiii
8.2.1	Impacts of Conformational Geometries in Fluorinated Alkanes	xiii
8.2.2	Fluorination-Dependent Molecular Orbital Occupancy in Ring-Shaped Perfluorocarbons	xv
8.2.3	The Electronic Structure of Perfluorodecalin studied by Soft X-Ray Spectroscopy and Electronic Structure Calculations	xx
	Acknowledgments	xxiii

List of Figures

2.1	Liquid Breathing	5
3.1	Schematic representation of Electron Promotion and Demotion Processes through X-Ray Radiation	12
4.1	Radiation Patterns of Synchrotron Radiation Principle Sources	21
4.2	Schematics of the U41-PGM and BL3U Beamline and its Elements	27
4.3	Schematics of Liquid X-Ray Absorption Methods	30
4.4	Rowland Circle Diffraction Geometry	34
4.5	Schematic of the LiXEdrom and Transmission Cell Setup	36
5.1	Schematic Representation of all Investigated Samples	40
5.2	Carbon K-edge Absorption for Hydro- and Perfluoroalkanes	44
5.3	Table Representation of the Alkane Molecular Orbitals	46
5.4	Carbon K-edge Absorption: Perfluoro Effect for Hydro- and Perfluoroalkanes	47
5.5	Carbon K-edge Emission for Hydro- and Perfluoroalkanes	49
5.6	Carbon K-edge Emission: Perfluoro Effect for Hydro- and Perfluoroalkanes	51
5.7	Carbon K-edge RIXS for Hydroalkanes	54
5.8	Carbon K-edge RIXS for Perfluoroalkanes	56
5.9	Fluorine K-edge Data for Perfluoroalkanes	59
5.10	Fluorine K-edge RIXS for Perfluoroalkanes	60
5.11	Carbon K-edge Absorption for Decalin and Perfluorodecalin	64
5.12	Carbon K-edge Emission for Decalin and Perfluorodecalin	68
5.13	Carbon K-edge RIXS for Decalin	70
5.14	Carbon K-edge RIXS for Perfluorodecalin	72
5.15	Fluorine K-edge RIXS for Perfluorodecalin	74

5.16	Carbon K-edge Absorption for Cyclo-Hexane and Perfluoro-Cyclo-Hexane	78
5.17	Carbon K-edge Emission for Cyclo-Hexane and Perfluoro-Cyclo-Hexane	81
5.18	Fluorine K-edge Data for Perfluoro-Cyclo-Hexane	85
5.19	Carbon K-edge Absorption for Benzene and Perfluorobenzene	88
5.20	Carbon K-edge Emission for Benzene and Perfluorobenzene	90
5.21	Fluorine K-edge Data for Perfluorobenzene	94
5.22	Carbon K-edge Absorption for Naphthalene and Perfluoronaphthalene:	98
5.23	Carbon K-edge Emission for Naphthalene and Perfluoronaphthalene	100
5.24	Fluorine K-edge Data for Perfluoronaphthalene	104
5.25	Carbon K-edge Absorption for Methylated-Ring Perfluorocarbons	108
5.26	Carbon K-edge Emission for Methylated-Ring Perfluorocarbons	112
5.27	Fluorine K-edge Data for Methylated-Ring Perfluorocarbons	115
8.1	Benzene Calculations with Different Parameter Configurations	xii
8.2	Impacts of Conformational Geometries - Sup 1	xiii
8.3	Impacts of Conformational Geometries - Sup 2	xiv
8.4	Fluorination-Dependent Molecular Orbital Occupancy in Ring-Shaped Perfluorocarbons - Sup 1	xv
8.5	Fluorination-Dependent Molecular Orbital Occupancy in Ring-Shaped Perfluorocarbons - Sup 2	xvi
8.6	Fluorination-Dependent Molecular Orbital Occupancy in Ring-Shaped Perfluorocarbons - Sup 3	xvii
8.7	Fluorination-Dependent Molecular Orbital Occupancy in Ring-Shaped Perfluorocarbons - Sup 4	xviii
8.8	Fluorination-Dependent Molecular Orbital Occupancy in Ring-Shaped Perfluorocarbons - Sup 5	xix
8.9	The Electronic Structure of Perfluorodecalin studied by Soft X-Ray Spectroscopy and Electronic Structure Calculations - Sup 1	xx
8.10	The Electronic Structure of Perfluorodecalin studied by Soft X-Ray Spectroscopy and Electronic Structure Calculations - Sup 2	xxi
8.11	The Electronic Structure of Perfluorodecalin studied by Soft X-Ray Spectroscopy and Electronic Structure Calculations - Sup 3	xxii

List of Tables

3.1	Energetic Region Table	7
5.1	Perfluoroalkane XA Carbon K-edge Character Table	48
5.2	Perfluoroalkane XE Carbon K-edge Character Table	52
5.3	Perfluorodecalin XA Carbon K-edge Character Table	66
5.4	Perfluorodecalin XE Carbon K-edge Character Table	69
5.5	Perfluoro-Cyclo-Hexane XA Carbon K-edge Character Table . . .	79
5.6	Perfluoro-Cyclo-Hexane XE Carbon K-edge Character Table . . .	82
5.7	Perfluorobenzene XA Carbon K-edge Character Table	89
5.8	Perfluorobenzene XE Carbon K-edge Character Table	91
5.9	Perfluoronaphthalene XA Carbon K-edge Character Table	99
5.10	Perfluoronaphthalene XE Carbon K-edge Character Table	101
5.11	Methylated-Ring Perfluorocarbons XA Carbon K-edge Character Table	109
5.12	Methylated-Ring Perfluorocarbons XE Carbon K-edge Character Table	111

List of Abbreviations

CCD	charge coupled device
cyc-hex	cyclo-hexane
dC	carbon atom with two fluorine neighbours
dF	fluorine atom bound to dC atom
DFT	density functional theory
FEL	free electron laser
FWHM	full-width at half maximum
GGA	generalised gradient-corrected approximation
HF	Hartree-Fock
HOMO	highest occupied molecular orbital
ID	insertion device
ISEELS	inner-shell electron energy loss spectroscopy
LDA	local density approximation
LUMO	lowest unoccupied molecular orbital
mC	methyl carbon atom
m-cyc-hex	methyl-cyclo-hexane
mF	fluorine atom bound to mC atom
MO	molecular orbital
naph	naphthalene
PF-Benzene	perfluorobenzene
PFC	perfluorocarbon
PF-cyc-hex	perfluoro-cyclo-hexane
PFD	perfluorodecalin
PFHep	perfluoroheptane
PFHex	perfluorohexane
PFnaph	perfluoronaphthalene
PFO	perfluorooctane
PF-toluene	perfluorotoluene
PGM	plane-grating monochromator
RF-cavity	radio-frequency cavity

RIXS	resonant inelastic X-ray scattering
sC	carbon atom with one fluorine neighbours
sF	fluorine atom bound to sC atom
SR	synchrotron radiation
TD-DFT	time dependent density functional theory
TFY	total fluorescence yield
TZVP	valence triple-zeta polarisation
VLS	variable line spacing
XA	X-ray absorption
XAS	X-ray absorption spectroscopy
XE	X-ray emission
XES	X-ray emission spectroscopy

Contributed Articles

Some chapters are part or in full published in international peer-reviewed journals. A list of the corresponding chapters and articles can be found here:

- **Brandenburg, T.**; Agaker, M.; Atak, K.; Pflüger, M.; Schwanke, C.; Petit, T.; Lange, K. M.; Rubensson, J.-E.; Aziz, E. F.: The electronic structure of perfluorodecalin studied by soft X-ray spectroscopy and electronic structure calculations. In: *Physical Chemistry Chemical Physics: PCCP* **16** (2014), Oktober, Nr. 42, 23379-23385 (Chapter 2, 5.1, 5.2 and 5.3.1)
- **Brandenburg, T.**; Petit, T.; Neubauer A.; Atak, K.; Nagasaka, M.; Golnak, R.; Kosugi, N.; Aziz, E. F.: Fluorination-dependent molecular orbital occupancy in ring-shaped perfluorocarbons. In: *Physical Chemistry Chemical Physics: PCCP* **17** (2015), Juli, Nr. 28, 18337-18343 (Chapter 2, 5.1, 5.2 and 5.3.1)
- **Brandenburg, T.**; Golnak, R.; Nagasaka, M.; Atak, K.; Sreekantan Nair Lalithambika S.; Kosugi, N.; Aziz, E. F.: Impacts of Conformational Geometries in Fluorinated Alkanes. In: *Scientific Reports: Sci. Rep.* **6** (2016), 31382 (Chapter 2, 5.1 and 5.2)

Abstract

Perfluoro systems are at the heart of research in blood substitute formulations, due to their capability of storing gases without binding them. A huge variety of applications have emerged, such as liquid breathing or tissue oxygenation, and recently, the scientific community has gained more interest in corresponding electronic structure studies.

In this work, I report on newly and previously developed concepts based on electronic structure measurements of perfluorocarbons. The focus is on the investigation of several hydrocarbons (e.g. benzene, hexane or toluene) and their respective fluorinated counterparts based on X-ray absorption (XA), X-ray emission (XE) and resonant inelastic X-ray scattering (RIXS) data. Additional time-dependent density functional theory (TD-DFT) calculations to support and assign the experimental spectra of the examined samples are performed and presented, too. The importance of the chemical and biological inertness of these studied perfluorocarbons and the possibility to extend the studies towards gas loaded systems is discussed.

I also present insights into the so-called perfluoro effect, which describes the energetic shift induced by fluorination, revealing differences regarding its rules for variations in geometrical structure and aromatic status. The observability of the perfluoro effect *via* XE spectroscopy is confirmed for the first time. My analysis that suggests the formulation of a molecular orbital (MO) transfer effect for all non-aromatic samples is discussed in this work. A "shielding" effect, leading to the inhibition of intermolecular interactions, has been discovered and is discussed with regards to possible molecular and polymer enhancement methods through fluorination. For the different chain-type perfluorocarbons, a conformation effect, resulting from different molecular conformations, is observed. This directly leads to a modification of the intermolecular interactions and helps gaining a deeper understanding of free cavities in the liquid.

For methylated perfluorocarbons I found out that, the methyl group atoms are discovered to exhibit a modulating function on the MOs, leading to a "quenching" of the previously non-methylated MOs. The benefits of discussing the carbon sites according to their number of bonded fluorine is presented. Thus, site-selective excitations are observed, which improve the understanding of the geometric and electronic structure of perfluorocarbons.

Abstract - German/Deutsch

Perfluoro-Systeme sind wegen ihrer Fähigkeiten, Gase zu speichern, ohne diese zu binden, sehr begehrt in der Blutersatzmittelforschung. Sie besitzen eine breite Anwendungspalette - von Flüssigatmung bis zu Sauerstoffanreicherung von Gewebe; wenig ist bekannt über die elektronische Struktur dieser Systeme und die wissenschaftliche Gemeinschaft zeigt starkes Interesse an systematischen Untersuchungen.

In dieser Arbeit diskutiere ich die neuesten, sowie bereits etablierten Konzepte, die auf elektronischen Strukturmessungen von Perfluorosystemen beruhen. Der Fokus liegt insbesondere auf der Untersuchung von Hydrokarbonen (z.B. Benzen, Hexan und Toluol) und deren fluorinierten Ebenbildern mittels Röntgenabsorptions- (XA), Röntgenemissions- (XE) sowie Resonanter Unelastischer Röntgenstreuungsspektroskopie (RIXS). Darüber hinaus werden TD-DFT Berechnungen präsentiert und herangezogen, um die experimentellen Spektren der untersuchten Systeme zu erklären. Die Wichtigkeit der chemischen und biologischen Inertheit der untersuchten Perfluorokarbone, sowie die Möglichkeit diese Studien auf Gas-beladene Systeme zu erweitern, wird diskutiert.

Ich präsentiere Einblicke in den sogenannten Perfluoro-Effekt, der die energetische Verschiebung durch die Fluorierung beschreibt, und diskutiere Abweichungen des Effektes für unterschiedliche geometrische Strukturen, sowie dem aromatischen Status. In dieser Arbeit ist dieser Perfluoro-Effekt erstmals mittels XES bestätigt worden. Meine Analysen zeigen auf, dass die Bildung eines Molekülorbital-Übergangseffektes für sämtliche untersuchten, nicht-aromatischen, Systeme besteht. Ein "Shield"-Effekt, der zur Unterdrückung von intermolekularen Wechselwirkungen führt, wurde entdeckt und dahingehend diskutiert, molekulare und polymere Verbesserungen durch Fluorinierung zu erreichen. Für die unterschiedlichen Ketten-Perfluorokarbone wurde ein Konformationseffekt beobachtet, der durch die vielen verschiedenen molekularen Orientierungen entsteht. Dieser Effekt führt direkt zu einer Modifizierung der intermolekularen Wechselwirkungen und damit zu einem Verständnissgewinn über Kavitäten in der Flüssigkeit.

Für methylierte Perfluorokarbone konnte ich nachweisen, dass die Atome in den Methylgruppen die Molekülorbitale dahingehend verändern, dass die vorher nicht-methylierten Molekülorbitale gestaucht werden. Die Nützlichkeit, Kohlenstoffatome bezüglich Ihrer Anzahl an Fluorbindungen zu diskutieren, wird vorgestellt. Die beobachteten ortsselektiven Anregungen helfen unser Verständnis über die geometrische und elektronische Struktur von Perfluorokarbonen zu verbessern.

1 Preface

Let me first welcome my readers with a personal note on this work and its overall process. You may skip this, as it has no implications to the official text and is purely a private message and my thoughts.

I started my work on this project with a basic scientific frame I set by myself and confirmed by the supervisor. The great idea was to compare the different primary structures of perfluorocarbons and gain an understanding of its chemical properties through this. Time revealed that my plan was shortsighted, as experimental success came one after the other, and an extension of my first idea was recommended. The primary structures, ring- and chain-shaped, can be further split into sub-species, which I noticed in the planning processes and adapted henceforth. Differences in aromatic status also delivered more depth and the primary idea developed into a sophisticated overall structure over the course of three years.

Now an experimental monster with seven sub-species was born and each species had several samples to investigate with a great variety of experimental techniques. In the end this left me with frustration, due to the sheer amount of work needed to be put into it, but also delivered great amount of joy. The external times in Japan were some of the most enjoyable events during the course of this work. It is a beautiful country and I can recommend anyone to visit for a holiday.

The overall experimental success also led to a lot of conference visits. Some highlights occurred in Chamonix, France and Rome, Italy. I am grateful for the opportunities and greatly enjoyed my visits. Therefore, let me give thanks to my supervisor for financing these visits and the big chances I had for presenting my work. Additionally, great thanks to the Japanese hosts for the opportunity to visit and experiment at their beamline.

In a nutshell, my colleagues were always helpful and I hope the help I received was offered back in similar meaningful ways. Consequently, I enjoyed my time and hope they did too.

The most undesired time was actually writing down all the processes and this work. Don't misunderstand me ... it was fun, but compared to the experimental and other times still a bit lacking in eventfulness. It also does not help to sit in front of your desk nonstop for around six months straight. I believe most of the readers will know what I'm talking about.

I hope I could give you some small insights into the three years I had while creating this work and wish you a nice time reading.

Tim

2 Introduction

Research in blood substitute formulations is gaining more attention in the scientific community in recent years [1, 2, 3, 4, 5, 6, 7, 8, 9] as more pharmaceutical companies start clinical trials on different artificial blood approaches [7, 10, 11, 12]. In general, artificial blood consists of emulsions of different liquid or protein compounds to increase oxygen solubility and transport capabilities as well as to decrease toxicity to biological tissue [7, 10]. Two of the more promising approaches centre themselves around haemoglobin-based carriers [11] and fluorinated microemulsions [6, 9]. Despite setbacks regarding clinical tests and medicinal approval of recent formulations [5, 13], an emulsion containing perfluorodecalin named Fluosol [12] was successfully approved by the U.S. Food and Drug Administration in 1989 (New Drug Application N860909).

The main oxygen carrier in Fluosol, perfluorodecalin, is part of the family of perfluorocarbons (PFC). They have a wide range of applications ranging from tissue oxygenation [1, 14, 15] to post-operative treatment [16, 17]. Their wide range of extraordinary properties - high density, high viscosity, high biological and chemical inertness, high gas solubility [18, 19] - offer opportunities for applications in biomedicine and physical chemistry [20, 21], as well as subsequently leading to a high interest in scientific development [2, 18, 19, 22, 23].

PFCs consist mainly of carbon and fluorine atoms and are synthesised from their respective hydrocarbons [22, 23, 24]. The corresponding hydrocarbons are often either harmful to humans or exhibit no biomedical interesting features [18, 24], which creates further interest in PFCs as they are mainly non-harmful and exhibit one primary trait. This trait is the ability to store and transport gases, while the PFC itself is in liquid phase [18, 19]. Earlier studies on these molecules revealed, that the gas is not chemically or physically bound to the molecule and that a different mechanism is at work [18]. Hamza *et al.* reported, that the structure of the fluid alone seems to be the predominant factor in accounting for the dissolving capacity of gases in fluorochemicals.

This trait of storing gases without binding them gave rise to the huge variety of applications and scientific interest, but is, to my knowledge, still not fully understood. Fundamental investigations on PFCs were a challenge, especially local electronic structure and far infrared measurements, because of spectrometers without an appropriate

resolution and light sources with insufficient intensity. Nonetheless, a few experimental studies based on photoelectron and X-ray absorption (XA) spectroscopy have already been performed [22, 23, 25, 26, 27], but the development of more complex theoretical models [28] and new experimental techniques [29, 30, 31] give opportunities for further investigation of perfluorocarbons. Especially the field of X-ray spectroscopy advanced significantly [29, 30], resulting in being the choice for experimental observation in this work.

Another inherent feature to all PFCs is the so called perfluoro effect, which describes the energy shifts of the spectral features due to the stabilisation impact of fluorine in the fluorination process [2, 18, 19, 22, 23]. It was discovered, that the magnitude of the energy shift can be used for a molecular orbital (MO) character classification to either bear σ - or π -character [22, 23] delivering an experimental method for orbital classification. As this effect was first publicised by Brundle *et. al.* in 1971, where several non-aromatic and aromatic hydro- and perfluorocarbons were investigated employing gas-phase photoelectron spectroscopy [22, 23], a systematic extension to different PFCs and spectroscopic methods is of high interest.

The family of PFCs is broad and only a selected few will be investigated in the frame of this work. To get a grasp on the big picture, I therefore choose to observe the X-ray absorption, emission and resonant inelastic X-ray scattering spectra of two main groups: alkanes (chain-shaped) and ring-shaped samples. These groups are then further split into their corresponding sub-groups: aromatic, non-aromatic and methylated. Consequently, all basic geometric and chemical systems are represented for low complex PFCs.

This work starts with chapter 3, where I present the theoretical background required to fully understand the presented spectroscopic and theoretical methods. Different types of light and matter interactions will be introduced and explained, while the reason behind choosing X-ray based techniques will be elaborated. A basic theoretical idea of the different X-ray based spectroscopies is introduced and the chapter is concluded with a deeper insight into the calculation model utilised for theoretical predictions.

The subsequent chapter 4 follows up with an introduction into the experimental means. The experimental creation of X-rays through synchrotron radiation will be explained and an in-depth insight of the two synchrotrons delivering experimental results in this work is provided. Consequently, the corresponding experimental end-stations are introduced and various experimental methods for X-ray measurements on liquids are demonstrated.

The discussion will be started by opening remarks on highly fluorinated materials in chapter 5.1, their specific characteristics and a small discussion on the molecules presented in this work.



Figure 2.1: **Liquid Breathing:** A mouse diving in a perfluorocarbon [32]. The mouse breathes oxygen through the perfluorocarbon liquid, demonstrating the possibility for liquid breathing and the high oxygen storing capabilities.

The first experimental data will be shown in chapter 5.2, representing three different chain-shaped fluorinated alkanes. Differences between the alkanes will be drawn and a discussion with regard to conformational geometries, the perfluoro effect, as well as their gas dissolving capacities, are discussed. Several new concepts, like a molecular orbital transfer from unoccupied to occupied region, are presented and further elaborated.

Chapter 5.3 will then extend the concepts and discoveries onto non-aromatic ring-shaped PFC systems. Several different ring-structures are discussed and contemplated on, with respect to structural differences and spectral similarities. Note that, a theoretical separation into different carbon sites is performed and found to be crucial for the subsequent discussions.

The corresponding aromatic ring-shaped counterparts are later discussed in chapter 5.4. Significant differences to the non-aromatic spectra and surprising changes in the behaviour of established concepts are going to be illustrated. The resulting changes in

analysis methodology and concept validity will also be discussed in regard to the influence of the free π electron system.

As the last data presentation part, chapter 5.5 will treat methylated samples. Ring-shaped PFCs from previous chapters, both aromatic and non-aromatic, are discussed pertaining to their added methyl group and the spectral differences towards their non-methylated counterparts. A refinement and confirmation of specific concepts was obtained, leading to a deeper insight into the relative inertness of PFCs.

The subsequent conclusions and a small summary will be found in chapter 6 with a following outlook onto possible further experiments and developments in chapter 7.

3 Theoretical Introduction

3.1 X-Ray Spectroscopy

3.1.1 X-Ray Interaction with Matter

Before talking about specific spectroscopies, a definition of the word spectroscopy and what it entails is required. In general, spectroscopy is the study of interactions between light and matter to understand the properties of a medium [33]. To accomplish this, various interactions of light and matter, when the former is traversing through the medium, are essential.

Photons of different energy ranges will interact with different systems in the medium, leading to a great variety of possible spectroscopies. Table 3.1 is summarising some of the energetic regions and their corresponding interactions to give an overview [34].

specific photon name	energy region [eV]	excited system
microwave	$1.24 \cdot 10^{-6}$ to $1.24 \cdot 10^{-3}$	spin system
infrared light	$1.24 \cdot 10^{-3}$ to 1.7	rotational and vibrational system
visible light	1.7 to 3.3	electronic system (valence band)
ultraviolet light	3.3 to 100	electronic system (valence band)
soft X-rays	100 to $6 \cdot 10^3$	electronic system (core-level)
hard X-rays	$6 \cdot 10^3$ to $100 \cdot 10^3$	electronic system (core-level)

Table 3.1: **Energetic Region Table:** Energetic regions and their corresponding interactions [34].

The delivered overview is not of finite nature, as every region is ambiguously chosen and sub-species, as well as additional sub-regions, may appear. Table 3.1 can, nonetheless,

be used to classify some of the more important photon energy domains.

If a medium is considered in a simplified quantum mechanical picture, the atoms or molecules of the medium can be said to have several discrete atomic energy levels [33, 35]. These energy levels are filled with electrons up to a certain point, above which is a small unoccupied region and the vacuum continuum (see figure 3.1).

If a photon wave of specific energy is impinging on a medium, interactions regarding the aforementioned energetic levels are bound to occur. The incoming photon can interact with the medium and excite an electron from its initial energy level to a higher one depending on the photon energy [36]. To promote the electron, the photon energy itself has to be higher or match the energy level difference. Consequently, the different energetic photon regions, as described by table 3.1, will cause transitions between different electronic states. The resulting vacancy in the medium is called a hole. In case of a core-level vacancy, one speaks of a core-hole. The now excited state of the medium will relax to fill the hole and create a response, which, e.g., can be a photon emission [33, 35, 36].

As the photon beam passes through the absorbing material, the intensity of the light decreases [35, 36]. Energy is transferred to the molecules or atoms of the absorbing material and a description for the energy loss is required. The loss in intensity over a small volume element is proportional to the initial intensity before entering the element I_0 , the absorber concentration C and the path-length l through the element [35, 37]:

$$\frac{dI}{dx} = -\epsilon l C \quad (3.1)$$

with ϵ as a proportionality constant. Through solving of the differential equation, the intensity of the transmitted light can be obtained [37]:

$$I = I_0 \cdot e^{-\epsilon l C} = I_0 \cdot 10^{-\epsilon l C} = I_0 \cdot 10^{-A} \quad (3.2)$$

where ϵ describes the molar absorption coefficient, containing the information regarding all the processes occurring between light and matter, and A as the optical density. This equation is known as the Beer-Lambert law.

X-ray spectroscopy is referring to excitations from the core-level domain of a medium and will be the focus of this dissertation. The advantage of core-level excitations is the element selectivity, as each element has specific core level energetics, different from the other elements [38, 39]. Especially the soft X-ray region is of interest, as the medium observed in this work includes core levels in the soft X-ray energy domain (more in chapter 5.1).

Up to this point, the interactions of light and matter were considered from a simple quantum mechanical point of view and should be described in more detail.

The interaction process can be described as electronic transitions in a system perturbed by electromagnetic radiation [33, 36, 40]. The systems to be considered are, e.g., atoms, ions, molecules or correlated systems like solids and liquids. The electrons in such systems are surrounded by a complicated landscape of electric and magnetic fields from the atoms, other electrons and the photon field from the electromagnetic radiation. The equations relating the electric and magnetic fields are described by Faraday's law [41, 42]:

$$\nabla \times \vec{E} = -\frac{\delta \vec{B}}{\delta t} \quad (3.3)$$

where \vec{E} is the electric and \vec{B} the magnetic field, which are governed by Maxwell's equations [42]. Under consideration of the limit $\vec{B} = 0$, equation 3.3 reforms to

$$\nabla \times \vec{E} = 0 \quad (3.4)$$

The subsequent result is: if a particle moves in a closed loop back to its original position, its energy is conserved and will not change. Utilising the vector identity $\nabla \times \nabla V = 0$, Faraday's law can be satisfied by defining $\vec{E} = -\nabla V$, where V is the potential describing the system [33, 36].

A suitable potential for the description of the magnetic field still needs to be chosen. The vector potential \vec{A} can be defined as $\vec{B} = \nabla \times \vec{A}$ under consideration of $\nabla \cdot (\nabla \times \vec{A})$ [33, 36, 43]. Following Faraday's law of induction in equation 3.3, the electric field is related to the potentials via

$$\vec{E} = -\nabla V - \frac{\delta \vec{A}}{\delta t} \quad (3.5)$$

Considering equation 3.5, X-ray spectroscopy can be viewed as the interaction of an electromagnetic field described by the vector potential \vec{A} with electrons in a system described by a potential V .

To further understand the processes involved, the effect of the presence of an electromagnetic field onto the Hamiltonian of the system, H_0 , needs to be discussed. In general, the additional field can be treated as a temporal perturbation of the Hamiltonian from an initial $|i\rangle$ to a final $|f\rangle$ state [33, 36, 40]. Nevertheless, the vector potential \vec{A} needs to be defined first.

If the incoming light is treated as an electromagnetic wave with wavenumber \vec{k} , frequency ω and polarisation $\vec{\epsilon}$, the vector potential can be expressed as [36, 43]

$$\vec{A} = \vec{\epsilon} \cdot \frac{A_0}{2} (e^{i(\vec{k} \cdot \vec{r} - \omega t)} + e^{-i(\vec{k} \cdot \vec{r} - \omega t)}) \quad (3.6)$$

Utilising equation 3.6 and the equation of motion for a charged particle in the presence of an electric and magnetic field, an expression of the perturbation in terms of vector potential interaction can be obtained. A detailed derivation can be found in literature [36, 43, 44].

$$H_p = \frac{e}{2m_e} (\vec{p} \cdot \vec{A} + \vec{A} \cdot \vec{p}) + \frac{e^2}{2m_e} \vec{A}^2 \quad (3.7)$$

with e as the charge and m_e as the mass of an electron and \vec{p} the momentum vector. Utilising Fermi's golden rule for perturbed and scattered systems [45], the intensity of the transition can be approximated to [36]

$$I(\omega) = \sum_f |\langle f | H_p | i \rangle|^2 \delta(E_f - E_i - \hbar\omega) \quad (3.8)$$

The Dirac δ function imposes conservation of energy, allowing interactions only, when $\hbar\omega = E_f - E_i$. The weight of the transition is given by the square of the element $\langle f | H_p | i \rangle$. Under consideration of the dipole approximation ($e^x \approx 1$) and approximating the charge distribution of the system to a dipole, the perturbation H_p is simplified and the dipole transition operator can be defined as $\vec{\mu} \propto \vec{\epsilon} \cdot \vec{p}$ [45].

The dipole transition operator clarifies the possible energetic transitions in the system as, if the operator is non-zero, a transition takes place or, if the operator is equal zero, the transition is dipole forbidden. Considering the odd parity of the dipole operator, with conservation of the angular momentum, it can be stated that [45]:

$$\Delta l = \pm 1 \quad (3.9)$$

$$\Delta m = 0, \pm 1 \quad (3.10)$$

where l is the angular momentum quantum number of the excited system and m is the magnetic quantum number. These rules are the so called "dipole selection" rules.

Since the electron spin is not affected by an electric dipole transition, spin conservation has to be fulfilled:

$$\Delta s = 0 \quad (3.11)$$

3.1.2 X-Ray Absorption

Considering the observations made regarding equation 3.8, one can differentiate between different parts of the perturbation H_p , as described by equation 3.7. The first part H_1 portrays simple transitions from one distinct state to another, while the second part H_2 characterises higher-order processes like scattering (schematic visualisation of the processes can be found in Fig. 3.1) [36].

$$H_p = H_1 + H_2 \quad (3.12)$$

$$H_1 \propto \vec{p} \cdot \vec{A} + \vec{A} \cdot \vec{p} \quad (3.13)$$

$$H_2 \propto \vec{A}^2 \quad (3.14)$$

Concentrating on equation 3.13 and rewriting it in terms of dipole transition operators $\vec{\mu}$ gives

$$H_1 \propto \vec{\mu} + \vec{\mu}^+ \quad (3.15)$$

From equation 3.15 the first addition, $\vec{\mu}$, describes a promotion process called absorption [36]. Here the electron is promoted from the core-level domain to a higher level, absorbing the photon energy in the process and creating a core-hole. The electron can be promoted to a higher unoccupied level and still be bound by the system or to the energetically above lying vacuum continuum, where the electron is no longer bound to the system (see Fig. 3.1a). The remaining excited final state will be called intermediate state $|m\rangle$ from here on.

Through observation of the photon flux and the subsequently absorbed photons (measuring the absorption cross section as a function of incoming photon energy), a method for characterising and observing the electronic properties and the local electronic structure of materials in a medium can be constructed. This process is called X-ray absorption

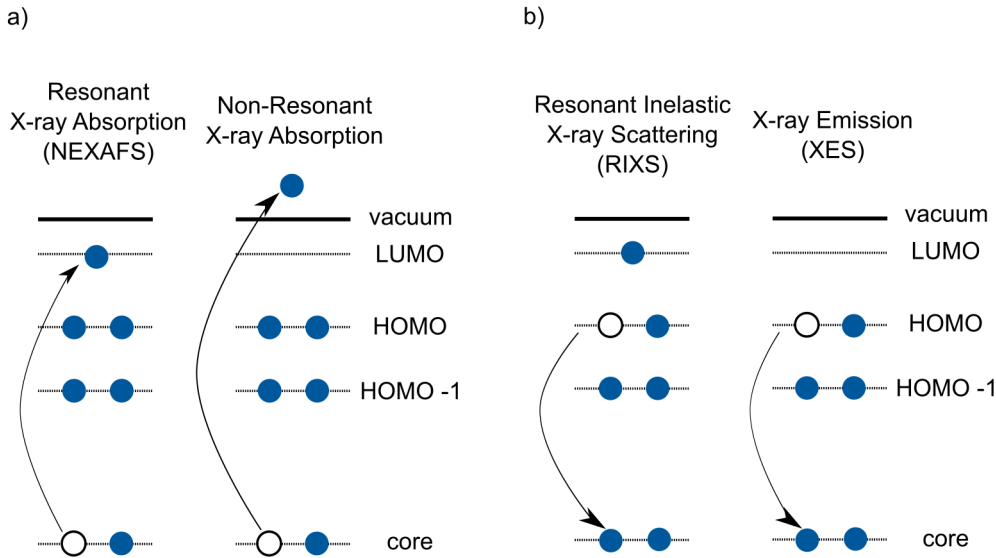


Figure 3.1: **Schematic representation of Electron Promotion and Demotion Processes through X-Ray Radiation:** a) describes an overview of the absorption processes resulting from X-ray irradiation. Depending on the photon energy, one of the two processes occurs. b) illustrates a schematic for the demotion/decay processes, occurring after the absorption. Depending on the absorption type, the processes appear simultaneously or one at a time. [46]

and provides the physical basis for X-ray absorption spectroscopy (XAS). More details on the observation process and instrumentation can be found in chapter 4.

Another option for observation is to detect the electrons that leave the system, and their kinetic energies, to obtain the material properties, which will not be discussed further in this work.

3.1.3 X-Ray Emission

The second part of equation 3.15, the addition $\vec{\mu}^+$, describes a demotion process called emission [36]. After absorption of a photon and creation of a core-hole, the system remains in an excited state $|m\rangle$. An electron from a higher lying level can now fill this core-hole, which will result in an energetically more favourable final state $|f\rangle$. This demotion process from a higher level to the core-hole level is described by $\vec{\mu}^+$ and therefore also obeys the dipole selection rules.

After the demotion of the electron, the energetic difference between the levels gives rise to excess energy, which will be emitted as fluorescence (see Fig. 3.1b) or a so-called Auger electron [47].

In the case of fluorescence, the excess energy is emitted as a photon which can be detected. Observing the spectrum of emitted photons provides a picture of the occupied electronic domain properties of the system and, in case of core-level vacancies, can be obtained element specifically. This process is called X-ray emission, providing the physical basis for X-ray emission spectroscopy (XES). Further details of element specific photon detection can be found in chapter 4.

For Auger electrons, the excess energy is transferred to an electron in a valence level, which in turn will be promoted to the vacuum continuum. Here, detection can be performed by segregating the electrons according to their kinetic energies, which will not be discussed in detail in this work.

3.1.4 Resonant Inelastic X-Ray Scattering

X-ray absorption and emission, as described in chapters 3.1.2 and 3.1.3, can be expressed separately in a two-step model process, as shown in equation 3.15. For higher order processes on the other hand, which e.g. represent scattering due to the final states, the promotion and demotion of the electrons can't be separated [36]. Here I will focus on resonant inelastic scattering processes, as contained in equation 3.14.

Resonant inelastic scattering describes the process of promotion of an electron to an unoccupied level, below the vacuum continuum still bound in the system, and the demotion of an electron to the created core-hole, under the presence of the promoted electron (spectator electron) [36] (see Fig. 3.1b). The observation of the emitted photons gives a deeper spectral understanding and several advantages over X-ray emission, which will be discussed later. Through this process several intermediate states $|m\rangle$ and competing decay channels need to be considered, resulting in the demand for a more complex description. To describe such processes, scattering matrix conformations and simplifications need to be contemplated, resulting in the redefinition of equation 3.14 [36, 45, 48]:

$$H_2 \propto \sum_m \vec{\mu}^+ |m\rangle \langle m| \vec{\mu} = \vec{\mu}^+ \vec{\mu} \quad (3.16)$$

with $\sum_m |m\rangle \langle m| \propto 1$. The resulting resonant inelastic scattering intensity can be described through insertion of equation 3.16 into equation 3.8:

$$I(\omega) = \sum_f |\langle f | \vec{\mu}^+ \vec{\mu} | i \rangle|^2 \delta(E_f - E_i - \hbar\omega) \quad (3.17)$$

The cross terms for the differing intermediate states in equation 3.16 result in multiple interference and wavefunction superposition effects, as well as an overlapping between the lifetime broadening of the intermediate states [48]. This allows simultaneous excitations of more than one intermediate state.

A positive effect established by this is, that spectral features become sharper in contrast to X-ray emission, because the short lifetime of the intermediate state no longer limits the spectral resolution, but the final state lifetime. Additionally there are no dipole forbidden transitions, because the dipole operator acts twice, allowing transitions without angular momentum change. Therefore the selection rules lose their importance, giving this technique a significant advantage over comparable spectroscopies [36].

3.2 Theoretical Model Calculations

The need for theoretical models to fully understand spectral components of measured systems is known by scientists around the world and advances are steadfast [28, 46, 49, 50, 51, 52]. Enhanced calculation algorithms made more complex calculations possible and gave rise to the understanding of more complex systems over time [22, 23, 24, 46, 49, 50].

The above mentioned X-ray spectroscopy processes are an example for these complex systems. To fathom the obtained spectral maps, an understanding of the transitions incorporated in each spectral feature is useful, as a more detailed observation of the inner-workings of the material is possible [40, 49]. The theoretical modelling program ORCA, is a recently developed tool for these type of calculations, including Hartree-Fock (HF) and time-dependent density functional theory (TD-DFT) models [28].

The basis for the above mentioned theoretical modelling is the acquisition of the ground state electronic energy of the system [40]. In the density functional theory (DFT) model, introduced by Hohenberg and Kohn, this ground state energy is obtained through the determination of the electron density [53]. It utilises the Kohn-Sham orbital theory to incorporate the kinetic, electron-nuclear and Coulomb electron-electron interactions and energies [54].

The difference between the various DFT methods is the choice of functional form for the exchange-correlation energy. The general form of the potential functional can be found to be similar in all cases, but slight variations are found to be more precise for specific types of systems [40, 51, 52]. These variations give rise to different functionals and estimation methods, like generalised gradient-corrected approximations (GGA) [55], local density approximations (LDA) [56] and hybrid-GGA methods [52, 57]. The advantage of hybrid-GGA functionals is the combination of both GGA and LDA methods, as well as additional corrections depending on the functional, which also makes them the standard functional methods since recent years [40]. Examples of these functionals are B3LYP [57] or M06 [52].

The first step to a theoretical analysis of X-ray spectra is the optimisation of the ground state energy through geometry alterations. The idea behind this approach is, that the lowest ground state electronic energy of a system is the energetically most favoured state, which is strongly affected by the geometry of the molecular system [28, 40].

To reach the optimal geometry, the DFT approach is utilised to determine the ground state energy, with a subsequent, controlled movement of the atom positions in a system [28, 40]. After the movement, the energy is again calculated, giving a correspondence point for further movements towards a minimum. Under consideration of all previous

points, an energy surface map can be constructed, which will lead to the minimum. Including a step control to ensure that the total length of a step does not exceed the precision of the theoretical method will additionally lead to faster calculations, as less steps are needed to reach the minimum, and the ability to not miss the optimum [40].

After acquiring the optimised geometry of a system, the TD-DFT method is utilised to estimate the transitions occurring in the given system to create the spectral map for K-edge X-ray spectroscopies.

TD-DFT is a simulation model to study the evolution of the kinetic energy in correspondence to a given perturbation of the ground state system [40, 58]. In case of X-ray spectroscopy, the perturbation is the creation or filling of a core-hole. The estimation of the evolving system after presence of a specific core-hole is done using the DFT algorithm in accord to the relevant dynamical equation Hamiltonian. A deeper explanation can be found elsewhere [40, 58], as a more detailed explanation would be out of the scope for this work.

After estimation of the perturbation on the system, the overlap integrals of the orbital functions give the possible transitions and their intensities [36, 40]. Applying a suitable broadening to the energetic positions of the transitions will subsequently deliver an estimated theoretical spectrum of the spectroscopic reactions on the system.

In this work all calculations were performed with the ORCA program package [28]. Molecular geometry optimisations were performed using the M06 density functional method [51, 52] employing the def2-TZVP(-f) basis set [59, 60] (more information on different functionals and basis sets can be found in the appendix 8.1). During the optimisation calculations, the resolution of identity approximation [61, 62, 63, 64, 65] was employed utilising the def2-TZVP/J basis set [66]. Transition energies and moments for the K-edges were calculated with TD-DFT. No intermolecular interaction effects in liquid phase are included. Spectra were obtained from the calculated transition moments by applying a Gaussian type broadening of 0.8 eV.

4 Experimental Methods and Instrumentation

4.1 Synchrotron Radiation

The prerequisite for X-ray spectroscopy studies, the creation of core-hole excitations, yields the need for especially intense, coherent and tunable X-ray light sources. Modern facilities abiding by this principle are e.g. synchrotron and free electron laser (FEL) facilities [67, 68]. The development of the FEL technique specifically made huge steps forward in the last years and several new FEL facilities are in preparation around the world [67]. Nonetheless, the well established number of synchrotron facilities makes them more accessible at the current time. Another important point for choosing where to perform the experiments are the intrinsic differences between synchrotrons and FELs [67, 68, 69, 70]. Even though the advantage of FELs are e.g. a better time-resolution and a possibly higher photon-flux, the flux from modern synchrotron facilities fits the experimental specifications needed in this work. Under the consideration of accessibility and required experimental specifications, this work produced the experimental results at two synchrotron facilities, BESSY II [69] and UVSOR III [71]. More information for each facility and synchrotron radiation in general is explained in the following chapters.

4.1.1 Basics of Synchrotron Radiation

Synchrotron radiation (SR) is generated, when charged particles of small mass and relativistic speed are subject to a transverse acceleration [69, 70]. Thus, SR in synchrotron facilities originates from relativistic particles in a strong magnetic field (more in chapter 4.1.2). The particles of choice in most synchrotron facilities are electrons or positrons, but heavier particles like protons or ions are also applicable, albeit with differing requirements regarding technical instrumentation [68, 69].

The description of the total radiated power of charged particles accelerating in a vacuum can be expressed through the Larmor formula [72]. Under consideration of relativistic

generalisations the total radiated power can be described as [70]

$$P = \frac{q^2 \gamma^4}{6\pi \epsilon_0 c} \left(\left(\frac{d\vec{\beta}}{dt} \right)^2 (1 - \beta^2) - \left(\vec{\beta} \times \frac{d\vec{\beta}}{dt} \right)^2 \right) \quad (4.1)$$

where $\vec{\beta} = \frac{\vec{v}}{c}$, with \vec{v} the velocity of the particle, c the speed of light, $\gamma = \frac{1}{\sqrt{1-\beta^2}}$ is the Lorentz factor and q is the charge of the particle. In case of a perpendicular acceleration to velocity ($\vec{\beta} \cdot \frac{d\vec{\beta}}{dt} = 0$), like experienced by a charged particle in a magnetic field, the equation reduces to

$$P_{a\perp v} = \frac{q^2 a^2 \gamma^4}{6\pi \epsilon_0 c^3} \quad (4.2)$$

Considering the relativistic mass-velocity relationship $E = \gamma m c^2$ and the proportionality relationship $P_{a\perp v} \propto \gamma^4$ one receives the following [70]

$$P_{a\perp v} \propto \frac{E^4}{m^4 c^8} \quad (4.3)$$

A close observation of equation 4.3 reveals why particles with low mass are preferred to heavier ions for the creation of SR. As the total radiated power goes with m^{-4} , the radiation for electrons is $\left(\frac{m_p}{m_e}\right)^4 \approx 10^{13}$ times higher compared to e.g. protons, which affects the photon flux and the brilliance of the light source [68, 70]. The brilliance of a light source is an important measure for modern X-ray light sources and defined as the flux density or the density of photons in transverse phase space [68, 69].

$$brilliance = \frac{photon\ flux}{I} \frac{1}{\sigma_x \sigma_y \sigma'_x \sigma'_y BW} \quad (4.4)$$

where I is the electron current, $\sigma_x \sigma_y$ the transverse area from which the SR is emitted, $\sigma'_x \sigma'_y$ the solid angle into which the SR is emitted and BW as the bandwidth of the monochromator. As most researchers have a certain minimum flux density requirement for their experiments, the brilliance is an appropriate measure to estimate the feasibility of projects at specific light sources.

Another factor affecting the brilliance is the principle source of the SR [70]. The principle sources of SR can be summed up into three different kinds, with different spatial emission and flux characteristics:

- Bending Magnet
- Wiggler
- Undulator

4.1.2 Principle Sources of Synchrotron Radiation

Bending Magnet

The Bending Magnet is, in general, a dipole magnet leading to a perpendicular acceleration of the charged particles due to its magnetic field [70]. Assuming the particles of choice are electrons, the crossing of a magnetic field \vec{B} for relativistic electrons can be described by the following equation of motion [73]

$$\vec{F} = -e\vec{v} \times \vec{B} \quad (4.5)$$

Equation 4.5 yields the creation of SR as described by 4.2 under the consideration of a homogeneous perpendicular magnetic field \vec{B} . In case of a highly relativistic motion the angular pattern of the radiation can be described by [70]

$$\tan \theta = \frac{\sin \theta'}{\gamma(\beta + \cos \theta')} \quad (4.6)$$

where θ' is observed in the reference frame moving with the electron and θ in the laboratory frame (observer). For arbitrarily large emission angles θ' and highly relativistic electrons, the radiation, as observed in the laboratory frame, results in a narrow tangentially directed radiation cone of half angle (see Fig. 4.1a):

$$2\theta \cong \frac{1}{\gamma} \quad (4.7)$$

As a bending magnet is creating SR under a certain angle of emission, the observer sees the photon radiation of an electron or a compressed electron package in a pulsed fashion, due to the solid observation angle [68]. Assuming detection of the radiation starts at a position A on an electron radius of curvature R, due to the electron reaching the horizon at point A within an emission angle $2\theta \cong \frac{1}{\gamma}$, the signal would be detected until a point B, where the radiation cone has turned too far to permit detection, and the duration of the radiation pulse can be described as [70]

$$\Delta\tau \cong \frac{R}{4c\gamma^3} \quad (4.8)$$

Through the use of Heisenberg's uncertainty principle, an anticipated photon energy spread for bending magnet SR can be expressed:

$$\Delta E \geq \frac{2\hbar c \gamma^3}{R} \quad (4.9)$$

The radius of curvature R can also be expressed through $R = \frac{\gamma m v}{eB}$, which changes the expression for bending magnet radiation to

$$\Delta E \geq \frac{2e\hbar B \gamma^2}{m} \quad (4.10)$$

Under consideration of the typically huge values of γ found in modern synchrotron storage ring facilities of several thousands, the radiation spectrum becomes very broad, comparable to a "white light" X-ray light bulb (see Fig. 4.1a) [69].

Concluding, bending magnets create a broad spectrum of photon energies to choose from with average photon flux and pulsed beam structure.

Undulator

Undulators are a straight network of periodically alternating dipole magnets leading to small amplitude oscillations in the electron path [68]. In such a composition two limits need to be considered: An amplitude smaller or bigger compared to the natural radiation width. One speaks about an undulator if the amplitude is smaller compared to the natural radiation width of $2\theta \cong \frac{1}{\gamma}$. The electron moving in such a structural frame experiences a periodic magnet structure moving towards it with a relativistic contracted period λ' creating an oscillating movement and consequent radiation [69, 70].

$$\lambda' = \frac{\lambda_u}{\gamma} \quad (4.11)$$

where λ_u describes the magnet period in the undulator. To translate this expression to the laboratory reference frame of the observer, the velocity dependent Doppler shifting needs to be considered. As the velocity v approaches c , the wavelength variations are dramatically compressed and an observation angle dependency can be observed [70]. The observed on-axis, tangential, wavelength can be described as

$$\lambda = \frac{\lambda_u}{2\gamma^2} \quad (4.12)$$

Using BESSY II as an example, with an electron energy of 1.7 GeV, and an undulator period of $\lambda_u = 5.0$ cm, the relativistically shifted observed on-axis wavelength results in $\lambda \approx \frac{5.0 \text{ cm}}{2.2 \times 10^7} \approx 2.3$ nm. This example shows, that correctly engineered undulators can

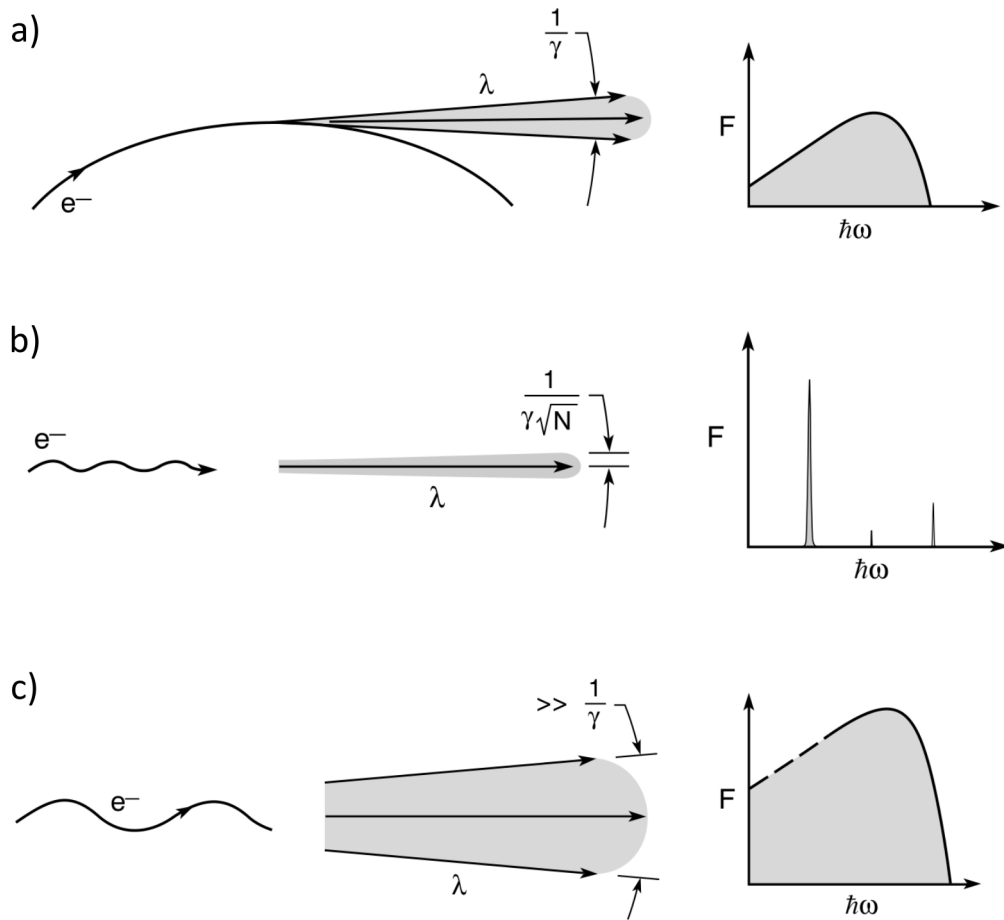


Figure 4.1: **Radiation Patterns of Synchrotron Radiation Principle**

Sources: The relative movement of the electron as well as the expected radiation cone are depicted schematically for all principle sources. The energy distribution of the synchrotron radiation is added as additional information. The bending magnet (a) shows a broader energy spread for the emitted photons compared to undulator radiation (b), which has distinct energetic radiation. Wiggler radiation (c) can be compared to bending magnets (a), considering energetic spread, but exhibit a significantly higher flux. The radiation cones resulting from the electron movement exhibit a more concentrated photon beam for undulator radiation (b) and a highly spread beam for wiggler radiation (c). [70]

achieve precise peaked wavelengths for the use of experiments. Note that, the observer also receives small angle off-axis contributions, as pinholes or similar structures can decrease the acceptance angle θ by a huge margin, but not indefinitely [68]. Therefore the realistic observed wavelength amounts to

$$\lambda = \frac{\lambda_u}{2\gamma^2}(1 + \gamma^2\theta^2) \quad (4.13)$$

The spectral width within the obtained radiation cone can be estimated by taking the difference for two angles, λ and $\lambda + \Delta\lambda$, and accommodating the ratios.

$$\frac{\Delta\lambda}{\lambda} \cong \gamma^2\theta^2 \quad (4.14)$$

Equation 4.14 shows, as one observes the radiation off-axis, that the detected wavelength spread increases. On the other hand, utilising the relationship $2\theta \cong \frac{1}{\gamma}$ for the radiation within the cone results in a small relative spectral bandwidth of about 25% around the peak wavelength.

Adding a monochromator, set by the number of oscillation periods N , after the undulator results in the filtration of the undulator radiation for a "natural" bandwidth $\frac{\Delta\lambda}{\lambda}$. This changes condition 4.14 to [70]

$$\frac{\Delta\lambda}{\lambda} \cong \frac{1}{N} \quad (4.15)$$

Combining both conditions 4.14 and 4.15 an emission solid angle for undulators reduced by a factor $\frac{1}{N}$ can be found leading to a narrower radiation cone width of

$$\theta_u \cong \frac{1}{\gamma\sqrt{N}} \quad (4.16)$$

The undulators were treated as static periodic magnetic structures until this point, but possibilities for tuning the wavelength can be achieved by changing the magnetic parameters. One possibility is through variations of the magnet gap, resulting in changes of the magnetic strength "felt" by the electron [70]. To account for this factor, the non-dimensional magnetic strength is defined as

$$K \equiv \frac{eB_0\lambda_u}{2\pi mc} \quad (4.17)$$

In case of undulators the amplitude in the electron path needs to be small compared to the natural radiation width, yielding the need of smaller magnetic field strengths

of $K \lesssim 1$. The other limit of $K \gg 1$ will be discussed later. Before introducing the magnetic modulated form of equation 4.13, the effects of transverse oscillations have to be considered. These oscillations introduce higher harmonics into the motion, which will also radiate with wavelengths of $\frac{\lambda}{n}$. An explanation regarding the origin and the specific effects of the additional harmonic motions will go beyond the scope of this work and can be found in the according sources [68, 69, 70]. Considering the possibilities for magnetic tuning and higher order harmonic motions, equation 4.13 extends to

$$\lambda_n = \frac{\lambda_u}{2\gamma^2 n} \left(1 + \frac{K^2}{2} + \gamma^2 \theta^2 \right) \quad (4.18)$$

where n is the harmonic number and K the magnetic strength defined through equation 4.17.

As a conclusion, the use of undulators for the creation of SR is broad. The spectral narrowing and smaller cone spread lead to higher brightness of the photon beam. Additionally, through the use of magnetic tuning and the harmonic motions created in the undulator a broad range of partially coherent wavelengths can be selected. Therefore, a monochromator can be utilised to efficiently select specific wavelengths corresponding to the experimental needs. The enhanced flexibility and with high brightness of undulators is a significant advantage over bending magnets, leading to undulators being the most commonly used principle source for the creation of SR [69].

Wiggler

In chapter 4.1.2 it was assumed that the amplitude of the oscillations in a straight network of periodically alternating dipole magnets is smaller compared to the natural radiation width of $2\theta \cong \frac{1}{\gamma}$. If the amplitude reaches the other extreme of being larger compared to the natural radiation width, changes in the above mentioned equations and conclusions need to be considered. This change would be the basis of the transition from undulator to wiggler radiation [69, 70].

The first change to be expressed is the need of a stronger magnetic field strength as defined by equation 4.17, to increase the oscillation amplitude. Subsequently, the magnetic strength in the wiggler limit will abide by $K \gg 1$ leading to the desired amplitudes. Additionally, this also results in stronger accelerations, generating radiation peaks at higher photon energies and a more abundant number of harmonics involved [70]. The increase in acceleration a additionally affects the radiated energy and photon flux with regard to equation 4.2. The number of harmonic spikes created also leads to a quasi-continuum spectral spread, similar to bending magnet radiation [68, 69, 70]. Considering

the radiation spectrum equation 4.10 for bending magnets and rewriting it in terms of the non-dimensional magnetic parameter K (see equation 4.17), an expression for the energetic spectral spread of wigglers can be attained:

$$\Delta E_w \geq \frac{4\pi c\hbar\gamma^2 K}{\lambda_u} \quad (4.19)$$

As the radiated energy is spread into many harmonics, within a cone of angular width of $\frac{K}{\gamma}$, the observation cone angle becomes important for high K values [70]. The larger resulting cone of $2\theta > \frac{K}{\gamma}$ includes a spectral spread with high photon flux, but the brightness of the light decreases compared to an undulator as the radiation cone increases substantially.

The wiggler combines the high flux of undulators with the broad energetic spread of bending magnets, creating opportunities for experiments where both factors are needed. The downside is the increased radiation cone to be considered, leading to huge demands regarding the monochromator and focusing devices. Another important factor is the heatload of these devices due to the high flux, which will not be discussed in detail here [69, 70].

4.1.3 Synchrotrons

A synchrotron facility is, in general, a ring-shaped chamber for accelerated particles [68]. In the beginning, synchrotrons were used as ring-shaped accelerators and usually operated for high-energy or nuclear physics (colliding-beam facilities) and not with the primary goal of creating SR. These rings were first used under parasitic operation, a mode where the radiation created is a byproduct of the actual experimental goal, and later in the so called storage ring mode. These are called "first generation" synchrotron facilities.

As the primary goal of these "first generation" storage rings was different from the creation of SR, they mainly consist of bending magnets, creating a nearly perfect ring form [68]. Under these circumstances only bending magnet radiation as described in chapter 4.1.2 could be produced and the development of new dedicated and principle sources for SR was desired.

These dedicated SR producing storage rings are entitled "second generation" synchrotron. They were primarily designed or operated for the acquisition of photons, but the development of undulators and wigglers further enhanced this process [68]. As undulator and wigglers need a straight passage in the storage ring, the previous design of a "perfect" ring made out of bending magnets needed to be revised. The newer "second genera-

tion" synchrotron incorporating these principle sources were therefore not ring-shaped anymore, but a rather ring-shaped polygon, using the straight paths for undulator and wiggler radiation [68].

At the same time as the development of polygonal storage rings advanced, "third generation" synchrotrons were being designed as a two-ring structure, whose development was meant and later also utilised for "second generation" light sources [68, 69, 70]. The first ring was arranged as a so called booster ring, increasing the energy of the particles to the desired value. The second ring is a "pure" storage ring used to store the particles and keep them at a specific energy. This structure is also the currently most used synchrotron type in the world, due to its high efficiency and brightness obtained [68, 69, 70, 71].

The design of such a synchrotron incorporates five main components [68]:

- electron source with linear accelerator (Microtron)
- booster ring
- storage ring
- radio-frequency cavities (RF-cavities)
- beamlines

The electron source is used for the creation of the desired electron particles, together with a linear accelerator for pre-acceleration. The booster ring boosts the electrons to its final value and the storage ring "stores" the electrons for the use in one of the principle sources of SR. RF-cavities are needed to keep the electrons on a constant velocity in the storage ring, as they would lose energy due to the radiation and vanish from the desired path in the ring. Beamlines are the combination of the insertion device (ID), also called principle source of SR (see chapter 4.1.2), and the successive focusing, monochromatising and collimation of the radiated photons [74, 75]. They are positioned tangentially to the storage ring to fit the radiation cone angle requirements of SR.

The development of "new generation" synchrotrons is currently underway and different approaches are used to create higher brilliance, temporal and spatial coherence [67, 76]. One concept is the free-electron laser (FEL), incorporating a very long undulator in a high-energy electron linear accelerator, by that also abandoning the ring-shaped structure [67]. The other concept is to manipulate the electron-beam and accomplishing better source conditions [76]. The scope aimed for in this work does not require deep insight into "new generation" synchrotrons and the discussion of the different concepts will therefore be omitted.

BESSY II and Beamline U41-PGM

BESSY II is a "third generation" synchrotron located in Berlin, Germany [69]. It uses a hot cathode as an electron source, which emits electrons that are accelerated to an anode, reaching energies up to 70 keV. The following accelerator accelerates the electrons to relativistic velocities of up to 99% of the speed of light and inserting them into the booster ring. The electrons reach energies of up to 1.7 GeV and will be inserted into the storage ring every two to three minutes in the "topping up" mode. This mode ensures that an approximate constant current of 290 to 300 mA for the electrons is maintained, as electrons are lost in the "storage" and radiation processes over time.

The storage ring of BESSY II has a circumference of 240 meters and around 50 consequent beamlines [69]. Some of the beamlines are sharing the same ID, as the radiation desired has similar specifications for the attached experimental end-stations. The beamline this work operated on is the U41-PGM [74], which shares an undulator with the U41-SGM:XM beamline.

The U41-PGM is an undulator beamline creating a highly brilliant, intense and focused soft X-ray beam. A schematic of the beamline is shown in Fig. 4.2a, listing all optical devices.

The first element (M_1), a toroidal mirror, focuses the undulator radiation horizontally and collimates the radiation vertically. Afterwards, a monochromator consisting of a plane grating (G) is used. A photon beam with a high energy resolution in a wide energetic range is created, while avoiding higher grating orders that would interfere in the energy resolution of the beam. The high line-density of the grating ensures a high flux for exciting the samples. The beam impinges a plane mirror (M_2) after the grating, refocusing it onto a cylindrical mirror (M_3), which demagnifies the collimated beam before the exit-slit. The slit is exchangeable to different sizes, ensuring the correct photon flux to spectral resolution ratio. The refocusing chamber comes after the exit-slit. Here a toroidal mirror (M_4) refocuses the beam towards the experimental chamber, which will be explained in chapter 4.2.5. To understand the beamline U41-PGM in greater detail, please refer to the description of Weiss *et. al.* [74].

Choosing the beamline U41-PGM results in several advantages. One is the small micro-focus provided and another the energetic range from 120 eV up to 1800 eV. As will be seen in later chapters, the small focus is needed to perform liquid-jet experiments utilising the LiXEdrom chamber (see chapter 4.2.5) and the energetic range fits perfectly to the experimental parameters needed for investigations on perfluorocarbons (see chapter 5.1).

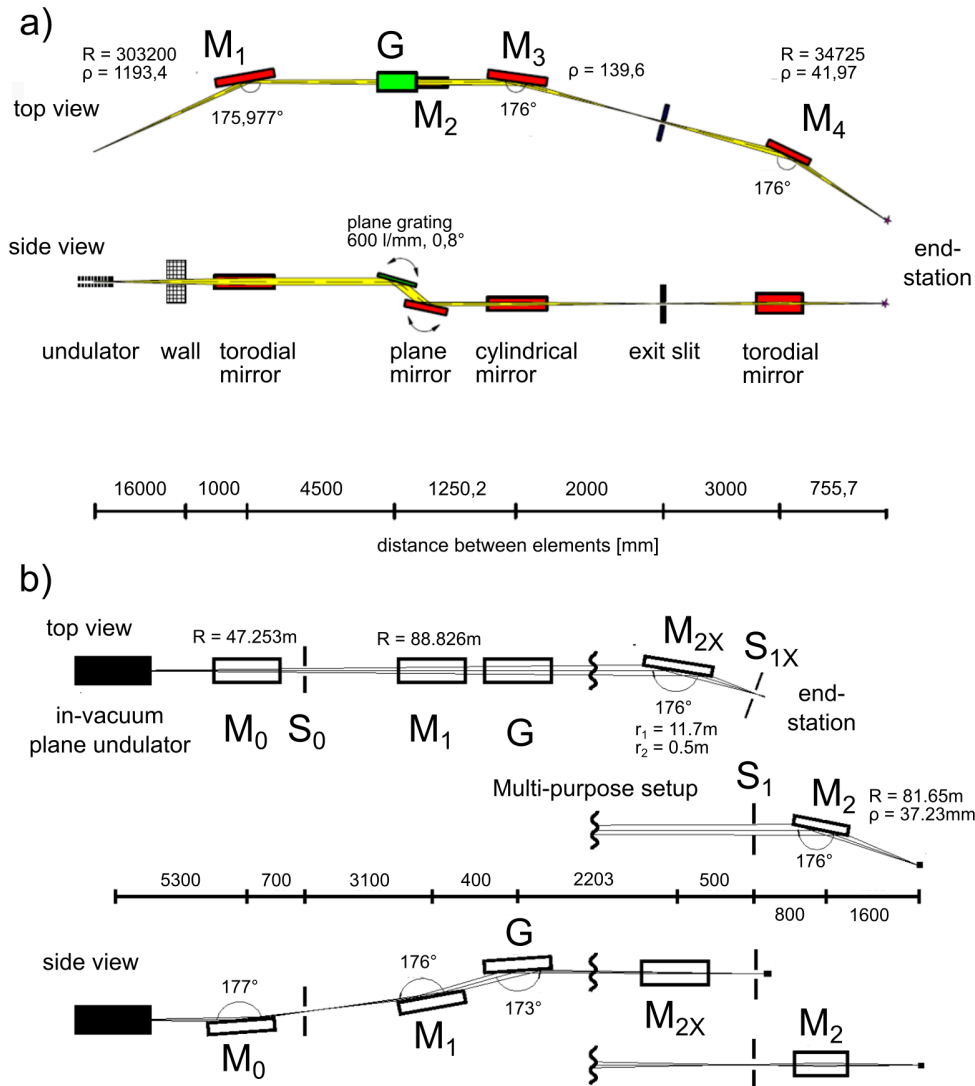


Figure 4.2: **Schematics of the U41-PGM and BL3U Beamline and its Elements:** The beamline U41-PGM is shown under (a) and consists of a toroidal mirror (M_1), the monochromator (consisting of a plane mirror (M_2), a plane grating (G) and a cylindrical mirror (M_3)), the exit-slit and a horizontally deflecting toroidal mirror (M_4) to collimate the soft X-ray beam. [74] The beamline BL3U is shown under (b) and consists of a cylindrical mirror (M_0), a spherical mirror (M_1), the variable-line-spacing plane grating (G) and mirrors for choosing between experimental end-stations (M_{2X}) and (M_2). [75]

UVSOR III and Beamline BL3U

UVSOR III is located in Okazaki, Japan and, like BESSY II, a "third generation" synchrotron [71]. The electron source is a hot cathode, with a following linear accelerator, which accelerates the electrons to relativistic speeds and energies of 15 MeV. Afterwards the electrons are inserted into the booster ring. Here they reach energies of around 750 MeV, upon which they are transferred to the storage ring in "topping up" mode, as described previously.

The storage ring has a circumference of 53 m and 15 consequent beamlines [71]. This chapter will emphasise beamline BL3U (a schematic can be found under Fig. 4.2b) [75].

The ID used for BL3U is an undulator, followed by a cylindrical and spherical mirror. These mirrors are used for focusing and collimation of the beam onto a variable-line-spacing plane grating (VLS-PGM) monochromator used for experiments in the soft X-ray region. The advantages of a VLS-PGM are a better resolution, compared to standard plane gratings, and a better X-ray reflection for the energetic range it was designed for [77]. The disadvantage is a more narrow effective energetic region for the reflection. The following two mirrors are used to focus on one of the two specific experimental chambers of the BL3U beamline. The experimental chamber used will be explained in chapter 4.2.6. More information on beamline BL3U and the UVSOR III synchrotron can be found elsewhere [75].

The energetic range provided by the beamline BL3U is comparable to the U41-PGM, but the slightly bigger focus point may seem disadvantageous. Nonetheless, the specifically designed experimental chamber at beamline BL3U (see chapter 4.2.6) utilises this focus point optimal and provides different possible experimental concepts compared to U41-PGM. These experimental techniques, like transmission type investigations (see chapter 4.2.1), are the reason for choosing the beamline BL3U in this work.

4.2 Liquid Measurements and X-Ray Spectroscopy Techniques

Liquid phase studies with soft X-ray photons experience a number of difficulties. One of the more prominent problems is the need for vacuum conditions to be able to investigate with soft X-rays [78]. While problems, like the evaporation of liquids under low pressures, were addressed by different approaches, the overall goal remains the same: Combining soft X-ray measurement characteristics with the field of liquid studies.

4.2.1 Drop between two Membranes

The "drop between two membranes" method is one of the more simple, but extensively used, experimental approaches for liquid measurements. A small amount of the liquid sample is placed between two membranes of specific, but thin, material. Consequently, liquid measurements under vacuum conditions are made possible, as the membrane separates liquid and vacuum. A schematic visualising this concept can be found in Fig. 4.3a. To detect an absorption signal, the X-ray photons need to penetrate the first membrane to interact with the liquid layer. After passing through the liquid layer the photons have to permeate the second membrane to be able to be detected. This type of absorption process is called transmission mode [79].

This process of absorption and detection is subject to a lot of challenges [79]. The most notable is sample damage through prolonged exposure with X-ray radiation, as the liquid is static and not renewed. Furthermore, does the attenuation effect of X-rays and their intensity, when passing through membranes and liquid layers, play a significant role [79]. Of importance is the path length in the liquid layer e.g., as it defines the absorption rate of the sample, as well as the membrane thickness (around 150 nm each), which needs to be in the micrometre region to let enough X-ray photons penetrate for interaction and detection. The membrane material also exhibits a notable effect. Membranes are available as different materials (Si_3N_4 , SiC , sp^3 carbon, etc.) and the involved atomic elements create artefacts through their own absorption characteristics [38, 39]. This character also defines the absorption rate of all photons in the X-ray region, specifying the penetration ability of specific photon energies.

If all of these problems are accounted for and a spectral analysis was carefully performed, the resulting absorption spectrum is considered to be the most accurate of the presented X-ray absorption techniques, in this work [79].

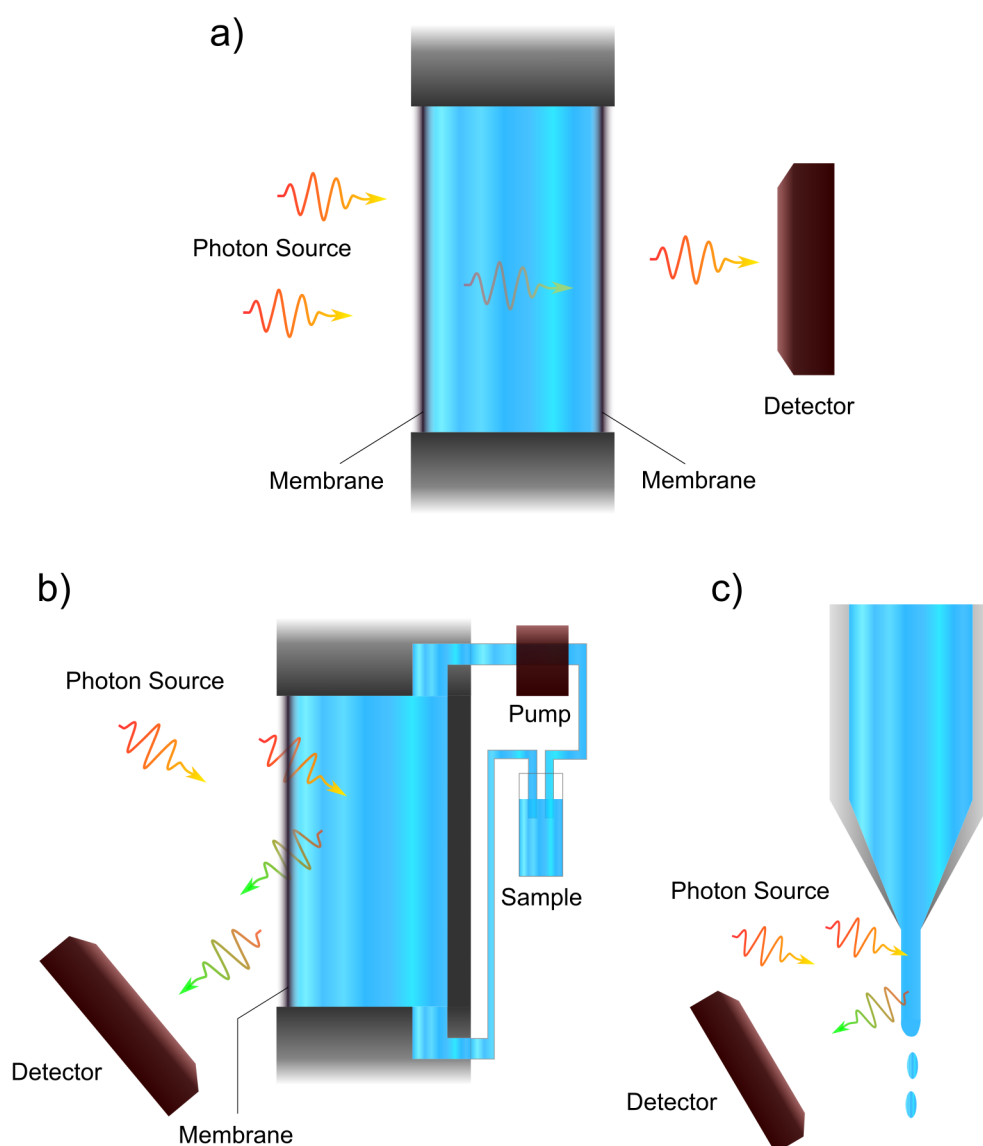


Figure 4.3: **Schematics of Liquid X-Ray Absorption Methods:** a) shows a transmission type cell called "drop between two membranes". The photons pass through membranes and the liquid with a detector at the other side of the cell. b) depicts a liquid flow cell type structure. The liquid is pumped through the cell, ensuring a stable sample environment. The incoming photons react with the sample, emitting photons in this process, which will be detected in turn. c) describes a liquid microjet setup, where liquid is pressed through a glass nozzle with micrometre opening. Here the emitted photons are detected, like in the case of b), a flow cell.

4.2.2 Liquid Flow Cell

As discussed in the previous section, the most prominent problem in measuring X-ray absorption spectra is sample damage. The liquid flow cell approach is developed to deal with this particular problem (schematic can be found in Fig. 4.3b). It tries to combine the advantages of the "drop between two membranes" method with a liquid flow for sample renewing. The continuous flow of sample ensures conditions devoid of sample damage and the membrane creates the separation between liquid and vacuum [80, 81].

Despite the gained advantages of long stable measurements with constantly renewed sample, the use of a membrane still presents undesired effects. In addition to the aforementioned effects in chapter 4.2.1, the long duration measurement conditions and the flow affect the membrane [79]. The exposure of the membrane to the X-ray photons will lead to membrane deterioration over a long time frame and consequently prompt changes in the liquid-membrane interaction. In addition, the sample flow will also affect the liquid-membrane interaction, as artefacts caused by hydrophobic or hydrophilic behaviour can't be excluded [79].

Another complication is that measurements in transmission mode, like in the "drop between two membranes" method, are difficult to achieve and a different approach is chosen. It employs the proportionality of the radiative fluorescence decay process with the total absorption [82]. This measurement method is called total fluorescence yield (TFY) method.

After creating a core-hole state through absorption of a photon, the emitted photons from the fluorescence decay channels are detected. As these emitted photons are radiated in all directions, detection through the same membrane, which lets the incoming photons through, is possible using specific geometries. The non-radiative Auger decay process also needs to be considered, as the quantum efficiency for this process is 99%, compared to the 1% for fluorescence decay, for the demands of K-edge spectroscopy [47, 70]. The Auger decay seems to be the more efficient process for the detection of the absorption, but the ejected electrons have to escape from the sample and travel through the membrane to be detected. As electrons have a much smaller penetration depth, compared to photons, they can't escape the confines of the flow-cell and are unsuitable for this experimental method. Subsequently, fluorescence detection delivers bulk sensitive data [79].

Another factor to be accounted for is sample charging. As fluorescence is insensitive to charging effects it can easily be used in presence of magnetic and electric fields, broadening its possible experimental applications.

Despite the advantages of a flow based system, problems from the TFY method itself appear [82]. Additional artefacts and effects can occur, as decay channels are used for the detection of the total absorption. In contrast, the transmission mode does measure the amount of absorbed photons directly, delivering a clear picture of the absorption. In this work a newly developed flow cell type was adopted, incorporating the "drop between two membranes" structure with a liquid flow system, delivering an experimental setup with the advantages of transmission mode measurements and flow based systems. More information regarding this system can be found in chapter 4.2.6.

4.2.3 Liquid Microjet

Until this point all methods for liquid measurements with soft X-rays incorporated membrane systems, which are, consequently, under the influence of possible membrane effects. The low variety of membrane materials and the subsequent possible sample choices gave rise to the development of membrane-less measurement techniques [83, 84, 85].

To utilise soft X-rays, vacuum conditions need to be met, delivering the biggest hurdle in developing membrane-less systems. One popular method is to "shoot" the liquid with high velocity and small overall surface area into the vacuum [83, 84]. Due to non-adiabatic expansion, the liquid will be cooled and, at the end, freeze on its way through the vacuum, where its trapped by a liquid nitrogen trap for storage. As the travel distance in vacuum is short, the velocity high and the surface area small, the amount of evaporated liquid is limited, delivering the possibility to maintain vacuum conditions with sufficient pumping [83, 84]. Such an experimental system is called liquid microjet (schematic in Fig. 4.3c) and one of the most practised membrane-less systems [85].

To create the high velocity and small surface area microjet a glass nozzle with a micrometre opening is utilised. The liquid sample is put under pressure and "pressed" against the micrometre opening of the nozzle, resulting in a liquid jet stream. The velocity v of the jet, resulting from such behaviour, can be calculated with [86]

$$v = \frac{F}{\pi r^2} \tag{4.20}$$

where F defines the flow and r the radius of the nozzle opening. Consequently, for typical nozzle sizes of around 10 to 30 μm , the resulting velocity amounts to approximately 30 m/s .

At such speeds the jet can be defined by two parts: The laminar area and the droplets [86]. The laminar area is situated directly after the nozzle opening, as a direct conse-

quence of the speed, and only a few millimetres in length. This area provides a region of bulk-like liquid with a defined surface and can be utilised to probe the liquid phase of the sample. At the end of the laminar area, the stream decomposes into small droplets [86]. These droplets increase the overall surface area in the vacuum significantly and need to be frozen in the liquid nitrogen trap to prevent evaporation.

When all the aforementioned conditions are met, vacuum conditions can be maintained and a membrane excluded. Radiation damages are also unproblematic as the continuous jet-velocity is providing undamaged sample at the point of photon interaction at all times. Consequently a membrane-free setup without sample damage can be created. But, in order to incorporate soft X-ray absorption measurements with the liquid micro-jet, the TFY method needs to be utilised, as the jet thickness is preventing the use of transmission mode measurements, contributing the known problems of this method.

4.2.4 Rowland Circle and X-Ray Emission

With the above mentioned measurement techniques, X-ray absorption studies are possible, but measurements concerning the emitted radiation are insufficiently implemented. For X-ray emission studies, a decomposition of the emitted radiation is needed. Specific X-ray gratings can achieve the desired decomposition, especially spherical gratings under Rowland Circle geometry [69, 87].

H.A. Rowland presented a solution for minimising aberrations of spherical gratings in 1882, delivering the theoretical basis for the Rowland Circle geometry [87]. In this geometry, the grating is defined to be spherical with a radius of $2R$. If the photon source lies on a circle of radius R , as depicted in Fig. 4.4, called the Rowland circle, focusing of the energetically resolved photons will occur along this specific circle. Rowland described the focusing of the diffracted lines onto the circle with the grating equation [69, 87]:

$$n \cdot \lambda = -d(\sin \alpha - \sin \beta) \quad (4.21)$$

with n as the diffraction order, λ the incoming wavelength, d as the grating line density, α for the incident and β for the diffracted angle. Of special focus is the diffraction order. The diffraction order is directly correlated to the energy resolution, as higher order diffractions disperse energies to a higher degree unequivocally leading to better resolution with subsequent lower intensity [69, 87].

The Rowland circle design significantly reduces the amount of optical elements needed for photon deconvolution and is therefore a powerful tool to disperse the photons emitted in X-ray emission studies. The blunt result is the separation of the photon energies

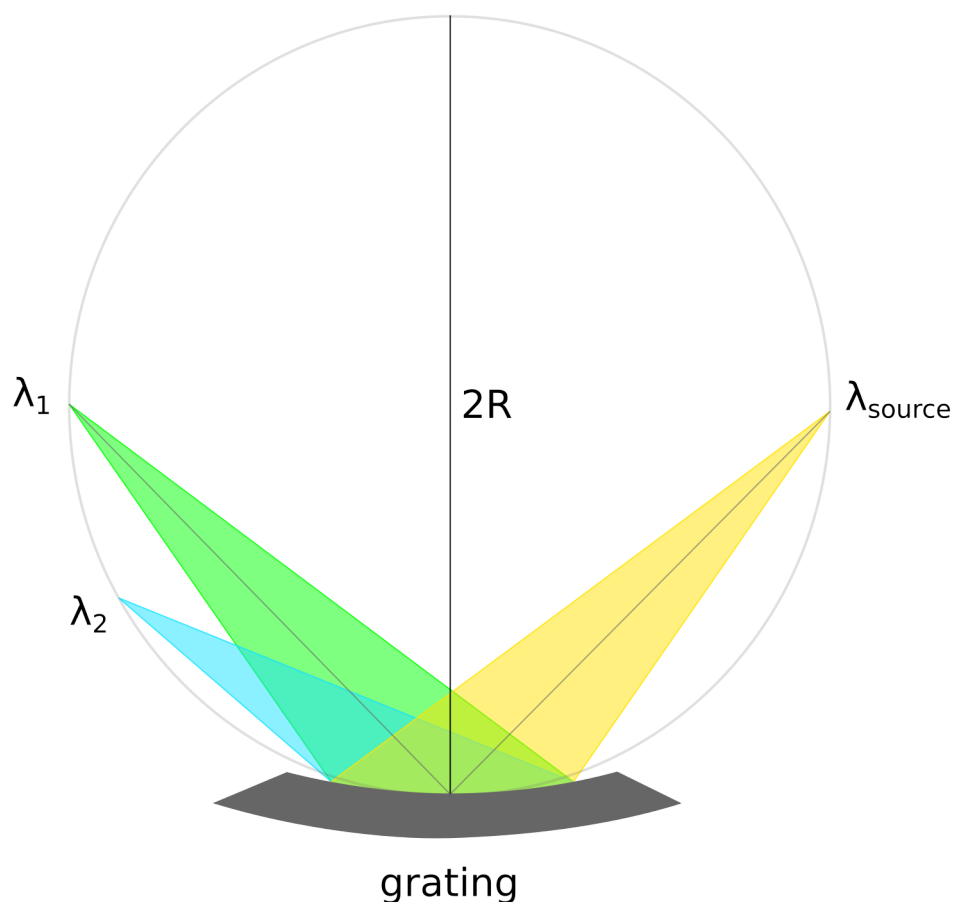


Figure 4.4: **Rowland Circle Diffraction Geometry:** The spherical grating with radius of $2R$ defines the Rowland circle with a radius of R (diameter $2R$). A photon source λ_{source} , on this Rowland circle, will have its spectral components energetically resolved through the grating and refocused onto different spacial position on the circle, e.g. λ_1 , λ_2 .

into their element specific emissions, permitting the study of emission signals from all elements in a sample.

4.2.5 Experimental Setup: LiXEdrom

To achieve liquid measurements under vacuum conditions, several concepts were mentioned until this point. In the synchrotron facility BESSY II at beamline U41-PGM (see chapter 4.1.3) a setup to accommodate these concepts was realised, including complex X-ray emission studies, called LiXEdrom. The LiXEdrom setup (see Fig. 4.5a) was developed with a focus on microjet and emission studies by Lange *et. al.* [88, 89].

It consists of a main and grating chamber, as well as a detector structure in Rowland circle geometry. The liquid microjet is introduced into the main chamber from the top, where it travels in vacuum until being captured by a liquid nitrogen cooled trap. Several vacuum-pumps and additional nitrogen cooled traps are ensuring a stable vacuum of around 10^{-5} mbar. An additional differential pumping stage between main chamber and beamline guarantees safe working conditions for the beamline. The X-ray photons are guided through the beamline onto the jet, where the absorption and emission processes take place. The emitted light will afterwards irradiate a spherical grating in the grating chamber.

The grating chamber operates under a pressure of 10^{-8} mbar, including several gratings for different energetic regions, mounted in a revolver type structure. The photons are energetically resolved under Rowland circle geometry (see chapter 4.2.4) and refocused onto a movable detector structure.

The detector structure is spatially resolving and can be moved to the energetic focus positions to select element specific photons. The detector is a multi-channel plate to CCD camera arrangement for X-ray photon detection.

More information on the LiXEdrom setup in general and the detector structure can be found elsewhere [88, 89].

4.2.6 Experimental Setup: Transmission Flow Cell

To achieve optimal measurement conditions for X-ray absorption, a combination of the "drop between two membranes" system, and its transmission mode, with a liquid flow system is needed. At the UVSOR III synchrotron facility at beamline BL3U (see chapter 4.1.3), Masanari *et. al.* developed such an arrangement [80, 81].

The transmission-type liquid flow cell consists of four regions, which are separated by membranes (see Fig. 4.5b). A liquid sample, which can be substituted by other samples in combination with a tubing pump system, is sandwiched between two membranes with pressed Teflon spacers set between the window frames of the membranes. The X-ray photons, under vacuum (region I), pass through the buffer region filled with helium gas (region II), the thin liquid layer (region III) and reach a photodiode detector in the last region filled with helium gas (region IV). Through adjustment of the helium pressure in regions II and III a control of the liquid layer thickness from 2000 to 20 nm is achieved, ensuring transmission mode conditions.

More details concerning the transmission-type liquid flow cell are described elsewhere [80, 81].

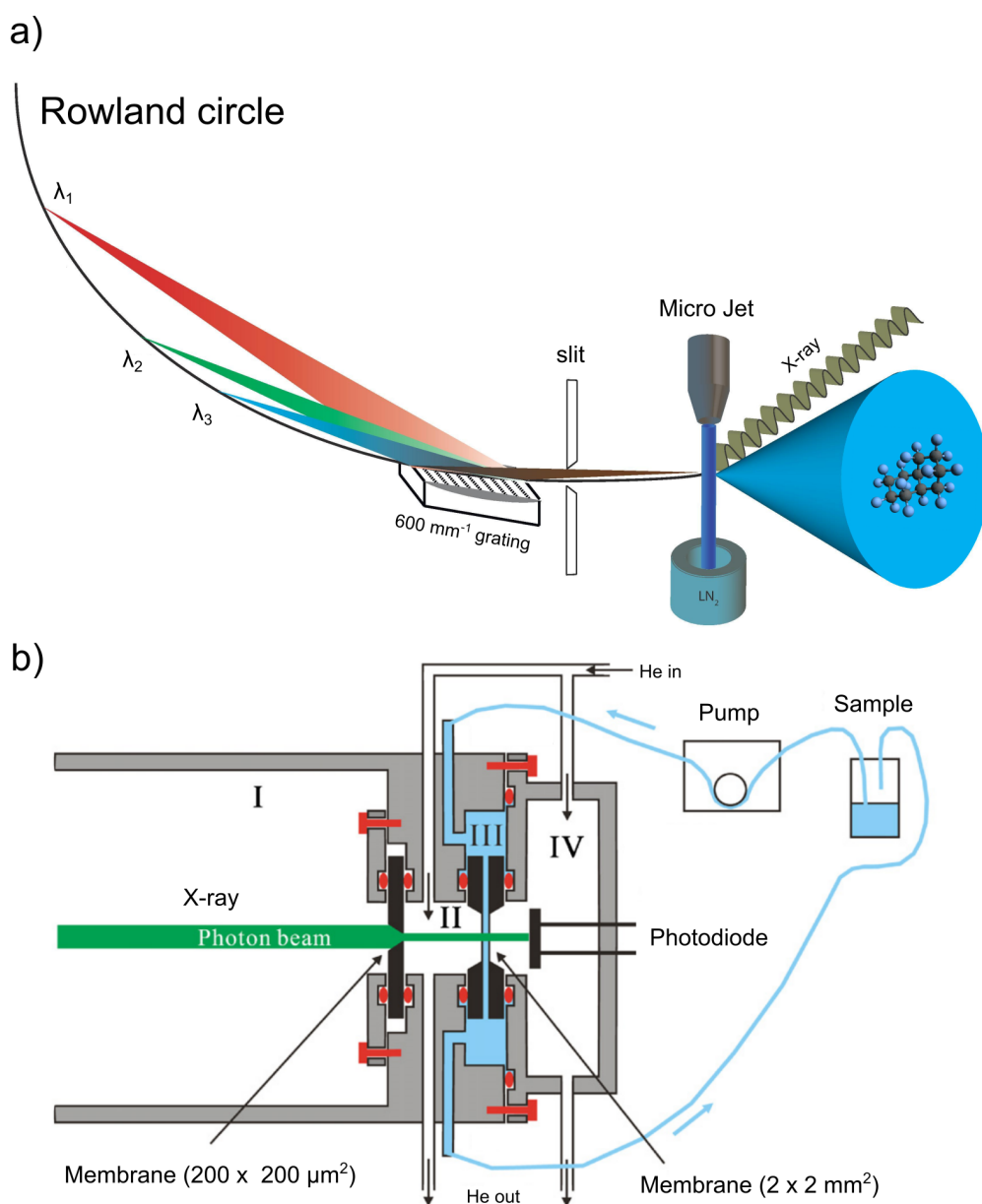


Figure 4.5: **Schematic of the LiXEdrom and Transmission Cell Setup:** a) The sample is injected through the microjet into the main chamber leading to a liquid nitrogen trap. The X-rays hit the jet and the emitted photons are guided onto a spherical grating, where a spectral decomposition under Rowland circle geometry takes place. [88, 89] b) The transmission-type flow cell is separated into four regions. Region I is under vacuum and separated with a membrane from region II, which is under helium pressure. Regions II, III and IV build a "drop between two membranes" system, with region III filled with pumpable liquid and region IV with helium. The helium pressure in region II and IV ensures transmission mode conditions, while pumping is in place. [80]

5 Data Presentation and Discussion

5.1 Highly Fluorinated Materials

As already introduced in the beginning, research in blood substitute formulations is gaining more attention and pharmaceutical companies start clinical trials on different artificial blood approaches [7, 10, 11, 12]. Especially the field of fluorinated microemulsions [6, 9] already delivered an artificial blood emulsion containing perfluorodecalin named Fluosol [12] in 1989 (New Drug Application N860909).

The main oxygen carrier in Fluosol, perfluorodecalin, is part of the family of perfluorocarbons (PFC). The wide range of extraordinary properties of PFCs - high density, high viscosity, high biological and chemical inertness, high gas solubility [18, 19] - offers opportunities for applications in biomedicine and physical chemistry [20, 21]. This delivers diverse applications [1, 14, 15, 16, 17] and creates high interest in scientific development [2, 18, 19, 22, 23, 46, 49].

PFCs consist mainly of carbon and fluorine atoms and are synthesised from their respective hydrocarbons [22, 23, 24]. The corresponding hydrocarbons are often either harmful to humans or exhibit no biomedical interesting features [18, 24]. In contrast, PFCs are mainly non-harmful and exhibit the ability to store and transport gases, while the PFC itself is in liquid phase [18, 19]. Hamza *et.al.* reported that, the structure of the fluid alone seems to be the predominant factor in accounting for the dissolving capacity of gases in fluorochemicals [18], leading to gas that is not chemically or physical bound to the molecule. They proposed that the presence of the fluorine atoms, which are larger than hydrogen, results in more irregular molecular shapes, creating large-sized cavities in the liquid and a possibility to store gases. This trait of storing gases without binding them is, to my knowledge, still not fully understood. Therefore, as earlier fundamental investigations on PFCs were a challenge, especially electronic structure studies, opportunities for further investigation of perfluorocarbons through more complex theoretical models [28] and new experimental techniques [29, 30, 31] can be taken.

5.1.1 The Perfluoro Effect

An inherent feature to all perfluorocarbons is the so called perfluoro effect, which describes the energy shifts of the spectral features due to the stabilisation impact of fluorine in the fluorination process [2, 18, 19, 22, 23, 46, 49]. The magnitude of the energy shift can subsequently be used for a classification of a molecular orbital (MO) to either bear σ - or π -character [22, 23] delivering an experimental method for orbital classification.

This effect was first publicised by Brundle *et. al.* in 1971, where several non-aromatic and aromatic hydro- and perfluorocarbons were investigated employing gas-phase photoelectron spectroscopy [22, 23]. They discovered that "in several instances ... the substitution of fluorine for hydrogen in a planar molecular has a much larger stabilisation effect on the σ MO's than on the π MO's" [23]. Later they called this fluorine stabilisation: perfluoro effect.

The impact of this effect can be seen in how the different orbital characters are treated. "The σ MO's are appreciably delocalised over the fluorine atoms and are strongly stabilised by the high effective nuclear charge of that atom" [23]. In case of "the π MO's, the delocalisation onto the fluorine atoms is much less and its stabilising effect is counteracted by a strong π anti-bond between the fluorine atom and the atom to which it is σ bonded" [23].

To summarise, the high electronegativity and bigger size of fluorine, in comparison to hydrogen, lead to this stabilisation and subsequent investigations lead to further discoveries, like possible fingerprint investigations [90] and explanations for chemical characteristics [2, 18, 19, 49, 46].

5.1.2 Perfluorinated Liquids

The family of PFCs is broad and only a selected few can be investigated in the frame of this work. To get a grasp on the big picture, I therefore choose to observe the two main groups: alkanes (see Fig. 5.1a) and ring-shaped samples (see Fig. 5.1b). These groups are then further split into their corresponding sub-groups: aromatic, non-aromatic and methylated. A full grasp on all samples can be obtained in Fig. 5.1, while further sample specific information, especially experimental complications, follows below.

Note, that the experimental data on some samples could not be obtained due to experimental complications, but a full theoretical study will still be shown for each sample.

Alkanes and Perfluoroalkanes

The first group of PFCs I will describe more closely are alkanes and perfluoroalkanes. As previous investigations on chain-lengths shorter than C_5H_x were already performed in literature [27, 91], chains starting from C_6H_x are in the frame of interest. Consequently, observations on hexane (C_6H_{14}), heptane (C_7H_{16}), octane (C_8H_{18}) and their respective fluorinated counterparts were performed to obtain data on different chain-lengths and to extend on literature observations.

The samples were obtained via Sigma-Aldrich with purities ranged above 85% (> 98% for perfluorooctane, > 85% for perfluoroheptane, > 99% for perfluorohexane, octane and heptane, > 95% for hexane). Performing the experimental observations, complications prevented us from obtaining XE and RIXS spectra for perfluoroheptane and perfluorooctane. The first experimental demand was sample amount, which was highly limited in both cases (around 5 ml), leading to an inability to obtain data at the LIXEDROM machine (see chapter 4.2.5). On the other hand is the vapour pressure, which is not suitable for the liquid microjet technique.

Double Ring Structure Samples

As the double-ring structure perfluorodecalin is treated as a general model system for ring-shaped perfluorocarbons, experimental observations on this material will give us favourable comparisons to chain-structured PFCs. Perfluorodecalin exhibits the special chemical properties of PFCs and is frequently used in applications. As such, I hope to recreate the effects observed and introduced for chain-shaped perfluorocarbons.

This sample exhibits cis- (chair) and trans- (planar) isomerism. As the sample provided by Alfa-Aeser comes in a 50/50 cis/trans mixture exhibiting > 95% purity for perfluorodecalin and > 98% for decalin, the theoretical predictions had to follow appropriately. Consequently, both structures, cis and trans, were calculated and put into a 50/50 ratio for the spectral predictions. Comparisons between the cis and trans spectra can be found in the appendix in chapter 8.2, Fig. 8.10. Note, that all MO shown in later chapters correspond to the trans-structure for better visibility of the MO features.

The corresponding aromatic counterpart for perfluorodecalin was also chosen for investigations to complement the study. This double-ring sample is called naphthalene and only literature data is provided in the according chapter [25] together with the theoretical predictions. Under room temperature it exists as a solid with low flash point, making observations with the provided experimental setups a challenge. The X-ray burns the sample under radiation directly, giving us no opportunity for experimental observations.

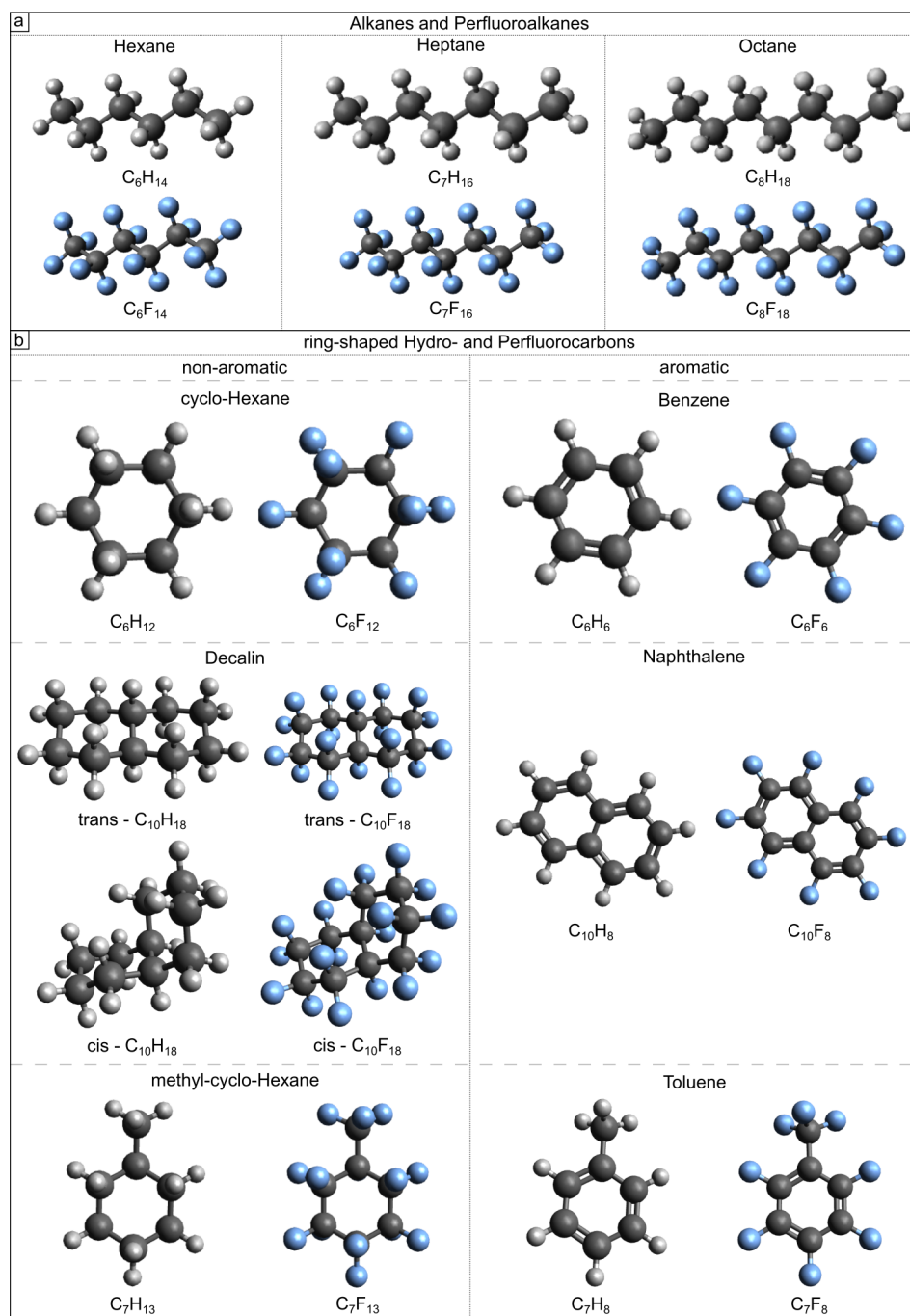


Figure 5.1: **Schematic Representation of all Investigated Samples:** The different investigated hydro- and perfluorocarbons are separated into two main groups: alkanes (a) and ring-shaped samples (b). Alkanes are represented by three different structures, with the main difference being the length of the chain. The ring-shaped samples are separated into aromatic and non-aromatic, as well as one-ring, two-ring and methylated sub-samples.

Single Ring Structure Samples

For further comparisons between chain- and ring-shaped PFCs, the epitome of ring-shaped systems was chosen: benzene. Nonetheless, benzene as an aromatic structure can only deliver part of the basic picture, as non-aromatic systems also need to be accounted for. Consequently, the non-aromatic system cyclo-hexane was chosen to complement benzene as aromatic, single-ring, structure.

Benzene was obtained via Sigma-Aldrich with a purity of > 99% and the corresponding fluorinated compound with purity around > 90%. Concerning the experimental data, the XE data on benzene is missing. Nonetheless, as benzene is the primary example of ring-shaped systems, literature XE data was quoted for comparisons to the theoretical predictions [92].

In case of cyclo-hexane and its fluorinated counterpart, the experimental complications came from the availability of the fluorinated sample. As only several drops (below 1 ml) could be obtained, no experimental data will be provided from my side. Still, the theoretical predictions can be compared to gas-phase spectroscopic literature data to obtain a greater grasp on the system [27, 93].

Methylated Samples

Special attention needs to be given to structures having a "dangling" methyl group [22, 23], as their gas storing capacities are higher than their non-methylated counterparts [19, 94]. Consequently, observations on methylated groups and comparisons to their non-methylated structures attains a special meaning. I choose to obtain the methylated counterparts for cyclo-hexane and benzene, as they are the least complex ring-shaped structures investigated in this work.

The corresponding structures, methyl-cyclo-hexane and toluene were obtained via Sigma-Aldrich with purities > 90% for the fluorinated samples and > 95% in the case of hydrocarbons. Note that, experimental complications similar to the above mentioned alkane samples (especially sample amount) came into play, preventing us from obtaining experimental XE data.

5.2 Chain-Shaped Hydro- and Perfluorocarbons

The Carbon K-Edge

In liquid emulsions several effects need to be accounted for. Two of the more prominent are the conformation effect [95] and the van der Waals force [96]. The conformation effect affects peak broadening and is a result of excited orbital interactions with surrounding molecules of different conformations [95, 97]. In the case of nonpolar systems, the acting van der Waals force is the London dispersion force, that is, an attractive force resulting from induced dipoles [96]. Liquid fluoroalkanes and their respective hydrocarbons, like the presented molecules in this chapter, are subject to weak van der Waals forces and have a high amount of different conformational geometries [18, 98].

The experimental carbon K-edge XA spectrum of the hydrocarbons (Fig. 5.2a) reveals a striking similarity between the different chain-shaped molecules hexane, heptane and octane. The presence of a pre-peak at 287.5 eV, the main feature around 288.05 eV and a broad band at 292.8 eV can be identified in all cases. By employing theoretical calculations based on the DFT algorithm for geometry optimisations and TD-DFT for spectral calculations on single molecules, the general spectral shape of the XA spectra can be reproduced (Fig. 5.2a). Based on the calculations and previously proposed assignments, the broad band feature around 292.8 eV is assigned to σ^* (C-C) shape resonances. The calculated bond lengths of the hydrocarbons (1.53 Å uniformly) further support this assignment, due to the correlation of σ^* resonance positions with the bond length of hydrocarbons [99]. This correlation is called " σ -shifting" effect and is a known effect of hydrocarbons, where a C-C bond length increase is accompanied by a shift of σ -features to lower energies, resulting in a constant energetic σ^* resonance position for the presented materials.

The main feature at 288.05 eV exhibits, in contrast to the conclusions on the gas phase drawn by Hitchcock *et al.* [100], no significant changes between the different hydrocarbons. Hitchcock *et al.* observed a decrease in peak area and height as the amount of (CH_2)-chains increase [100]. However, the provided data shows a significantly smaller decrease upon reaching hexane and my theoretical calculations give no hints to changes in the major feature. Taking the presented data in this work into account, I conclude a smaller influence of the peak area and height decrease effect as the amount of (CH_2)-chains exceeds four. We also observe an intensity increase and energy shift (100 meV) in the pre-peak feature as the number of (CH_2)-chains increases, which is confirmed by the data provided by Hitchcock *et al.* for chains with one to four CH_2 [100]. The intensity increase can be explained through a higher cross-section for this particular transition as

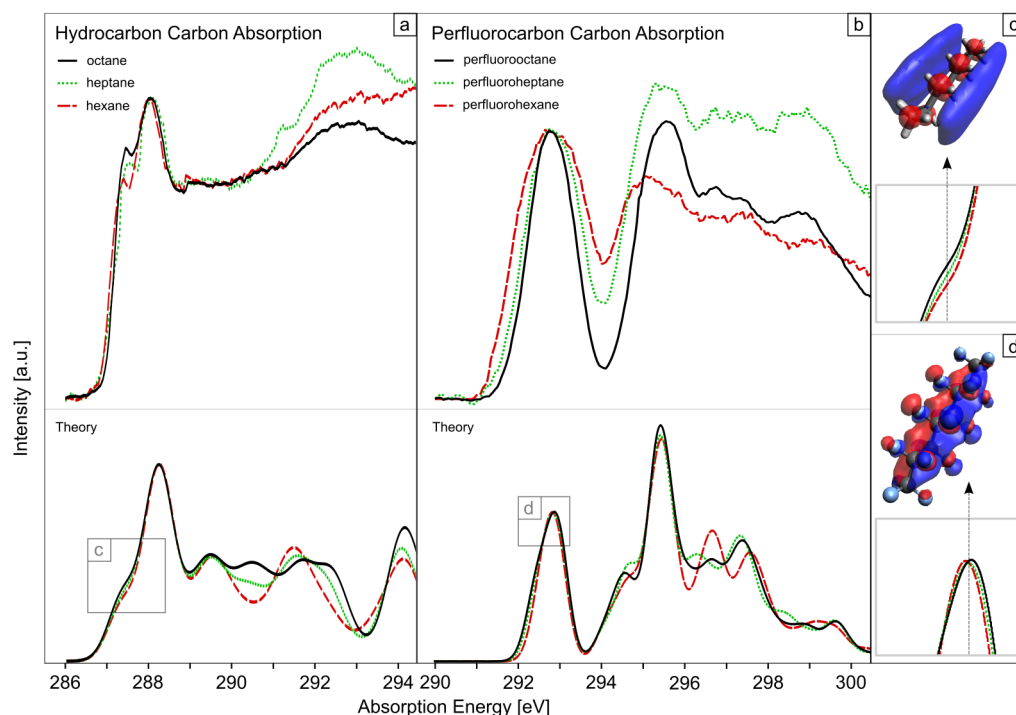


Figure 5.2: **Carbon K-edge Absorption for Hydro- and Perfluoroalkanes:** Experimental and theoretical carbon K-edge X-ray absorption data for chain-shaped hydrocarbons (a) and their respective perfluoroalkanes (b). The insets (c, d) represent the main areas of change in the experimental spectra and illustrate the molecular orbitals for the corresponding transitions.

the amount of (CH_2) carbons is raised, which is also confirmed by the simulated spectra (Fig. 5.2c), albeit no hint to an energy shift is observed and the intensity increase is underestimated. Small energy shifts can result from intermolecular interactions [97, 101]. The theory doesn't include intermolecular interactions, but chain-shaped hydrocarbons are molecules, which are confined in the vicinity of each other in liquid phase due to strong intermolecular forces [102]. Here, the dominant forces are London dispersion forces [98, 103, 104], which are an attractive force resulting from temporary dipoles induced by interactions of electrons in two adjacent molecules. London forces become stronger as the molecule grows larger due to a higher contact interaction from the increased surface area. Strong dispersed electron clouds over the surface further amplify this effect. The orbital correlated to this particular transition is provided in Fig. 5.2c and exhibits a strong distribution over the intermolecular contact surface; however, this effect is applied not only to the ground state but also to the core-excited state, resulting in minor effects in the XA peak shift and width.

Fig. 5.2b shows the experimental carbon K-edge XA spectra of the perfluorocarbons perfluorohexane (PFHex), perfluoroheptane (PFHep) and perfluorooctane (PFO), as well as the corresponding theoretical calculations. Theory predicts the spectral shape reasonably well, with a strong resonance at 292.8 eV, a dip around 294.1 eV and several shape resonances above 295 eV. According to the calculations I can assign the resonances above 295 eV uniformly as σ^* (C-C) shape resonances for all perfluorocarbons. The main resonance at 292.8 eV exhibits a decrease in full-width at half maximum (FWHM) as the amount of (CF_2) -chains increases. The FWHM decreases from 2 eV (PFHex) over 1.5 eV (PFHep) down to 1.2 eV (PFO). As the FWHM decrease is not depicted in the theoretical predictions, the most likely cause is an effect not incorporated in the calculations, like intermolecular interactions. In the case of isolated atomic and molecular systems, the width of a resonance is determined by the inverse of the lifetime of the final state [105]. The life-time broadening is not so much affected by the molecular interaction in the case of interacting systems such as clusters and liquids. Instead, different molecular conformations can affect the peak broadening due to the exchange interaction of excited electrons with surrounding molecules of different conformations [95, 97]. This so called conformation effect can be exhibited if the excited orbital is of delocalized character, as delocalized orbitals are more sensitive to the surrounding, and gains influence if the amount of different molecular conformations in a liquid is high. Perfluorocarbons are known for having a high amount of slightly distorted molecular geometries, due to the substitution of hydrogen to the highly electronegative and bigger fluorine, which subsequently results in a high amount of different conformational geometries [18].

In case of perfluoroalkanes the amount of geometries is also directly affected by the length of the chain and should lead to a higher peak broadening for PFHex compared to PFO, due to the conformation effect and the higher amount of different conformational geometries. The feature at 292.8 eV can mainly be attributed to π_z (C-C) resonances (see Fig. 5.2d), which are of delocalized character. As mentioned above, different intermolecular interactions of an excited orbital of delocalized character with the surroundings results in an influence on the peak broadening. As the amount of (CF_2) -chains increases, the size of the molecule and accordingly also the size of the MO increases (see Fig. 5.2d, Fig. 5.3 and Appendix 8.3), resulting in more delocalized orbitals and more conformational geometries. This directly leads to a higher peak broadening for PFHex compared to PFO due to the more delocalized orbital and the intermolecular conformation effect. Subsequently, PFHex has the widest FWHM from the compared perfluorocarbons and PFO the narrowest as a direct outcome from the difference in conformational geometries. Additionally, an investigation of different dimer, trimer and more complex structures would improve the understanding of the impact

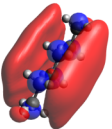
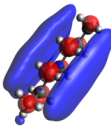
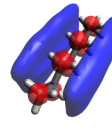

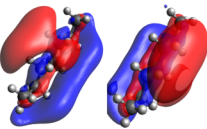
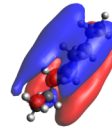
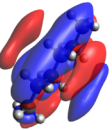
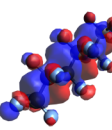
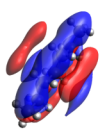
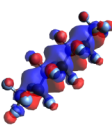
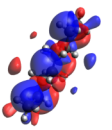
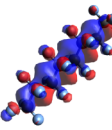
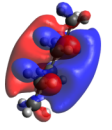

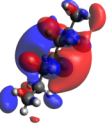
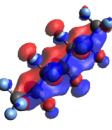
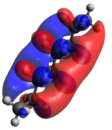
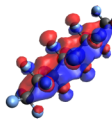
	Hexane	PFHexane	Heptane	PFHeptane	Octane	PFOctane
A		-		-		-
B		-		-		-
Γ						
Δ						

Figure 5.3: **Table Representation of the Alkane Molecular Orbitals:** Table representation of the molecular orbitals involved in the energetic shifts and corresponding transitions.

of conformational geometries in the given materials. Subsequently, molecular dynamics investigations of different conformations are recommended to extend the analysis.

Within the theory of the frontier orbital model the lowest unoccupied molecular orbitals (LUMO) play a major role in defining the interaction between two different liquid compounds [106], resulting in a great influence on the dissolving capacity of the main with the target liquid material. In the present case, the main compound is changing the spectral width of the LUMO associated transitions, which directly translates to changes in the intermolecular interaction habits of the liquid within the frontier orbital model. As the spectral width changes due to the different intra- and intermolecular conformations, these should subsequently influence the compound's dissolving capacity of, e.g., water. According to Freire *et. al.* the mole fraction solubility of water increases as the chain-length of perfluoroalkanes rises [2]. This coincides with the observations and conclusions drawn from the LUMO differences in the XA spectra of the presented materials leading to a direct impact of the different conformational geometries on the dissolving capacity of chain-shaped perfluorocarbons with water. I note that the conclusions drawn by Hamza *et. al.* mention that the high amount of different molecular conformations in perfluorocarbons affect the dissolving capacity with liquids and gases [18], further supporting my findings. To further understand this concept of conformational geometries

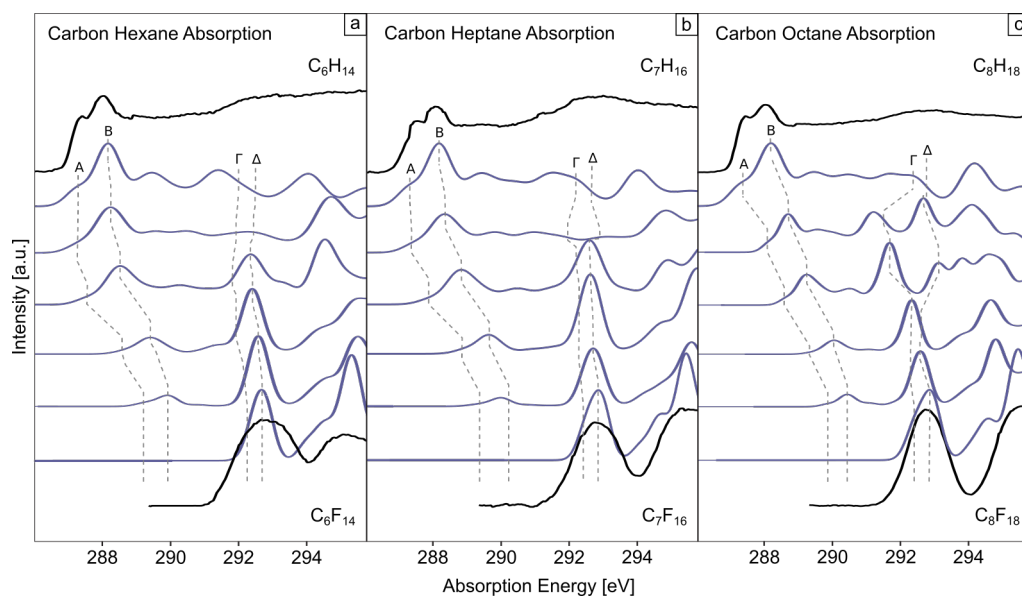


Figure 5.4: **Carbon K-edge Absorption: Perfluoro Effect for Hydro- and Perfluoroalkanes:** Experimental (black lines) and calculated (blue lines) carbon K-edge X-ray absorption spectra for hexane (a), heptane (b), octane (c) and their respective fluorinated compounds. Dashed lines indicate the shifts of the spectral features.

influencing the dissolving capacity with other liquids and possibly gases, an extension to more complex perfluoro compounds and gas loaded samples, as well as molecular dynamics investigations, is recommended.

Theory predicts an additional small transition attributed to π_x (C-C) resonances (see Fig. 5.3 and Appendix 8.3 for the molecular orbitals) at 292.2 eV, which creates a small shoulder on the low energy side of the resonance at 292.8 eV. The experimental spectra don't give clear evidence for this transition, but the non-uniform energy changes on the lower energy side, compared to the higher energy side, give rise to speculations for the existence of this transition. The form of the participating MO suggests an involvement with the conformation effect to a similar degree to the π_z (C-C) resonance described above. Under these circumstances the transition would also be subject to the broadening effect explained earlier giving rise to a non-uniform energy change on the low energy side of the 292.8 eV resonance. Further analysis of this transition will be subject to future investigations as more data on different perfluoroalkanes is needed for an unequivocal understanding.

The experimental carbon K-edge XA spectra for the hydrocarbons and perfluorocarbons, the calculated spectra for the respective molecules as well as the stepwise fluorinated hydrocarbon derivatives are presented in Fig. 5.4. The figures also visualise the energy

shifts of the four main features upon fluorination for the XA spectra. The dimension of the shifts gives rise to a possible direct σ - or π -character assignment for the participating orbitals in these features as described by Brundle *et. al.* (2-4 eV corresponds to σ , 0-0.5 eV corresponds to π) [23], where π is of out-of plane and diffuse (Rydberg-like) character, but not of anti-bonding character like π^* . This information is summarised in Table 5.1.

feature	energy shift upon complete fluorination [eV] (PFHex)	energy shift upon complete fluorination [eV] (PFHep)	energy shift upon complete fluorination [eV] (PFO)	orbital character
<i>A</i>	1.76	1.68	1.70	σ -like
<i>B</i>	2.11	2.10	2.06	σ
Γ	0.15	0.19	0.14	π_x (C-C)
Δ	0.17	0.09	0.10	π_z (C-C)

Table 5.1: **Perfluoroalkane XA Carbon K-edge Character Table:** Energy shifts and derived MO characters for the XA features.

The energy shifts reveal strong similarities between the main-features of each molecule, as suggested above. Small differences exist, which can be attributed to the addition of (CF_2)- or (CH_2)-chains and the resulting small changes in molecular length, but the overall molecular character assignment is equivalent. Resonance *A* is the only not clearly assignable feature, but due to the strength of the energy shift a clear trend to σ -like character can be seen. A closer look at features *A* and *B* reveals that they disappear and don't have a counterpart in the absorption spectra of the perfluoroalkanes. We note, that all fluorinated hydrocarbon derivatives exhibit these features, albeit their intensity decreases with increasing number of F atoms. This anomaly will be discussed further later in this chapter.

Features Γ and Δ behave according to the theory of the perfluoro effect with a controlled stabilisation of the MOs due to the fluorination. We note that the step from hydrocarbon to the first fluorinated hydrocarbon derivative involves a significant energy jump to the lower energy region. This energy shift is the result of the transformation of the previous pure carbon orbitals because of the substitution of hydrogen with electronegative fluorine. In case of Γ and Δ the involvement of fluorine quenches the MO, due to its shape, into a more confined space surrounding the carbon atoms. The first fluorination step therefore has the strongest impact on the MO, while the subsequently added fluorines stabilise the quenched MO, resulting in a stronger energy jump for the

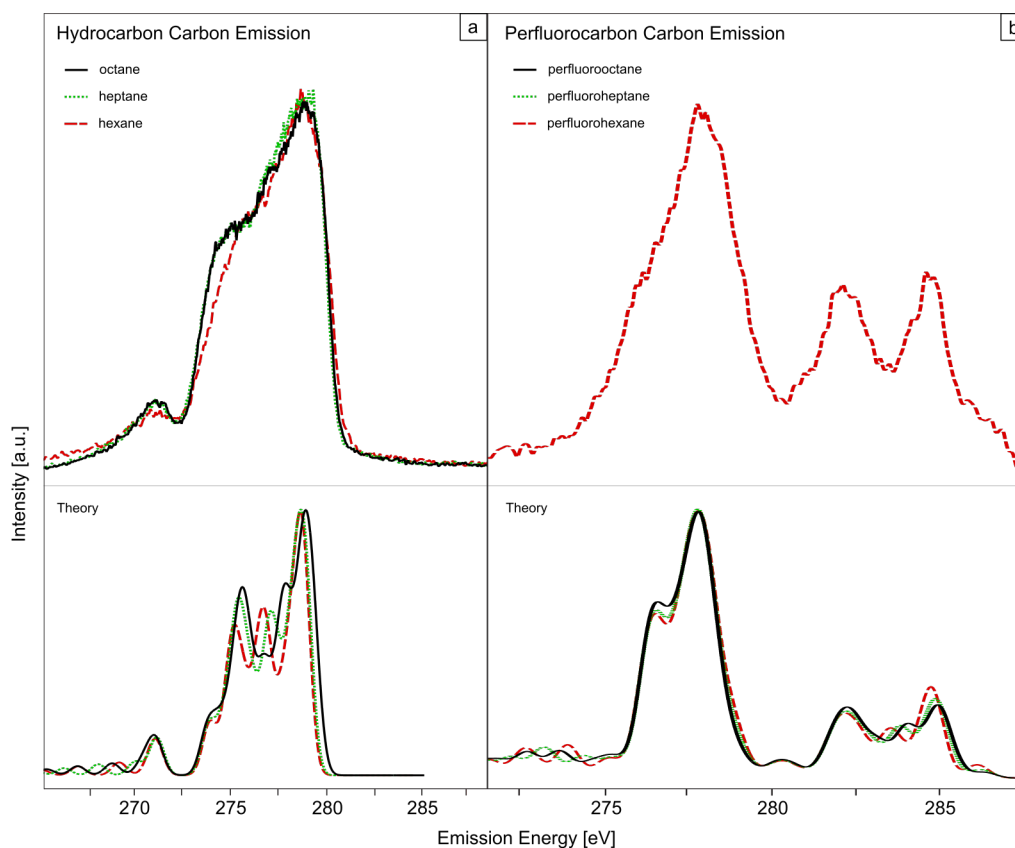


Figure 5.5: **Carbon K-edge Emission for Hydro- and Perfluoroalkanes:** Experimental and theoretical carbon K-edge X-ray emission data for chain-shaped hydrocarbons (a) and their respective perfluoroalkanes (b). Experimental and sample limitations lead to the missing perfluoroalkane data.

first fluorination.

Additionally, the fluorine acts like a shield to shelter the MO from outside influence as the orbitals are largely localised on the carbon atoms, which are repulsively interacting with a potential barrier created by the exchange interaction of the fluorine atoms. Subsequently, these orbitals have limited overlap with potentially reacting molecules, leading to a higher relative inertness within the understanding of the frontier orbital model [106]. This effect can be recognised as one of the reasons to the high relative inertness of perfluorinated alkanes.

The experimental carbon K-edge XE spectrum of the hydrocarbons (Fig. 5.5a) exhibits a strong similarity between the different chain-shaped hydrocarbons. Four main features can be identified: the main peak at 278.8 eV with a slight shoulder around 277.4 eV, a pronounced shoulder around 275.0 eV and a weak feature at 271.1 eV. The employed theoretical calculations retraced the general shape of the XE spectra and can, similarly

to the XA calculations, be used to assign the features. Additional help can be provided by utilising the XE spectra of rather simple hydromethanes, like CH_4 [107]. The carbon K-edge emission spectrum of especially CH_4 [107] and C_2H_6 [91] should reveal similarities to more complex chain-shaped hydrocarbons, due to the absence of fluorine atoms and the sp^3 -hybridised carbon character. Indeed, CH_4 displays one broad feature around 277 eV, which is an indicator for sp^3 -hybridised carbon character [107]. Furthermore, a glance at the spectra of C_2H_6 and C_3H_8 reveals an additional shoulder compared to the carbon XE spectra of CH_4 at around 274.8 eV [91]. This shoulder can be attributed to C-C bond interactions and coincides with the observed shoulder at 275 eV in this work.

As expected, the presented experimental spectra are more complex than simple hydrocarbons, exhibiting a broader peak and, using the calculated XE spectra, indicating a second transition at around 278.8 eV and small energetic shifts. Nonetheless, due to the phenomenological similarity to simple hydrocarbons, I can assign γ_1 and γ_2 as having sp^3 -hybridised carbon character and the shoulder β as resulting from C-C bond interactions. α can also be attributed through the above mentioned method and is contributed through transitions of deep valence orbitals. These transitions play a minor role in the chemical processes of hydroalkanes and will therefore not be discussed in deeper detail. Comparing the different hydrocarbon XE spectra reveals no significant changes in the spectral features, with the exemption of feature β . The main difference between the presented materials is the increase in CH_2 chain length. As attributed above, β corresponds to C-C bond interactions, subsequently leading to an increase in the cross section for C-C bond interactions as the amount of CH_2 carbons is raised. We take note that the experimental spectra, as well as the theoretical predictions, exhibit this increase, with small differences in the amount of increased intensity between the hydrocarbons.

Carbon K-edge XE spectra of the perfluoroalkanes are compared to predictions in Fig. 5.5b. The provided experimental spectrum solely consists of PFHex, while the theoretical calculations exhibit all perfluorocarbon spectra. The reasons behind the missing XE spectra are thoroughly explained in chapter 5.1. The spectra show a sharp low-energy peak around 278 eV, and a double-peak structure at 282 eV and 284.7 eV. A small shoulder around 286.3 eV can also be confirmed.

Again, the overall shape can be understood by comparing the XE spectra of gas-phase fluoromethanes. As the perfluoroalkanes mainly consist of CF_2 and CF_3 carbons, special attention is given to the fluoromethanes CH_2F_2 and CHF_3 . Indeed, the carbon K-edge XE spectrum of CH_2F_2 shows a three-peak structure [107]: a broader peak at lower energies (277 eV), typical for sp^3 -hybridised carbon, a sharper high-energy peak (283 eV), due to a mixed C-F orbital, and a peak at intermediate energies (281 eV),

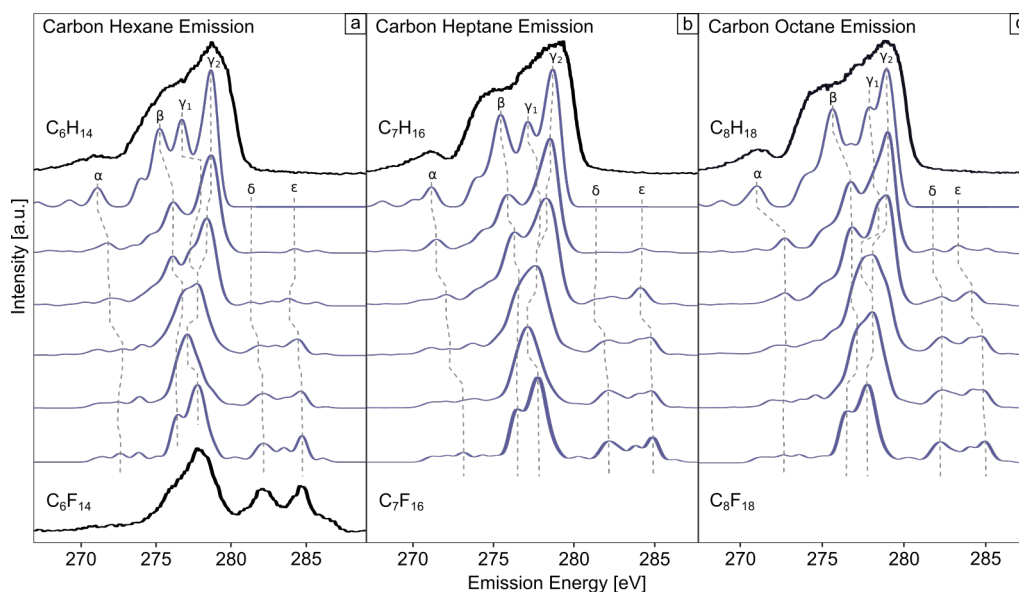


Figure 5.6: **Carbon K-edge Emission: Perfluoro Effect for Hydro- and Perfluoroalkanes:** Experimental (black lines) and calculated (blue lines) carbon K-edge X-ray emission spectra for hexane (a), heptane (b), octane (c) and their respective fluorinated compounds. Dashed lines indicate the shifts of the spectral features. Experimental and sample limitations lead to the missing perfluorocarbon data.

where the orbitals predominantly have fluorine character. The similarities between the spectra suggest an overall assignment accordingly, albeit chemical shifts need to be considered. The carbon K-edge XE spectrum of CHF_3 also exhibits a three-peak structure with a chemical shift of around 1 eV to higher energies [107]. Subsequently, the high-energy shoulder around 286.3 eV can be attributed to CHF_3 and the sharp high-energy peak (284 eV) as resulting from a mixed C-F orbital. As this shoulder is exhibited by the CF_3 carbons, it will be more profound for short chain-like perfluorocarbons, as the intensity ratio of CF_2 to CF_3 carbons will get more favourable. This is confirmed by the theoretical predictions and I can assume that this feature vanishes for sufficiently long fluoroalkanes.

The experimental carbon K-edge XE spectra for the hydrocarbons and perfluorocarbons, the calculated spectra for the respective molecules as well as the stepwise fluorinated hydrocarbon derivatives are presented in Fig. 5.6. The figures also visualise the energy shifts of the main features upon fluorination. As mentioned above, according to the dimension of the shifts a σ - or π -character assignment for the participating orbitals in these features can be achieved (2-4 eV corresponds to σ , 0-0.5 eV corresponds to π). This information is summarised in Table 5.2.

feature	energy shift upon complete fluorination [eV] (PFHex)	energy shift upon complete fluorination [eV] (PFHep)	energy shift upon complete fluorination [eV] (PFO)	orbital character
α	1.4	1.9	1.5	σ -like
β	1.2	1.0	0.8	not distin- guishable
γ_1	1.3	1.2	0.8	not distin- guishable
γ_2	0.8	0.9	0.8	not distin- guishable
δ	0.5	0.6	0.4	σ
ε	0.3	0.25	0.2	σ

Table 5.2: **Perfluoroalkane XE Carbon K-edge Character Table:** Energy shifts and derived MO characters for the XE features.

Similar to the XA features, the energy shifts reveal strong similarities between the main-features of each molecule, while small differences can be attributed to the addition of (CF_2)- or (CH_2)-chains and the resulting small changes in molecular length. Several features are not clearly distinguishable with the energy shift method and can be assumed to be of mixed character. Resonance α is the only discernible feature as, due to the strength of the energy shift, a clear trend to σ -like character can be seen.

Complementary to the XA spectra, features δ and ε for the XE spectra require special attention. They do not exist in the hydrocarbon phase, but appear upon fluorination. This coincides favourably with the disappearance of the absorption features A and B . Simultaneously, both the XA features (A , B) and the XE features (δ , ε) originate from similar MOs and I can assume a switch from unoccupied to occupied orbital region. The differences of the MOs have to be taken into account under the assumption of the intrinsic differences between occupied and unoccupied orbitals, like the electronic nodal planes and electron distribution. Accordingly, the change from unoccupied to occupied orbitals occurs due to the enormous number of additional orbitals and the different partial charge distributions based on the substitution of hydrogen by fluorine. The stronger electronegativity of fluorine results in a depopulation of most carbon orbitals, giving dominance to fluorine signals in the XE spectra. The transformation of the previous pure carbon orbitals with fluorine contribution can therefore lead to an energetic shift of the occupied orbitals due to the increase in fluorine character.

In addition to the orbital change, a σ -shifting effect is observed. This effect was already mentioned above for the σ^* features of the hydrocarbon XA spectra and is accompanied by a shift of σ -features to lower energies, when a C-C bond length increase is observed [99]. The average C-C bond length was calculated to be 1.565 Å for the perfluoroalkanes (1.559 Å for PFHex, 1.568 Å for PFHep, 1.565 Å for PFO) and 1.516 Å for the hydrocarbons (1.515 Å for hexane, 1.518 Å for heptane, 1.516 Å for octane). Note, the bond length in partially fluorinated compounds is slightly higher for bonds including fluorine substituted carbon atoms than for only hydrogen substituted carbon atoms (around 1.549 – 1.569 Å *vs.* 1.514 – 1.528 Å). Hence, the σ -shifting has only impact where fluorine substituted carbon atoms are involved. Consequently, the orbital change is strongly affected by σ -shifting, supporting and strengthening the orbital rearrangement.

As mentioned above, the frontier orbital model can be used to describe the interactions between two non-solid materials [106]. Apart from the mentioned broadening effects, a large HOMO-LUMO gap can be of importance for the chemical inertness and properties of the molecules [49, 106]. Through my presented data on chain-shaped hydrocarbons and the partially fluorinated species, I gain insight into the gap. My data supports a significant increase of the gap for the last fluorination step ($C_xF_yH_1$ to C_xF_{y+1}). For this step, the gap increases by around 2 eV due to the orbital change of the features *A* and *B* into the occupied orbital region, additionally to the systematic energy shift for these features. This increases the relative inertness according to the frontier orbital model and reveals the critical impact of the orbital change on the inertness of the perfluorinated molecule.

Additionally, parallels between the observed orbital change and molecule enhancement methods through fluorine treatment should be discussed [108, 109]. The observations are similar with respect to the observed changes in the MO structure and the resulting changes in chemical character [108, 109, 110, 111]. To enhance the mechanistic understanding and involvement of the orbital change in these methods and molecules, further research on chain structured and more complex perfluoro compounds will hopefully deliver a more general understanding of these findings.

A deeper insight into the dynamics of the local occupied states can be attained by utilising the RIXS method through enhanced site- and resonance-selectivity. The carbon K-edge RIXS spectra, as well as the theoretical XE predictions, are included in Fig. 5.7 and energetically aligned to the XA spectra. As previously stated, the XE spectra for the presented hydrocarbons are equal to a significant extend and observing the RIXS dynamics results in a similar statement. Small differences can be found, especially in the intensity ratios between features α_3 and α_4 .

Comparing the emission spectra of the first resonance feature around 287.5 eV we can

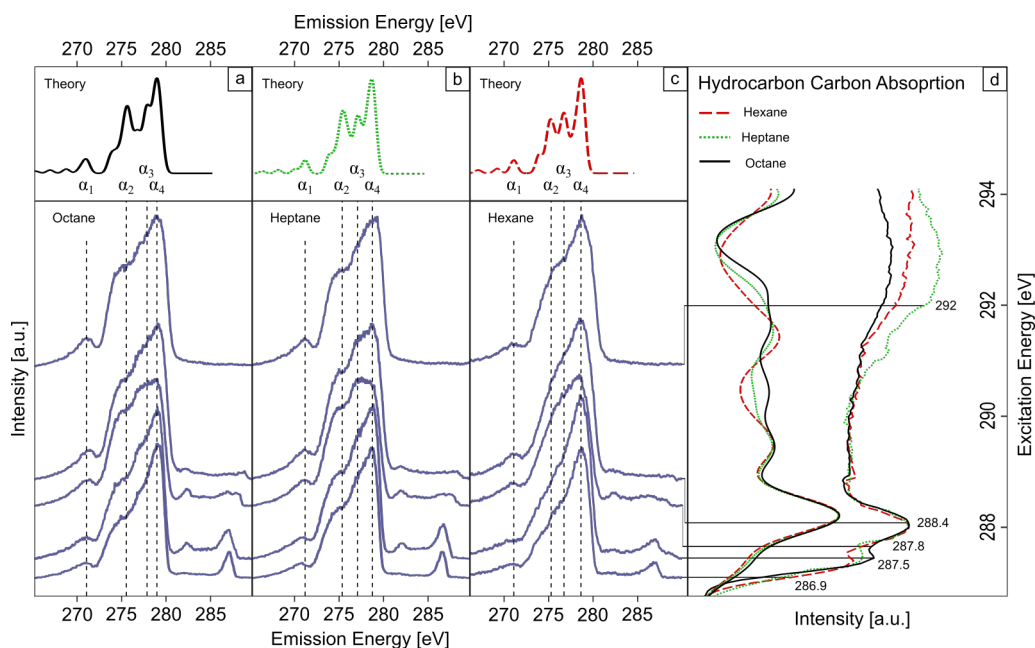


Figure 5.7: **Carbon K-edge RIXS for Hydroalkanes:** Experimental and theoretical carbon K-edge RIXS spectra for hexane (a), heptane (b) and octane (c), as well as X-ray absorption data (d). Dashed lines indicate the energetic positions of the features. The small peak above 285 eV corresponds to the elastic scattering feature in all RIXS spectra.

observe changes between the spectrum of each hydrocarbon species. As this resonance corresponds to the amount of CH_2 carbon atoms present in the molecule, as discussed above, any changes in the RIXS dynamics between the presented hydrocarbons can be attributed to the influence of changing the CH_2 -chain. The intensities corresponding to feature α_2 and α_3 are higher the longer the chain extends and subsequently support the assignment of α_2 being influenced by C-C bond interactions. As for α_3 , a correspondence to sp^3 -hybridised carbon was presented. Concerning the obtained RIXS data I can assume that α_3 is influenced by the total amount of sp^3 -hybridised carbon atoms, while the non-changing α_4 , also a sp^3 -hybridised carbon feature, corresponds to the existence of such carbon character, as described by Glans *et. al.* [107], without being significantly influenced by the amount.

A deeper look into the slope before the first resonance feature, around 286.9 eV, displays a similar behaviour as discussed for 287.5 eV, albeit with less intensity for α_2 and α_3 .

After the first resonance a valley around 287.8 eV is present, which depicts a decrease in intensity for α_4 . On a first glance one may assume that α_3 increased in intensity, but a look at the ratios between α_2 , α_3 and α_4 delivers the clear picture of α_4 losing intensity. As we just passed a resonance corresponding to the α_3 decay channel, an explanation can

be found. After passing a resonance the corresponding decay channels will be promoted, while other channels, like α_4 , become unfavourable (lower cross-section) and may lose intensity.

The last resonance at 288.4 eV restores the cross-section for α_4 , displaying a spectral structure which remains unchanged for higher excitation energies. At this energetic resonance sp^3 -hybridised carbon is favoured, which also explains why the spectrum is similar to simple fluoromethanes, as every carbon in the molecule is of sp^3 -hybridised character. Additionally, no XE feature has a higher cross-section as every feature is influenced by sp^3 -hybridised carbon character, as presented in the XES discussion.

To summarise, the RIXS dynamics present a similar picture to the previously discussed XES description. The assigned XE feature characters were supported and, in combination with the XA information, confirmation for the effects of the changes created by the chain-length increase was obtained.

The carbon K-edge RIXS spectra concerning PFHex are presented in Fig. 5.8, including theoretical predictions and energetic alignment to the XA data. The reasons behind the missing fluoroalkane data is thoroughly explained in chapter 5.1. A closer look at the XA spectrum reveals two energetic positions that require special attention: 292.8 eV and 295 eV.

The RIXS spectrum concerning 292.8 eV reveals a two-pronged structure revealing features β_2 and β_3 . We can also suspect β_1 being present, due to the non-uniform structure of the 278.8 eV peak. The differences to the theoretical XE predictions are as expected and unsurprisingly, especially the lack of β_4 and β_5 . As the transition partaking in resonance 292.8 eV does not include a mixed C-F orbital, the cross-section of such decay-channels is supposedly low. Including the previously made observations, concerning β_4 and β_5 being mixed C-F orbital transitions, a contribution of said transitions to the spectrum is negligible. The subsequent effect of missing the HOMO transitions, for this particular resonance, can be understood within the picture of the frontier orbital model [106]. As stated previously, the HOMO-LUMO gap of a liquid system is of importance to its chemical inertness and properties. Exciting the LUMO orbital resonance delivers us a local-gap increase of around 2 eV, due to the non-interference of the HOMO orbital decay-channels. Subsequently the actual local-gap to be considered is larger and only liquids with a similar sufficiently large gap can interact and mix with the presented materials.

Crossing into the valley after resonance 292.8 eV and reaching the second feature at 295 eV a significant development in the RIXS spectra can be observed. The paramount change appears in features β_4 and β_5 , which begin to appear and increase in intensity.

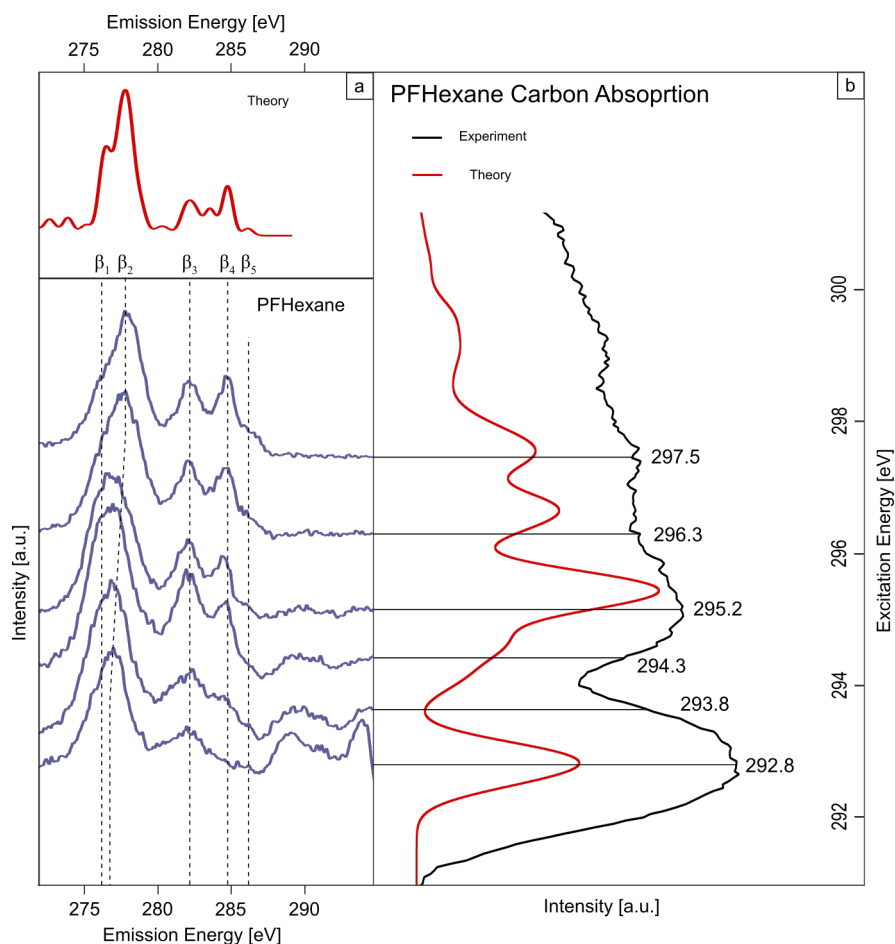


Figure 5.8: **Carbon K-edge RIXS for Perfluoroalkanes:** Experimental and theoretical carbon K-edge RIXS spectra (a) and X-ray absorption data (d) for perfluorohexane. Dashed lines indicate the energetic positions of the features.

Especially β_4 rises significantly, which can be explained through the total number of CF_2 carbon atoms, as discussed previously. The increase of these features can be attributed through the mixed C-F orbital character of resonance 295 eV, which corresponds to the character of the decay-channels.

I note, that throughout the RIXS spectra 292.8 eV until 295 eV an additional peak structure at 289 eV can be discovered. Theoretical predictions assume no spectral contribution of the given material at this position. The most probable origin for this peak are vibrational states, which occur on the low-energy side of the elastic feature, or effects created through higher order harmonics of the beamline. Another probable effect could be an inter-liquid interference structure, but the profoundness of the feature suggests otherwise. Overall no clear explanation can be found and will be subject to future

investigations.

Through high similarities between the theoretical predictions of the hydro- and fluoroalkane carbon K-edge emission and absorption features, I can interpolate similar spectral developments for the missing experimental data. Especially the proceedings concerning the RIXS spectra should be complementary, as the molecular structure change is negligible and the overall peak assignments are unequivocal identical. Including the data presented by Hitchcock *et. al.* for more simple alkanes [100], I can extrapolate the here presented conclusions and analytical methodology onto longer chain-type hydrocarbons with similar molecular structure and conclude my findings as general for sufficiently short hydro- and fluoroalkanes.

The Fluorine K-Edge

The previous chapter discovered the effects of the carbon K-edge onto the peculiar character of hydro- and fluoroalkanes. Simultaneously, a "shielding" effect for the presented samples originating from the fluorine encasing of the carbon atoms was hypothesised and confirmed. A closer look onto the fluorine K-edge will subsequently deliver more insight into this effect and the resulting conclusions drawn towards the chemical and biological inertness of the materials.

The fluorine K-edge XA spectra for PFHex, PFHep and PFO are presented together with theoretical predictions in Fig. 5.9a. On a first glance the spectra seem to show saturation effects [112, 113], as the fluorine K absorption dominates the absorption cross-section above the edge, as well as the missing feature distinctions provided by the theoretical predictions. On the other hand, the spectra were obtained through transmission mode measurements, as described in chapter 4.2. Such measurements are not reliant on the yield of secondary particles to monitor the absorption cross-sections, which directly rules out the effect of saturation, as it occurs when the secondary photons, which have energy below the edge, are not reabsorbed and the contrast is lost.

The spectra deliver two main features: a peak at 690.3 eV and a broad band above 691.8 eV. Theoretical predictions reproduce the general spectral shape of the XA spectra and can be utilised to assign the broad band feature. The band above 691.8 eV can be uniformly assigned as σ^* (C-F) shape resonances originating principally from two transitions, where one is incorporating an additional π (F-F) contribution. Theoretical predictions assume the peak at 690.3 eV to be a two-pronged structure, which also explains and predicts its energetic shift of 100 meV. The main feature predicted at around 690.2 eV until its shift towards 690.3 eV is assumed to be transitions to the same orbital responsible for the peak broadening of the perfluoroalkane carbon XA LUMO feature, as described above (see Fig. 5.9c). It was confirmed that this orbital is heavily influenced by the distortions of the different conformational geometries, resulting in the peak broadening change. Concerning the fluorine K-edge, we observe that theoretical calculations accurately predict the energetic shift and can therefore rule out the involvement of conformational geometries towards this shift. A direct look at the orbital reveals a π^* (C-F) character involvement, which is overall less affected by changes in the geometric conformations of the molecule.

The orbital involved in the low energy shoulder around 689.6 eV is again a known orbital originating from π_x (C-C) and π^* (C-F) character. Additionally a small π (F-F) contribution can be confirmed. In the carbon XA section I established the fact that both orbitals are affected by the chain-length and therefore the amount of (CF_2) carbons.

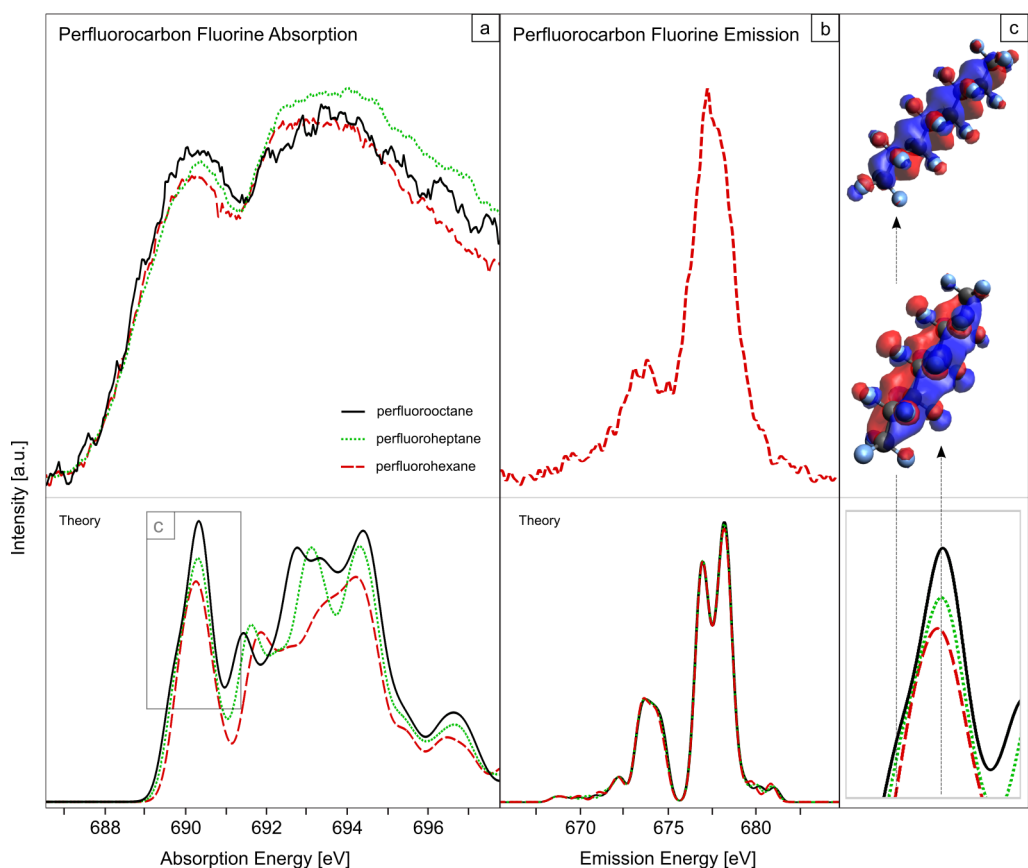


Figure 5.9: **Fluorine K-edge Data for Perfluoroalkanes:** Experimental and theoretical fluorine K-edge X-ray absorption data for chain-shaped perfluoroalkanes (a) and their respective X-ray emission data (b). The inset (c) represents the main areas of change in the experimental spectra and illustrate the molecular orbitals for the corresponding transitions.

Subsequently, the increase in intensity from PFHex to PFO can be attributed to such. Note that, the predicted main-feature transitions have a stronger intensity rise due to its orbital shape being more favourable for transitions from fluorine 1s core-orbitals. The energetic shift on the other hand requires a discernment of the actual energetic positions of the transitions. The shoulder transition is predicted to occur at 689.6 eV uniformly (experimentally at 689.6 eV), while the main feature is predicted to occur at 690.35 eV for all perfluoroalkanes (experimentally at the 690.2 eV - 690.3 eV interval). As a result of the non-uniform intensity increase between both features, a shift from lower energies to higher ones occurs. We can assume, that for sufficiently long chain-type perfluoroalkanes, the feature stabilises around 690.35 eV in the predictions.

Comparisons of the different predicted fluorine K-edge XE spectra of the perfluoroalkanes (Fig. 5.9b) reveal an astonishing overall similarity, leading to the calculations being

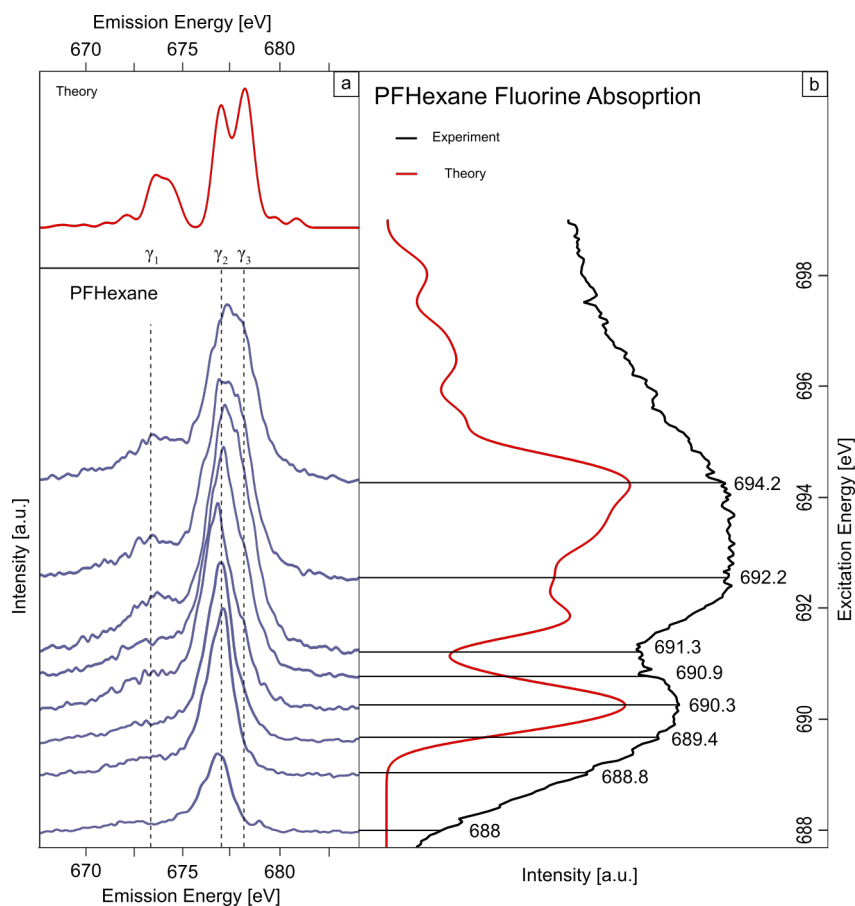


Figure 5.10: **Fluorine K-edge RIXS for Perfluoroalkanes:** Experimental and theoretical fluorine K-edge RIXS spectra (a) and X-ray absorption data (d) for perfluorohexane. Dashed lines indicate the energetic positions of the features.

basically equal. The three-pronged prediction is also confirmed by the experimental PFHex spectrum. While the experimental spectrum only reveals two features, the effect of the third peak can be confirmed in the RIXS dynamics spectra later on, confirming the validity of the theoretical predictions. The low-energy peak at 673.7 eV (γ_1) can be attributed to orbitals mixed with carbon sp^3 valence character, in analogy to the methodology used for the carbon XE spectra, utilising the simple fluoromethanes CH_2F_2 and CHF_3 [107]. The main peak originates from local F p character dominated states, revealing the predicted double peak structure due to different F p characters. The low-energy feature around 677.2 eV (γ_2) emerges from F p characters perpendicular to both the (C-C) and the (C-F) axis, while the high-energy feature at 678 eV (γ_3) arises from F p characters perpendicular to the (C-C), but parallel to the (C-F) axis.

A glimpse at the HOMO-LUMO gap observed by the fluorine data reveals a gap of more

than 10 eV (carbon data provides a gap around 6-7 eV), which in the frontier orbital model correlates to a high chemical inertness and an inability to mix with standard solvents like water and ethanol [106]. Subsequently, the high experimentally observed inertness and special mixing dynamics of the perfluoroalkanes can be explained through it, as the previously described "shielding" effect of the fluorine atoms (inhibition of exchange interaction between carbon atoms and other solvents) was confirmed with this data. As both the carbon and fluorine data of all presented perfluoroalkanes provides evidence for the "shield" being part of the reason for the relative inertness, I conclude this "shielding" effect as playing a part in the inertness of all chain-type perfluorinated materials.

RIXS data concerning the fluorine K-edge of PFHex is presented in Fig. 5.10 together with theoretical predictions and energetic alignment complementing the XA data. At low energy excitation we observe a sharpening of the F K emission main peak around 677.2 eV. This directly correlates to the previously mentioned low-energy feature γ_2 of the fluorine XE spectra and was anticipated from the orbital characters involved in the excitations below 689.4 eV and the corresponding decay-channels. The F p character involved in the predicted high-energy emission feature γ_3 , on the other hand, is correlated to the XA resonance around 690.3 eV and should gain intensity at higher excitation energies.

As predicted, an asymmetry is occurring in the main emission feature upon passing the 689.4 eV excitation, hinting at an intensity gain for γ_3 . Subsequently, the existence of γ_3 is confirmed. Note however, that the main emission peak has a low energy shift also for excitations as high as 691.3 eV, where I find it unlikely that the γ_2 decay-channel is dominating, as theory predicts otherwise. Therefore, I believe that the coupling with the excited electron must also be important at these energies. Such an influence of the core-hole potential is indeed supported by the calculations delivering excitonic effects.

In a similar manner to the carbon K-edge emission and absorption features, I can interpolate equal spectral developments for the missing experimental PFHep and PFO fluorine data. Extrapolating the found developments, through the help of the data presented by Hitchcock *et. al.* [100], we can assume the "shielding" effect occurring for all chain-type perfluorinated materials and generalise the constructed analytical methodology concerning XE, XA and RIXS data of sufficiently short chain-type hydro- and perfluorocarbons.

Summary

Fundamental insights and a comprehensive picture of the electronic structure of hexane, heptane and octane as the parent molecules, as well as their respective perfluorinated counterparts, were presented based on XA, XE and RIXS spectroscopic data. In addition DFT calculations for the hydrocarbons, the stepwise fluorinated hydrocarbons and the perfluorocarbons were performed. Additional insights into the energy shift induced by fluorination, the so-called perfluoro effect, were drawn and these provided significant connections to previous works. We observed changes in the electronic structure due to the conformation effect induced by the increase of (CH_2) - and (CF_2) -chains for the investigated molecules and detected that different conformational geometries mainly influence the chemical and electronic interaction between the molecules. Subsequently, that may be one of the main reasons for the slight differences in chemical and biological character of the presented liquid materials. Interestingly, the conformational geometries can greatly influence the LUMO of the perfluorocarbons leading to an impact on the dissolving capacity with other materials like water. As a full understanding of the gas dissolving capacity of perfluorocarbons was not found until this date, to my knowledge, a deeper investigation into this conformation effect and its extension to larger, more complex perfluoro systems and gas-loaded samples is of particular interest for medical applications like blood substitute formulations and liquid breathing [1, 2, 15, 16]. We observed a change in occupancy of MOs occurring for the fluorinated hydroalkanes upon reaching complete fluorination. This MO alteration may be one of the main reasons for the chemical and biological inertness of the chain-shaped perfluorocarbons compared to their parent molecules and the corresponding partially fluorinated hydrocarbons. To the best of my knowledge, the observability of the perfluoro effect *via* XE spectra was confirmed for the first time, and the orbital change originating from unoccupied hydroalkane to occupied fluoroalkane MOs was also discussed in relation to the well-known high electronegativity of fluorine atoms. Hence, the validity of this concept and its extension to ring and also larger perfluoro systems is of particular interest for a better understanding of the special properties of perfluoro compounds and their application development. Additionally, a "shielding" effect can be described for the presented samples and I conclude that one reason for the high relative inertness of chain-type perfluorinated materials is that the "shield" is inhibiting interactions. In summary the validity of various concepts was confirmed and their observability in linear perfluoro systems presented a deeper insight into the basis of the relative inertness and the special properties of perfluoro compounds and their possible applications.

5.3 Non-Aromatic Ring-Shaped Hydro- and Perfluorocarbons

5.3.1 Decalin and Perfluorodecalin

The Carbon K-Edge

As previously mentioned, perfluorocarbons have interesting chemical properties and diverse applications in biomedicine, physical chemistry and polymer science. Therefore, Carbon K-edge absorption and emission spectra of liquid samples were performed to give a comprehensive picture of the electronic structure based on soft X-ray absorption and emission spectroscopies. In this chapter I will concentrate on perfluorodecalin (PFD), which is often studied as a general model system for ring-shaped perfluorocarbons, as it exhibits the special chemical properties of perfluorocarbons and is frequently used in applications. As such, I hope to recreate the effects observed and introduced in chapter 5.2 for chain-shaped perfluorocarbons. I note, that PFD exhibits cis-trans isomerism, but, as no significant spectral differences were found through theoretical predictions, a combined 50-50 cis-trans configuration is assumed and depicted as given by the sample provider.

The experimental carbon K-edge XA spectrum of decalin (Fig. 5.11a) reveals two peaks at 287.2 eV and 288.7 eV followed by a broad feature extending from 291 eV to 294 eV. The general spectral shape of the XA spectrum of decalin can also be reproduced in shape and energetic position by theoretical predictions. Nevertheless, the neglect of intermolecular interactions inside the liquid probably leads to the different intensity ratios for the two peaks at 287.2 eV and 288.7 eV by comparing theoretical and experimental data.

The XA spectrum comprises transitions of many non-equivalent carbon sites and one may have suspected most spectral fine structures to be washed out. Note, however, that most carbon atoms have a similar chemical environment, with the same sp^3 -hybridisation, as well as two hydrogen atoms and two carbon atoms (dC) as nearest neighbours (Fig. 5.1). One could reasonably expect the spectra associated with the core-levels of these atoms to be similar. The chemical environment of the two carbon atoms (sC) connecting the rings is equivalent, but significantly different from the dC atom environment, as they have three carbon atoms and only one hydrogen atom as nearest neighbour. The resulting spectral differences suggest separate theoretical calculations for the dC and sC sites, which are additionally presented in Fig. 5.11a. Note

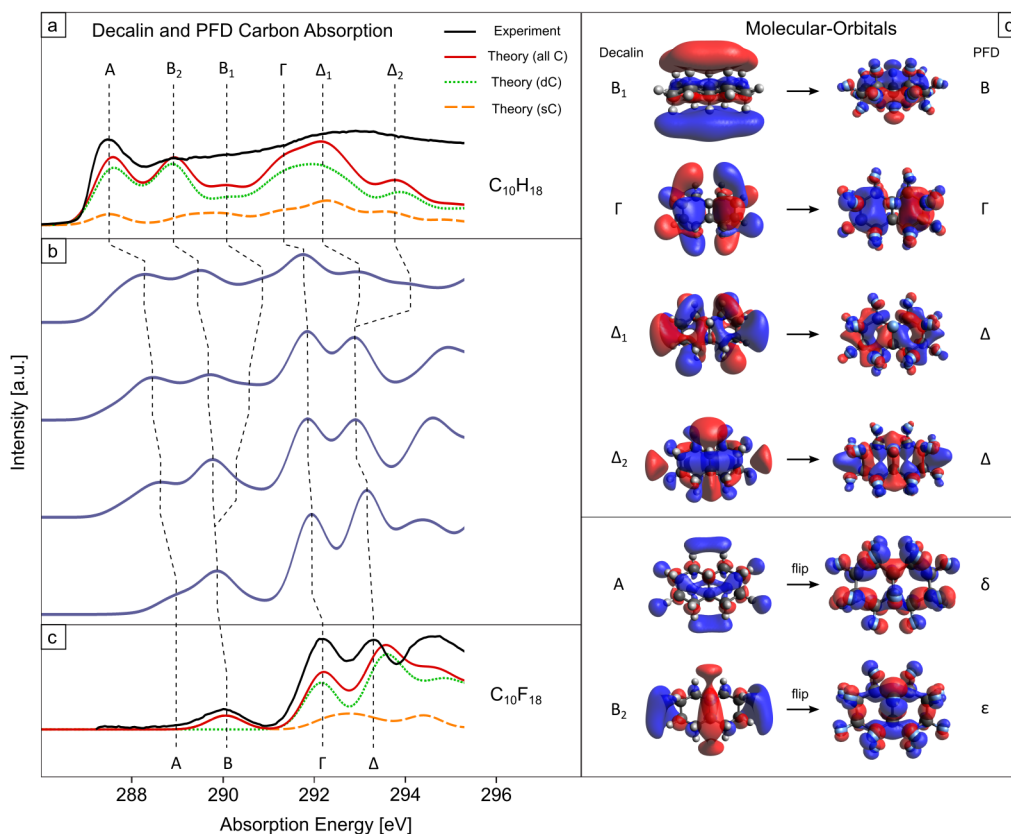


Figure 5.11: **Carbon K-edge Absorption for Decalin and Perfluorodecalin:** (a) and (c) show the experimental (black lines) and calculated carbon K-edge X-ray absorption spectra for decalin and PFD. Theoretically calculated data are shown for different carbon sites. The calculated spectra for the stepwise fluorinated decalin derivatives are additionally depicted in (b), utilising dashed lines to indicate the shifts of the spectral features. MOs for decalin and PFD corresponding to the shifting features are labelled in (d).

that, the two different carbon atom sites in decalin mainly differ by the number of bound hydrogen atoms.

Eight carbon atoms are bound as dC type carbons, while the two carbon atoms connecting the rings are bound as sC type, resulting in a statistical weight of (1/4). The corresponding theoretical spectra were obtained through the sum of the spectra for all dC and sC sites respectively and depict, surprisingly, a similar spectrum for dC and sC sites. This is in contrast to the findings for PFD, as will be presented later. A deeper look at the net charge on the carbon atoms reveals quite similar charges (0.21-0.23 for dC and 0.20 for sC), resulting in almost identical spectra.

A comparison to the XA spectra of simple ring-shaped fluorocarbons, like cyclo-hexane,

is helpful for the general understanding of the decalin spectra [93]. Hitchcock *et al.* reveal a basic three-pronged structure: two peaks corresponding to σ (C-C) and π^* (CH_2), as well as a σ^* shape resonance related to σ^* (C-C) transitions. This picture is also fully in line with the provided theoretical predictions, albeit differences in peak positions and intensities have to be taken into account with regard to the increased complexity of the decalin molecule. Thus, the spectral structures can be assigned accordingly.

The carbon K-edge XA spectrum of PFD (Fig. 5.11c) shows a rich structure with an isolated peak at 290 eV, followed by a broad band exhibiting at least six intensity maxima up to 300 eV. The spectrum shows some similarities to spectra of other sp^3 -hybridised fluorocarbons, with the carbon K-edge situated at an unusually high energy. This can be mainly attributed to the large core-level chemical shift, due to the electronegativity of the fluorine neighbours. The spectrum differs substantially, however, from XA spectra of fluorobenzenes, which are dominated by an intense peak at lower energies, assigned to a π^* excitation with respect to C-C bonds. Seemingly, the core hole in the PFD double-ring cannot localise the lowest unoccupied molecular orbital (LUMO) in the same way as in fluorobenzene and therefore the oscillator strength for the first absorption transition is much lower.

In line with the above mentioned splitting of the carbon atoms in dC and sC configurations, theoretical predictions for sC and dC PFD were prepared. While, for decalin, the differences between the carbon sites were negligible for the overall carbon spectra prediction, a different picture reveals itself for PFD. Here the hydrogen was exchanged for highly electronegative fluorine, which quenches the electron distribution stronger than hydrogen, leading to significantly different chemical environments. Referring to the net charge of the carbon atoms, a clear difference between the molecules can be discovered. While for decalin, as depicted above, the net charge on the carbon atoms is quite similar (0.21-0.23 for dC and 0.20 for sC), in PFD a slight net charge difference for dC and sC atoms (0.26-0.27 for dC and 0.16 for sC) can be observed. I believe that the difference for the two carbon sites can mainly be attributed to this charge difference, as it influences the electron distribution in the molecule. Additionally, I note that, the differences between net charges for decalin carbons and PFD carbons (decalin charge being positive, while PFD is negative), occur due to the substitution of hydrogen to highly electronegative fluorine. Subsequently, the fluorine influence is smaller for sC sites, compared to the dC atoms, and a correspondingly smaller core-level chemical shift suggests that the resonance at lowest energy may be associated with excitations at the sC sites.

A comparison to the XA spectra of simple fluoromethanes is helpful for the general understanding of the PFD spectra. In these compounds the valence is typical of carbon

sp^3 -hybridisation and, like for sC carbons, there is one C-F bond in CH_3F , whereas, like for dC carbons, there are two C-F bonds in CH_2F_2 . Therefore I expect the local electronic structure to show similarities. Indeed the LUMO transition in the carbon K-edge absorption spectrum of CH_3F is found just below 289 eV, whereas the corresponding transition in CH_2F_2 appears around 292 eV. The Rydberg series, which are prominent for the small molecules, have no correspondence in liquid PFD.

This picture is fully in line with the theoretical predictions (see Fig. 5.11c). In general the theory predicts the overall spectrum qualitatively well with the pre-peak and a broad structure with six maxima at appropriate energy positions, albeit with differing intensities. The theory indeed assigns the first peak to transitions to the lowest unoccupied orbital (LUMO) from core levels of the sC atoms. The predicted difference in chemical shift between dC and sC atoms is 1.9 eV and judging from the FY spectra the difference may be a little larger. Note also that the relative weight of the LUMO is larger in the theoretical sC spectrum than in the dC spectrum. As we shall see later also excitonic effects must be taken into account for a full understanding of the spectrum.

Fig. 5.11b shows the predicted carbon K-edge XA spectra of stepwise fluorinated decalin derivatives. Combined with Fig. 5.11a and c, the figures visualise the shifts of the four main features. As mentioned above, according to the dimensions of the shifts for these features it is common to assign directly a σ - or π -character for the participating orbitals (2-4 eV corresponds to σ , 0-0.5 eV corresponds to π) [23], where π is of out-of-plane and diffuse (Rydberg-like) character, but not of anti-bonding character like π^* . The information is summarised in Table 5.3.

feature	energy shift upon complete fluorination [eV]	orbital character
A	1.8	σ
B_1	0.3	π
B_2	1.3	not distinguishable
Γ	0.9	not distinguishable
Δ_1	1.4	not distinguishable
Δ_2	0.1	π

Table 5.3: **Perfluorodecalin XA Carbon K-edge Character Table:** Energy shifts and derived MO characters for the XA features.

Features A and B_2 are special due to their disappearance in the spectra of PFD. All other calculated fluorocarbons show these features even though their intensity decreases with increasing number of fluorine atoms. Furthermore, these features do not have

corresponding PFD orbitals for the absorption process. One can assume a MO transfer in a similar fashion to the presented orbital change in fluoroalkanes (see chapter 5.2). More discussion on this transfer follows at the XE spectra discussion. I additionally note that B_2 only loses its dC contribution to the spectrum, while the sC contribution remains of the same intensity.

Features B_2 , Γ and Δ_1 can only be assigned to both σ - and π -orbital character, since the observed energetic shift is in the range known for strong σ - π -hybridisation. According to the relative high values of 1.3 eV and 1.4 eV for B_2 and Δ_1 , respectively, a larger contribution of σ -character for these features can be assumed in comparison to Γ with a value of 0.9 eV for the energetic shift.

In addition to the possible orbital change, a σ -shifting effect is observed. This σ -shifting effect was already introduced for chain-shaped hydrocarbons in chapter 5.2. I want to exemplify that the aforementioned shifting effect is known to occur in hydrocarbons regardless of shape and aromatic status [99]. The average C-C bond length for PFD was here calculated to be 1.565 Å and 1.533 Å for decalin. Note, the C-C bond length in partially fluorinated compounds is slightly higher for bonds including fluorine substituted carbon atoms than for only hydrogen substituted carbon atoms (around 1.545-1.565 Å vs 1.529-1.534 Å). Hence, the σ -shifting has only impact where fluorine substituted carbon atoms are involved. This development is in accordance with the observations of chain-shaped fluorocarbons and I assume a confirmation and subsequent generalisation of mentioned affairs.

In the previous chapter I found that perfluoroalkanes have a large HOMO-LUMO gap, supposedly of importance for the chemical inertness and properties of the presented materials. Utilising the data on decalin, PFD and the partially fluorinated hydrocarbons, we gain insight into the mechanism behind this process for ring-shaped fluorocarbons. My data supports a significant increase of the gap for the last fluorination step ($C_{10}F_{26}H_2$ to $C_{10}F_{28}$). For this step, the gap increases by 1.2 eV, due to features A and B_2 vanishing, additionally to the systematic energy shift for these features. As a result, this increases the relative inertness according to the frontier orbital model [106].

I note, that all developments shown for PFD and decalin reveal significant similarities to the XA characteristics of the presented fluoroalkanes (see chapter 5.2). Consequently, we can assume that the "shielding" effect of fluorine substituted samples, as well as the orbital change effect, also occur in non-aromatic ring-shaped fluorocarbons. Further discussions on the XE region of PFD and decalin are needed to fully support this hypothesis.

The experimental carbon K-edge XE spectra of decalin (Fig. 5.12a) are in good agree-

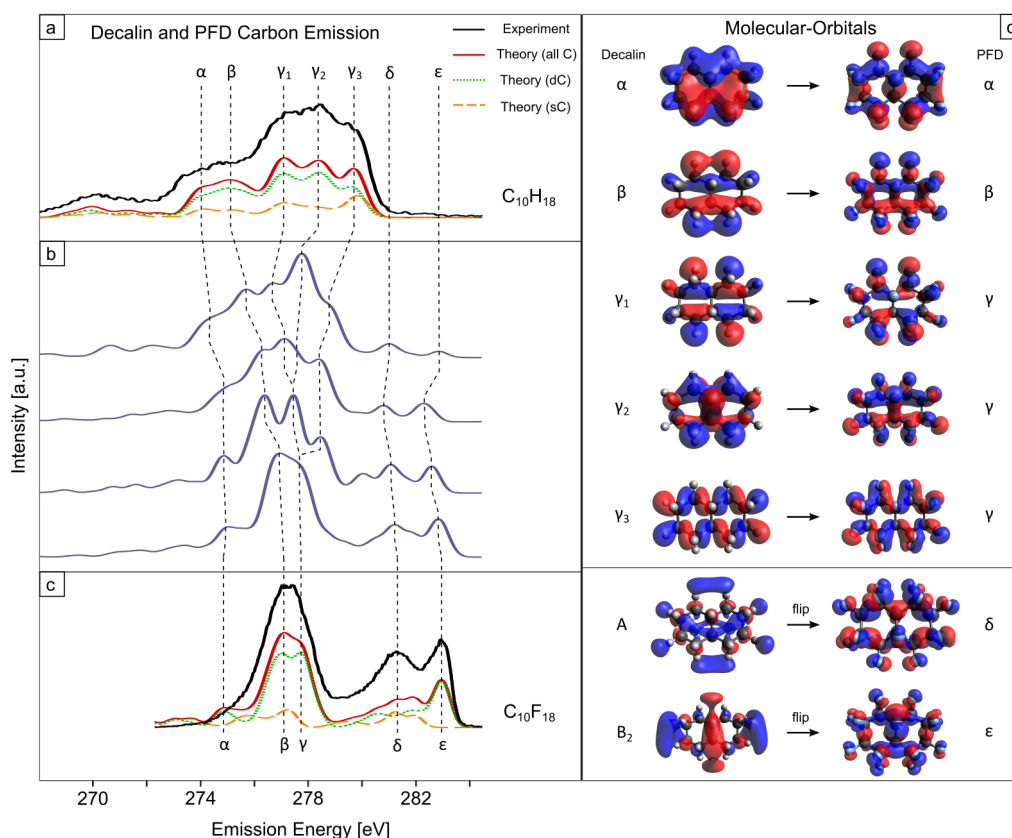


Figure 5.12: **Carbon K-edge Emission for Decalin and Perfluorodecalin:** (a) and (c) show the experimental (black lines) and calculated carbon K-edge X-ray emission spectra for decalin and PFD. Theoretically calculated data are shown for different carbon sites. The calculated spectra for the stepwise fluorinated decalin derivatives are additionally depicted in (b), utilising dashed lines to indicate the shifts of the spectral features. MOs for decalin and PFD corresponding to the shifting features are labelled in (d).

ment with the calculated predictions. By comparing to XE spectra of rather simple fluoromethanes a classification methodology was developed in previous chapters (see chapter 5.2), giving rise to similar proceedings for ring-shaped perfluorocarbons and their parent molecules. Subsequently, the carbon K-edge emission spectrum of CH_4 should reveal similarities to decalin due to the absence of fluorine atoms and the sp^3 -hybridised carbon character. Indeed, CH_4 shows one broad feature around 277 eV, which is an indicator for sp^3 hybridised carbon [107]. Additionally, the spectra of C_2H_6 and C_3H_8 reveal an additional shoulder compared to the carbon XE spectra of CH_4 at around 274.8 eV [91]. This shoulder can be attributed to C-C bond interactions and coincides with the decalin α/β structure at 274.6 eV.

As expected, the methodology, as well as the spectral composition, are complementary to chain-shaped perfluorocarbons, exhibiting a broad peak with two features, albeit with small energetic shifts that need to be accounted for. Anyhow, due to the phenomenological similarity to simple and chain-type hydrocarbons, I can assign γ_1 , γ_2 and γ_3 as sp^3 -hybridised carbon structures and the shoulder α/β as resulting from C-C bond interactions.

Carbon K-edge XE spectra for PFD are compared to predictions in Fig. 5.12c. The spectra reveal a broad band around 275 eV (β/γ), a sharper high-energy peak at around 281 eV (ε), and a local maximum in-between at 279 eV (δ). Again, the overall shape can be understood by comparing to the XE spectra of gas-phase fluoromethanes [107] and chain-shaped fluorocarbons. Like dC PFD carbon atoms, the CH_2F_2 carbon valence shows sp^3 -hybridisation and the carbon atom binds two fluorine atoms. Consequently, one may expect corresponding similarities in the local electronic structure. Indeed, the C K emission spectrum of the CH_2F_2 molecule shows, like PFD, a three-peak structure: a broader peak at lower energies (277 eV), typical for sp^3 -hybridised carbon, a sharper high-energy (283 eV) peak, due to a mixed C-F orbital, and a peak at intermediate energies (281 eV), where the orbitals predominantly have fluorine character. The similarities between the two spectra suggest an overall assignment, accordingly. Note that, the overall similarity to chain-shaped hydro- and fluorocarbons is striking and we may expect similar developments.

feature	energy shift upon complete fluorination [eV]	orbital character
α	0.9	not distinguishable
β	2.1	σ
γ_1	0.7	σ / not distinguishable
γ_2	0.6	not distinguishable
γ_3	1.9	σ
δ	0.2	σ
ε	0.1	not distinguishable

Table 5.4: **Perfluorodecalin XE Carbon K-edge Character Table:** Energy shifts and derived MO characters for the XE features.

Complementary to the investigations of the XA spectra, features δ and ε for the XE spectra (Fig. 5.12b) require special attention (see also Table 5.4). They do not exist in decalin but appear upon fluorination. This coincides favourably with the disappearance of the absorption features A and B_2 . Similarly, both the XA features (A , B_2) and the XE

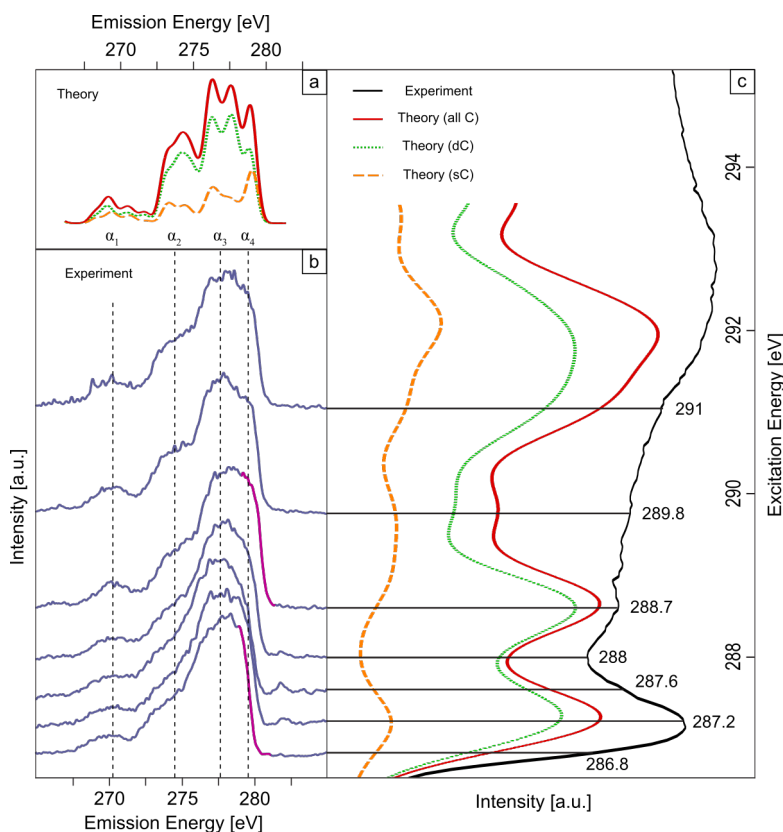


Figure 5.13: **Carbon K-edge RIXS for Decalin:** Experimental (b) and theoretical (a) carbon K-edge RIXS spectra and X-ray absorption data (c) for decalin. Theoretically calculated data are shown for different carbon sites. The highlighted edges in the RIXS spectra (b) indicate the excitation-energy dependent spectral features. Dashed lines additionally indicate the energetic positions of the features.

features (δ , ε) originate from similar MOs and we can assume a switch from unoccupied to occupied orbital region. Accordingly the change from unoccupied to occupied orbitals occurs in similar fashion to the previously introduced MO change in chapter 5.2. I note, that feature δ is a mixture of sC and dC carbon sites and ε of only dC carbon sites, which should lead to differences in intensities concerning the RIXS excitation of the pre-peak, as it only corresponds to sC sites. The previously mentioned σ -shifting effect also supports the orbital rearrangement, as shown in the XA spectra discussion.

This, in addition to the gap increase, reveals the generality of the orbital change concepts established in chapter 5.2, leading to the critical impact of the orbital change on the inertness of the perfluorinated molecule in accordance with the frontier orbital model [106]. Additionally, the striking resemblance of the spectral properties and assignment procedures of the, hitherto, presented fluorinated materials leads to a conclusive general

procedure for the spectral analysis of fluorinated materials. I assume that sufficiently simple fluorinated hydrocarbons can be investigated by the presented procedures until now.

The RIXS spectra of decalin (see Fig. 5.13) are overall uneventful. The spectral structure changes insubstantially and remains unchanged for excitation energies higher than 288.7 eV. This effect can be attributed to so-called tail excitation and vibronic coupling effects.

Notable is the excitation-energy dependence in the range of 286.8-288.7 eV, where the high energy shoulder (α_4) at 279.6 eV emission energy gains intensity. The corresponding resonance was assigned to a dC-sC mix transition, which coincides with the complementary decay-channel for α_4 , as seen by the theoretical predictions. For a more in-depth analysis, an observation of the involved orbitals is essential. Comparing the orbital responsible for the excitation (see Fig. 5.11d, orbital B_2) with the one involved in the decay-channel (see Fig. 5.12d, orbital γ_3), we can observe similarities, which lead to the promotion of α_4 . Both orbitals incorporate σ (C-C) character, leading to a corresponding and subsequent energy-excitation dependence.

As noted above, excitation at the XA pre-peak of PFD mainly selects sC atoms, e.g., carbon atoms which bind only one fluorine atom, and the corresponding emission spectrum should differ radically from the high-energy excited spectra. To support this statement, a conclusive RIXS study of PFD is needed (see Fig. 5.14). At the pre-peak resonance, the low-energy feature (β_1) seems to split into a double structure peaking at 273.5 eV and 276 eV, the intensity of the high-energy feature (β_3) is suppressed and the local maximum at intermediate energies (β_2) is shifted from 279 eV to 278 eV. Assuming that the coupling to the excited electron is small and that the emission is typical for ionisation at sC sites, one would expect a local electronic structure that simulates the carbon site in CH_3F [107]. Indeed, the CH_3F carbon K-edge emission spectrum is lacking the high-energy peak of the CH_2F_2 spectrum and comprises of two rather broad features at 276.5 eV and 280 eV, the first again, reminiscent of sp^3 -hybridised carbon and the second peak being due to an F-C anti-bonding orbital. Although the PFD spectrum is more complex, with a split low energy peak, the similarities in the phenomenology are striking.

I note that there is a steep excitation-energy dependence for the spectra excited in the range of 292.3-294.9 eV. The main changes comprise of a gradual high-energy shift and intensity-increase of the high-energy flank so that the high-energy excited spectrum is retrieved at an excitation energy of 296.6 eV. The shift of the high-energy flank from the lowest to the highest excitation energy can be explained by the difference in the core-level chemical shift and the appearance of an additional feature when going from sC to

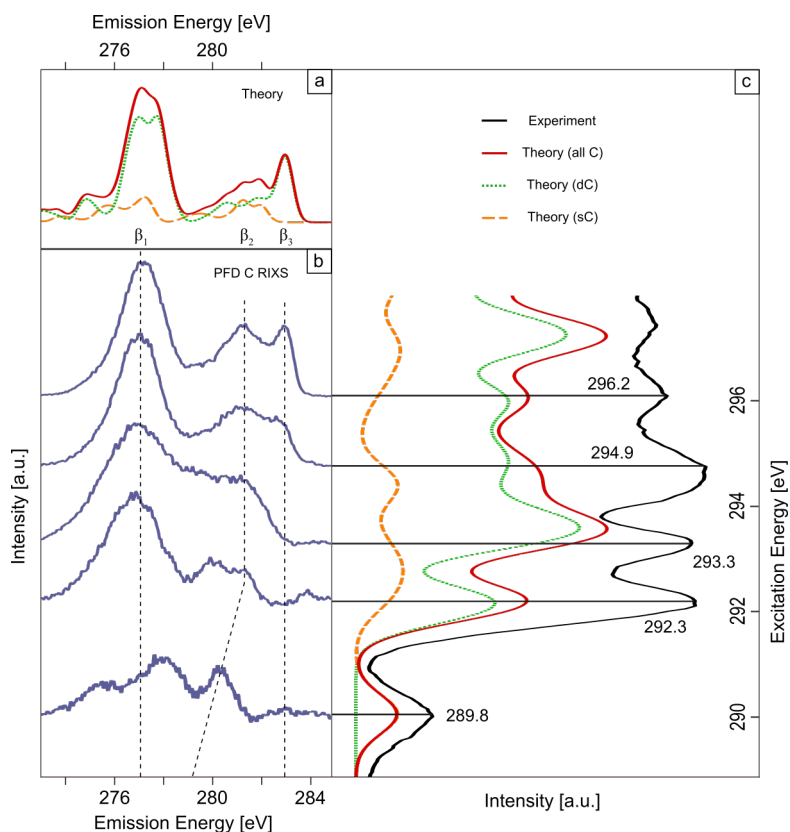


Figure 5.14: **Carbon K-edge RIXS for Perfluorodecalin:** Experimental (b) and theoretical (a) carbon K-edge RIXS spectra and X-ray absorption data (c) for PFD. Theoretically calculated data are shown for different carbon sites. Dashed lines indicate the energetic positions of the features.

dC atom sites. However, site-selective excitation cannot fully explain the details in the excitation-energy dependence. The three-pronged structure with the most intense peak at 275.5 eV in the spectrum excited at the lowest excitation energy is not predicted by sC site XE theory, whereas the double structure at 278-279 eV in the spectrum excited at 292.3 eV seemingly corresponds to a feature in the theoretical sC spectrum. The XE theory does not support any appreciable site-selectivity for excitation energies in the 292.3-296 eV region, where the XE spectrum is excitation-energy dependent. Instead, I attribute the observed excitation-energy dependence to excitonic effects, e.g., and that the electron excited in the first step influences the emission spectrum.

The aforementioned RIXS measurements also coincide with the statement provided above, in which the feature δ and ϵ (β_2 and β_3 accordingly) shall have different intensities upon excitation of the pre-peak feature. As ϵ is comprised of solely dC contribution, the suppression is within the scope of the argument, confirming the observations reached through the orbital change and energetic shifts of the XA spectra.

The Fluorine K-Edge

In the previous part I established the fact that unequal carbon sites, called sC and dC, deliver vastly different spectral predictions and can help analyse and interpret the experimental observations. Site-selective excitations and their corresponding decay-channels were discovered further increasing the insight into the material. I note that two of the fluorine atoms (sF) differ from the others (dF) in that they bind to the sC atoms, resulting in their next-nearest neighbour not being another fluorine atom. The fluorine atoms in PFD can therefore also be separated in sF and dF sites accordingly.

The fluorine K-edge XA spectrum (see Fig. 5.15c) reveals a first peak at around 690 eV followed by broad band extending up to 700 eV, which can be compared to predictions. The theoretical calculations deliver a more feature-rich picture, but the overall spectral shape and energetic positions can be assumed. Additionally, the theory predicts for the core-level of the sF atoms a different chemical shift than for the dF core-levels by 0.7 eV, which leads to a corresponding shift. When comparing the sF and dF absorption spectra, shown in Fig. 5.15c, their statistical weight (1/8) has to be taken into account. In the experimental spectrum there is a faint low-energy shoulder at around 688 eV, which may be attributable to the sF sites.

The theoretical calculations predict the sF and dF spectra to be marginally different, with respect to their intensity ratios and feature positions. In the former, transitions to the LUMO seem to dominate the spectrum, giving little intensity in the region of the most intense dF peak. This suggests that the local character of the unoccupied orbitals varies over the molecule and, as we shall see below, also excitonic effects are important. I note, that the net charge distribution between the different fluorine sites is negligible (-0.13 for dF and -0.15 for sF), resulting in similar electron distribution environments.

The first peak around 690 eV is built upon a two-pronged structure, as revealed by theory. The main transition is attributed to π^* (C-F), through the help of the predicted spectrum, revealing similarities to chain-shaped perfluorocarbons, where the first main resonance is also of π^* (C-F) character. Additionally I attributed the faint shoulder around 688 eV to sF sites, which is partly characterised through the XA predictions and will be further confirmed in the RIXS discussion. The orbital involved in this transition reveals σ^* (C-F) character, depicting the influence of the slight fluorine site net charge difference on the predicted energetic position. As σ -bonds are more substantially affected by the net charge barrier between the carbon and fluorine bond, in comparison to π -orbitals, we can expect shifts if the barrier is significantly different. Indeed, the sC-sF barrier (0.31) is lower by a net charge of 0.08, compared to the dC-dF barrier

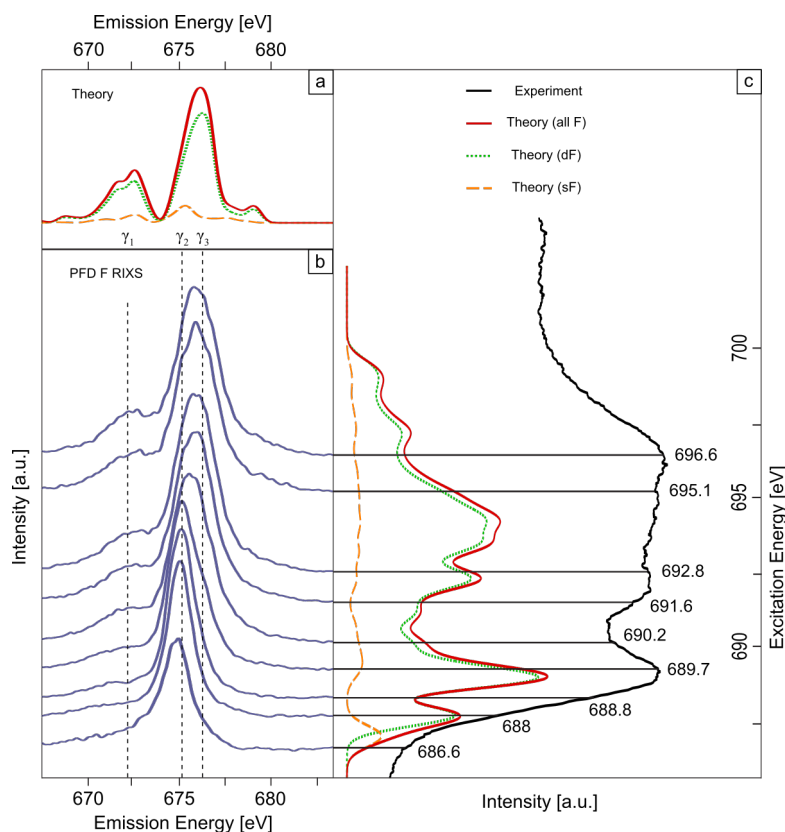


Figure 5.15: **Fluorine K-edge RIXS for Perfluorodecalin:** Experimental (b) and theoretical (a) fluorine K-edge RIXS spectra and X-ray absorption data (c) for perfluorodecalin. Theoretically calculated data are shown for different fluorine sites. Dashed lines indicate the energetic positions of the features.

(0.39), resulting in a small shift of the σ^* (C-F) resonance for sF and dF sites. This is further supported by comparisons to simple fluoromethanes. Ueda *et al.* reveal a shift of 2 eV for the σ^* (C-F) resonance between CH_2F_2 and CH_3F [114], hinting at the shift provided in my data. Through the higher complexity of PFD the fluorine XA spectrum is more convoluted than simple fluoromethanes, but the phenomenological similarity leads to a confirmation of this energetic shift and the theoretical predictions provided. Note that, the band above 691.5 eV can be uniformly assigned as σ^* (C-F) shape resonances originating principally from two transitions, where one is incorporating an additional π (F-F) contribution. Subsequently, this assignment also coincides with the fluorine XA characterisation of chain-shaped perfluorocarbons.

The high-energy excited fluorine K-edge emission spectrum (Fig. 5.15a) shows a main peak at 675 eV, with an asymmetry towards higher energies and a low-energy feature at 672 eV. This is rather well reproduced by the theoretical prediction and I also note

that the overall shape resembles the fluorine K-edge emission spectrum of CH_2F_2 [107]. In analogy, one would assign the low-energy feature with the orbitals mixed with the carbon sp^3 valence and the main peak to states that are dominated by local fluorine p character.

At low-energy excitation (see Fig. 5.15b around 687 eV) the relative intensity of the low-energy peak decreases and the main peak becomes sharper and shifts towards lower energies. To some extent I anticipate increased contributions from the sF sites at low-energy excitation, although the site-selectivity is not as clear-cut as at the carbon edge. The observed trends upon decreasing the excitation energy can, to some extent, be explained by comparing the predicted XE from sF and dF sites. A shift towards lower emission energies and a narrowing of the main feature is in line with increasing relative emphasis on sF sites. Note however, that the site selectivity predicted by the calculations is not as pronounced as at the carbon edge. In addition, we see that the main emission peak also has a low-energy shift for excitation as high as 689.7 eV, where I find it unlikely that sF sites are dominating. Therefore, I believe that the coupling with the excited electron must also be important at these energies. Such an influence of the core-hole potential is indeed supported by the calculations, delivering an excited electron that localises in the core-hole potential, resulting in the coupling with the remaining electrons delivering an excitation-energy dependence in the RIXS spectra.

Previously the meaning of the HOMO-LUMO gap to the dissolving capacity and the frontier orbital model were discussed [106]. A "shielding" effect was demonstrated, which can also be found occurring in PFD. The carbon gap can be estimated to around 6 eV, utilising the experimental and theoretical data, while the fluorine gap is approximately 12 eV. As the fluorine is encasing the carbon atoms, the active site for chemical reactions has to be either fluorine or overcome the barrier established by the encasing. In the frontier orbital model, a gap of around 12 eV is considered as chemically inert and creates insolubility of common solvents, like water and ethanol [106]. Furthermore, the favourable chemical active centre carbon is "shielded" from outside influence creating an inhibition effect, leading to further inertness. These discoveries are in-line with the observations of chain-shaped fluorocarbons and we can further assume that this "shielding" effect occurs in generally all perfluorocarbons of sufficiently low complexity.

Referencing chapter 5.2, we can also see significant spectral similarities between non-aromatic ring-shaped perfluorocarbons and chain-shaped perfluorocarbons. The phenomenological equivalency is astonishing, further supporting the claims that the constructed analytical methodology concerning XE, XA and RIXS data can be generalised onto sufficiently small hydro- and perfluorocarbons.

Summary

In summary, I presented fundamental insight into the energetic shift induced by fluorination, the so-called perfluoro effect, and a comprehensive picture of the electronic structure of decalin, as the parent hydrocarbon molecule, and perfluorodecalin based on XA, XE and RIXS spectroscopic data. In addition, DFT calculations for decalin, perfluorodecalin and stepwise fluorinated decalin derivatives were performed. We observed a change in occupancy of MOs occurring for the fluorinated hydrocarbons when reaching complete fluorination in PFD, which is in-line with the previously observed orbital change in chain perfluorocarbons. This supports the guess, that this MO alteration may be one of the main reasons for the chemical and biological inertness of perfluorocarbons compared to the corresponding partially fluorinated hydrocarbons and parent molecules. Interestingly, the orbital change assigned to the A and B_2 feature in the XA spectra could also be observed in the XE spectra for the features δ and ϵ in a complementary way. Hence, the validity of this concept and its extension to non-aromatic ring perfluoro systems was confirmed and a better understanding of the special properties of perfluoro compounds and their application development was obtained. The "shielding" effect, found for chain-type perfluorocarbons, could also be formulated for non-aromatic ring-shaped perfluorocarbons, backing the idea of fluorine inhibiting interactions through a "shield"-like mechanism. Overall, the previously established concepts were confirmed and further developed for non-aromatic ring perfluorocarbons, leading to deeper insights and a possible overall generalisation of the origin of the chemical and biological inertness of perfluorocarbons. The astonishing phenomenological spectral similarity towards chain-shaped fluorocarbons also further supports the developed assignments and methodology.

5.3.2 Cyclo-Hexane and Perfluoro-Cyclo-Hexane

The Carbon K-Edge

In the previous chapter perfluorodecalin (PFD) and its corresponding hydrocarbons were discussed, which are often studied as a general model system for ring-shaped perfluorocarbons. As such, I recreated the effects observed and introduced in chapter 5.2 for chain-shaped perfluorocarbons onto non-aromatic ring-shaped systems. Still, further observations are needed to fully generalise the proposed concepts onto all non-aromatic ring perfluorocarbons. Therefore, carbon and fluorine K-edge absorption and emission spectra of more non-aromatic liquid samples are discussed to give a full comprehensive picture.

Gas-phase inner-shell electron energy loss spectroscopy (ISEELS) experimental data on the fully-substituted, non-aromatic, single-ring structure cyclo-hexane (C_6H_{12} , cyc-hex) were obtained from data provided by Hitchcock *et. al.* [93] and depicted in Fig. 5.16a. The theoretical predictions used in the analysis of the cyc-hex data, is equivalent to the one described in chapter 3.2, but fundamentally different from the theoretical data provided by Hitchcock *et. al.* [93]. Hitchcock *et. al.* reveal a basic three-pronged structure: two peaks corresponding to σ (C-C) (287.7 eV) and π^* (CH_2) (283.1 eV), as well as a σ^* shape resonance related to σ^* (C-C) transitions (292.2 eV). My theoretical predictions reproduce the data reasonably well and the obtained feature characteristics also replicate the ones provided by Hitchcock *et. al.*.

Comparisons to the double-ring structure decalin (presented in chapter 5.3.1) reveal a striking spectral similarity, disregarding a small energetic shift of 0.5 eV and different intensity ratios. Overall, the feature assignments are identical accordingly and effects occurring for decalin and PFD can be postulated to also occur for cyc-hex and perfluoro-cyclo-hexane (C_6F_{12} , PF-cyc-hex). I note that a splitting into different carbon sites, like presented for decalin and PFD in chapter 5.3.1, is not necessary for cyc-hex, PF-cyc-hex and its respective fluorinated hydrocarbon derivatives, as every carbon is in the same environmental state.

The experimental data on PF-cyc-hex was obtained through data provided by Hitchcock *et. al.* [27]. Additionally, theoretical predictions can be found in Fig. 5.16c. The predictions show a three-pronged structure at 291.7 eV, 292.6 eV and 294.8 eV respectively, with a σ^* -shape resonance around 297 eV.

A comparison to simple fluoromethanes, as performed for PFD, is helpful in obtaining a general understanding of the predicted spectra and confirming their validity. Comparisons with CH_2F_2 should deliver a meaningful connection, as all carbon atoms in

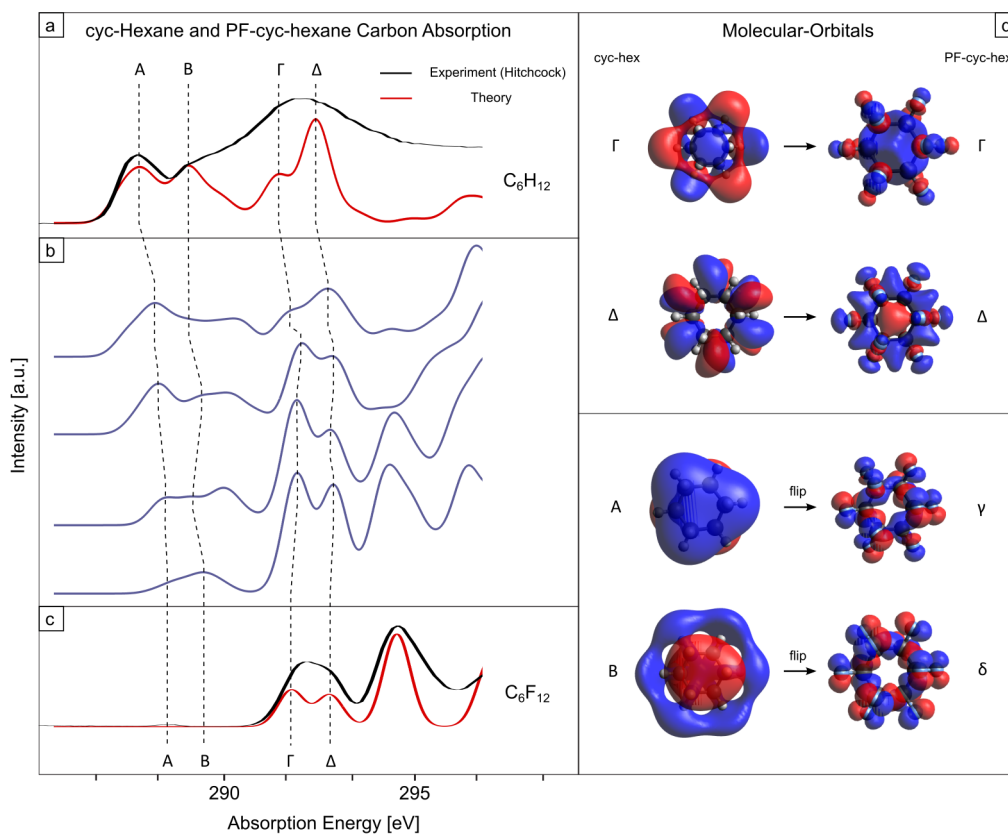


Figure 5.16: **Carbon K-edge Absorption for Cyclo-Hexane and Perfluoro-Cyclo-Hexane:** (a) and (c) show the experimental (black lines) and calculated (red lines) carbon K-edge X-ray absorption spectra for cyclohexane and perfluoro-cyclohexane. The experimental data was obtained through Hitchcock *et. al.* [27, 93]. The calculated spectra for the stepwise fluorinated derivatives are additionally depicted in (b), utilising dashed lines to indicate the shifts of the spectral features. MOs for cyclo-hexane and perfluoro-cyclo-hexane corresponding to the shifting features are labelled in (d).

PF-cyc-hex have two C-F and two C-C bonds. CH_2F_2 shows a two-pronged structure with extended Rydberg-series states at higher energies [114]. The first two features occur around 292 eV and 293 eV respectively, delivering a striking similarity to the predicted spectra (respecting an energetic shift of around 0.3 eV). The predicted resonance occurring around 295 eV can also be found in the shape off Rydberg-series states (around 295 eV [114]). Hereby, under consideration of the higher complexity of PF-cyc-hex in comparison to CH_2F_2 , I delivered a validation of the theoretical predicted spectrum.

As previously stated, and expected, the carbon K-edge spectrum of PF-cyc-hex does not show a pre-peak feature, contrary to PFD. Although geometrical similarities between PF-cyc-hex and PFD exist, both ring-shaped and non-aromatic, the single-ring structure does not reveal any carbon site-selectivity effects, like the previously mentioned pre-peak. Nonetheless, the overall spectral shape and characteristics are comparable and I can assume that bigger ring-shaped perfluorocarbons also exhibit similar spectra, taking different carbon sites and their subsequent effects on the spectrum in consideration.

After validating the spectrum for PF-cyc-hex, the predicted carbon K-edge XA spectra of stepwise fluorinated derivatives can be used to observe the perfluoro-effect (see Fig. 5.16b). The participating orbitals are additionally depicted in Fig. 5.16d and the obtained information is summarised in Table 5.5.

feature	energy shift upon complete fluorination [eV]	orbital character
<i>A</i>	0.8	not distinguishable
<i>B</i>	1.0	σ (C-C)
Γ	0.3	π
Δ	0.4	π

Table 5.5: **Perfluoro-Cyclo-Hexane XA Carbon K-edge Character Table:** Energy shifts and derived MO characters for the XA features.

Similar to the previous chapters, features *A* and *B* are of major concern, due to their disappearance in the fully fluorinated spectrum. The MO transfer effect discovered in chapter 5.2 can be reasonably assumed. To obtain more insight into these features and the occurrence of the MO transfer, an investigation of the XE spectra is necessary.

The shifts of Γ and Δ expose their π character, which can be confirmed through their MO pictures in Fig. 5.16d. As both features are in-line with the perfluoro effect principle (2-4 eV shift corresponds to σ , 0-0.5 eV shift corresponds to π) [23], further comparisons to the energetic shifts of decalin and PFD can deliver information on the scalability of

similarities of this effect in ring-shaped, non-aromatic, perfluorocarbons.

Before going into detail, I want to note that the " σ -shifting" effect can also be confirmed for PF-cyc-hex and its corresponding hydrocarbons and derivatives. The average C-C bond length for PF-cyc-hex was here calculated to be 1.551 Å and 1.520 Å for cyc-hex. In a similar fashion to PFD, the C-C bond length in partially fluorinated compounds is slightly higher for bonds including fluorine substituted carbon atoms than for only hydrogen substituted carbon atoms (around 1.549-1.551 Å *vs* 1.519-1.523 Å). Hence, the σ -shifting has only impact where fluorine substituted carbon atoms are involved. This development is in accordance to the observations of the previously reported fluorocarbons and a confirmation and further generalisation of arguments including the " σ -shifting" effect can be obtained.

I note, that all developments shown for PF-cyc-hex and cyc-hex reveal significant similarities to the XA characteristics of the previously presented fluorocarbons (see chapter 5.2 and chapter 5.3.1). Especially the similarities towards PFD and its derivatives is striking. Comparing the MOs leading to the shifts of feature Γ and Δ (see Fig. 5.11d and Fig. 5.16d, Δ_1 for PFD), we can observe that the orbitals are equivalent if I extract only part of the MO shape information in PFD. If we consider half of the MO shape in PFD (only one ring), the orbitals are schematically identical to the PF-cyc-hex orbitals. Concerning this observation, I assume that an increase in number of rings will lead to an advance in the complexity of the concerned MOs, but the MO shape of the previously less-complex (one ring less) perfluorocarbon will be observable in part. This effect can help to predict MOs and effects concerning these particular MOs of more complex ring-shaped perfluorocarbons. Nonetheless, to generalise this observation, investigations of more complex ring-shaped, as well as aromatic, fluorocarbons is recommended.

Subsequently, due to the similarities between the presented molecules and MOs, we can assume that the "shielding" effect of fluorine substituted samples, as well as the orbital change effect, occur in PF-cyc-hex and its derivatives.

Regarding the carbon K-edge XE spectra of cyc-hex and PF-cyc-hex, only theoretical predictions are provided (see Fig. 5.17). As mentioned above, detailed reasons on missing experimental data is given in chapter 5.1.

As discussed previously, comparisons with the XE spectra of CH_2F_2 (CH_4 for cyc-hex) deliver a meaningful connection and should be considered. Looking at the CH_4 XE spectrum reveals a broad feature around 277 eV [107], which is also depicted in my predictions, albeit with more complexity with two features around 275.8 eV and 277.3 eV (see Fig. 5.17a). Glans *et. al.* describe this feature as originating from sp^3 -hybridised carbon transitions, which is confirmed by my predictions if a glance at the participating MOs is taken (see Fig. 5.17d). Feature β at 279.4 eV is also outlined in the CH_4 XE

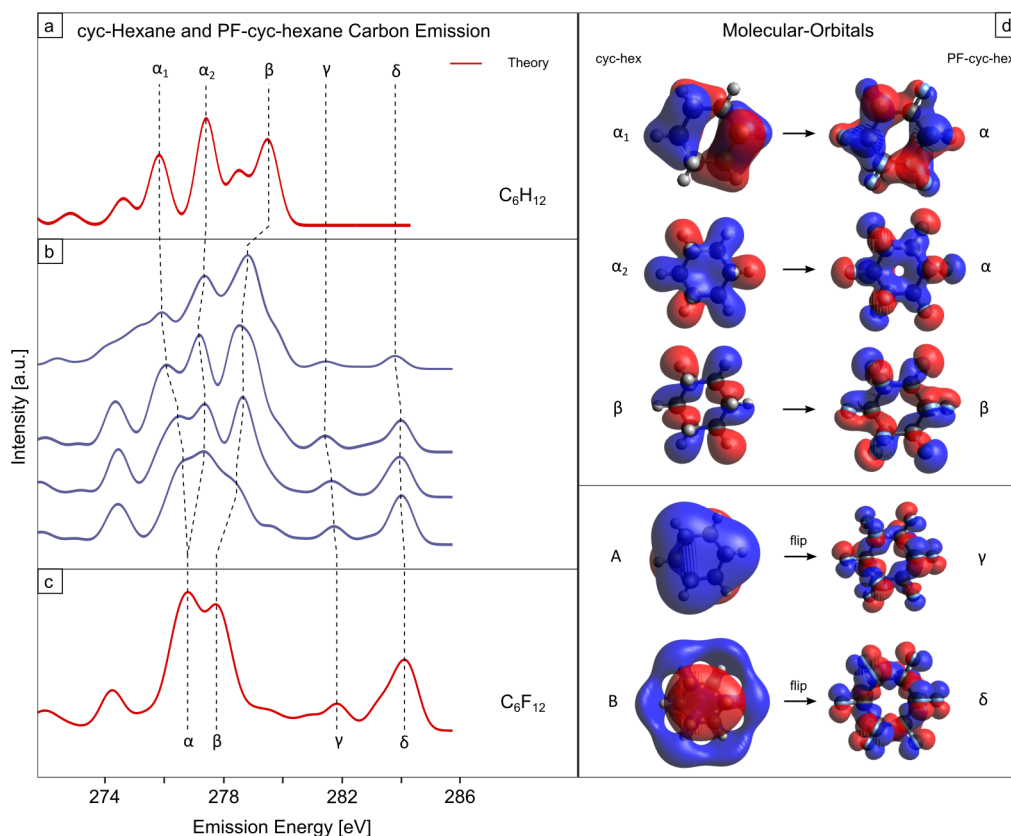


Figure 5.17: **Carbon K-edge Emission for Cyclo-Hexane and Perfluoro-Cyclo-Hexane:** (a) and (c) show the calculated (red lines) carbon K-edge X-ray emission spectra for cyclo-hexane and perfluoro-cyclo-hexane. The calculated spectra for the stepwise fluorinated derivatives are additionally depicted in (b), utilising dashed lines to indicate the shifts of the spectral features. MOs for cyclo-hexane and perfluoro-cyclo-hexane corresponding to the shifting features are labelled in (d).

spectrum [107]. This transition represents σ (C-H) type transitions for CH_4 , with an additional σ (C-C) contribution in cyc-hex, being the reason why the intensity is pronounced in cyc-hex. Overall, the assignments can be explained accordingly.

I note that, the predictions don't show significant indications for the (C-C) bond interaction features discovered in decalin (around 274.6 eV). It can be assumed, that (C-H) and sp^3 indicating type transitions are favoured due to the single-ring structure. Therefore, an experimental XE study on cyc-hex is recommended to validate this statement.

Fig. 5.17c depicts the predictions for PF-cyc-hex, delivering a four peak structure: a two-pronged feature at 276.8 eV and 277.7 eV respectively, a small feature around 281.8 eV and a high energy peak at 284.2 eV. Comparisons with CH_2F_2 show a three-peak structure [107]: a broader peak at lower energies (277 eV), typical for sp^3 -hybridised carbon,

a sharper high-energy (283 eV) peak, due to a mixed (C-F) orbital, and a peak at intermediate energies (281 eV), where the orbitals predominantly have fluorine character. If the higher complexity of PF-cyc-hex is considered, the broader peak at 277 eV can be considered to represent the two-pronged PF-cyc-hex structure, and an overall assignment is suggested accordingly due to the similarities between the two spectra.

Comparisons to the XE spectrum of PFD (see Fig. 5.12c) additionally reveals a striking similarity between the XE spectra of both perfluorinated samples. Above, it was assumed, that, the single-ring structure of cyc-hex, in comparison to decalin, is the reason for the differences between the hydrocarbon spectra. Glancing at the fluorinated samples, we observe a different behaviour. As a direct consequence I can state that, the reasons for the differences in the hydrocarbon species are suppressed in the fluorinated materials. I assume that the effect of the electronegative fluorine and its stabilising functions regarding the orbitals is the reason behind this effect. Nonetheless, to reach a full understanding of the behaviour of the above mentioned effects, an analysis of the experimental XE spectra of PF-cyc-hex and its parent hydrocarbons, with a subsequent comparison to PFD and decalin is recommended.

The stepwise fluorinated carbon K-edge XE spectra are presented in Fig. 5.17b. After combining these spectra with Fig. 5.17a and c, a visualisation of the energetic shifts is obtained. The obtained information is summarised in Table 5.6.

feature	energy shift upon complete fluorination [eV]	orbital character
α_1	1.0	π / not distinguishable
α_2	0.3	π
β	1.8	σ
γ	1.2	not distinguishable
δ	0.4	σ (C-C)

Table 5.6: **Perfluoro-Cyclo-Hexane XE Carbon K-edge Character Table:**
Energy shifts and derived MO character for the XE features.

The previously discovered disappearance of the XA features *A* and *B* already hinted at the MO transfer effect, which is confirmed through the appearance of γ and δ in the fluorinated XE spectra. A glance at the MOs (see Fig. 5.17d) validates this guess and confirms the occurrence of the MO transfer effect in single-ring, non-aromatic, perfluorocarbons. More information on the mechanics behind the MO transfer can be found in chapter 5.2.

The remaining features and shifts behave similar to the double-ring spectra, albeit with

slight differences due to the less-complex structure. The similarities towards the double-ring investigations can also be found in the large HOMO-LUMO gap. In the case of PF-cyc-hex, the gap increases by 1.8 eV, due to features *A* and *B* vanishing, additionally to the systematic energy shift for these features. Utilising the data on hydrocarbons, perfluorocarbons and the partially fluorinated hydrocarbons up to this point helps to gain insight into the mechanism reported previously. My data supports a significant increase of the gap for the last fluorination step ($C_xF_yH_1$ to C_xF_{y+1}) in all presented samples. As a result, this increases the relative inertness according to the frontier orbital model [106] in all presented chain- and ring-shaped perfluorocarbons, leading to a general trend.

This reveals the generality of the orbital change and HOMO-LUMO gap increase concepts established in chapter 5.2, leading to the critical impact on the inertness of the perfluorinated molecule in accordance to the frontier orbital model [106]. This confirms my guess that sufficiently simple fluorinated hydrocarbons can be investigated by the, hitherto presented procedures.

The Fluorine K-edge

In the previous section, the similarities between the carbon data of the presented single-ring and double-ring samples was pointed out. As a direct conclusion a corresponding development in the fluorine K-edge observations and a confirmation of the "shielding"-effect discovered in chapter 5.2 can be expected.

In the same fashion as the carbon K-edge, experimental data obtained by Hitchcock *et. al.* on the fluorine edge is presented [27]. The fluorine K-edge XA spectrum (see Fig. 5.18a) reveals four main features: a first two-pronged structure at 687.6 eV and 688.2 eV with a pronounced peak at 689.8 eV followed by a broad feature around 693 eV. A glance at the participating MOs (see Fig. 5.18a) reveals the involvement of σ^* (C-F) transitions for the two-pronged structure and π^* (C-F) transition in the case of the 690 eV feature. In a direct comparison to PFD (see chapter 5.3.1), the spectrum is equivalent in character and energetic positioning. The main difference is the two-pronged structure of the first-feature, which can be attributed to the less-complex geometrical structure. Further support can be found in the experimental spectrum of CH_2F_2 [114], as it shows a strong phenomenological similarity to the PFD and PF-cyc-hex spectra.

The fluorine K-edge XE spectrum (see Fig 5.18b) shows a main peak at 676 eV and a low-energy feature around 672 eV. A small high-energy shoulder around 679 eV can also be identified. This is rather well reproduced by the emission spectrum of CH_2F_2 [107], considering an energetic shift of 1.8 eV towards higher energies. Accordingly, one would assign the low-energy feature with orbitals mixed with the carbon sp^3 valence, the main peak to states that are dominated by local fluorine p character and the high-energy shoulder towards a mixed (C-F) orbital.

As the fluorine is encasing the carbon atoms, as seen in the corresponding orbitals (see Fig. 5.18a), the active site for chemical reactions has to be either fluorine or overcome the barrier established by the encasing. The predicted energetic HOMO-LUMO gap amounts to 8 eV for the fluorine site and around 4 eV for the carbon site. Subsequently, the favourable chemical active centre carbon is "shielded" from outside influence creating an inhibition effect, leading to chemical inertness. These discoveries are in-line with the observations of the "shielding" effect and we can establish a general rule stating that in all perfluorocarbons of sufficiently low complexity the "shielding" effect occurs.

Referencing the previous chapters 5.2 and 5.3.1, we can also see significant spectral similarities between non-aromatic ring-shaped perfluorocarbons and chain-shaped perfluorocarbons, establishing an astonishing phenomenological equivalency.

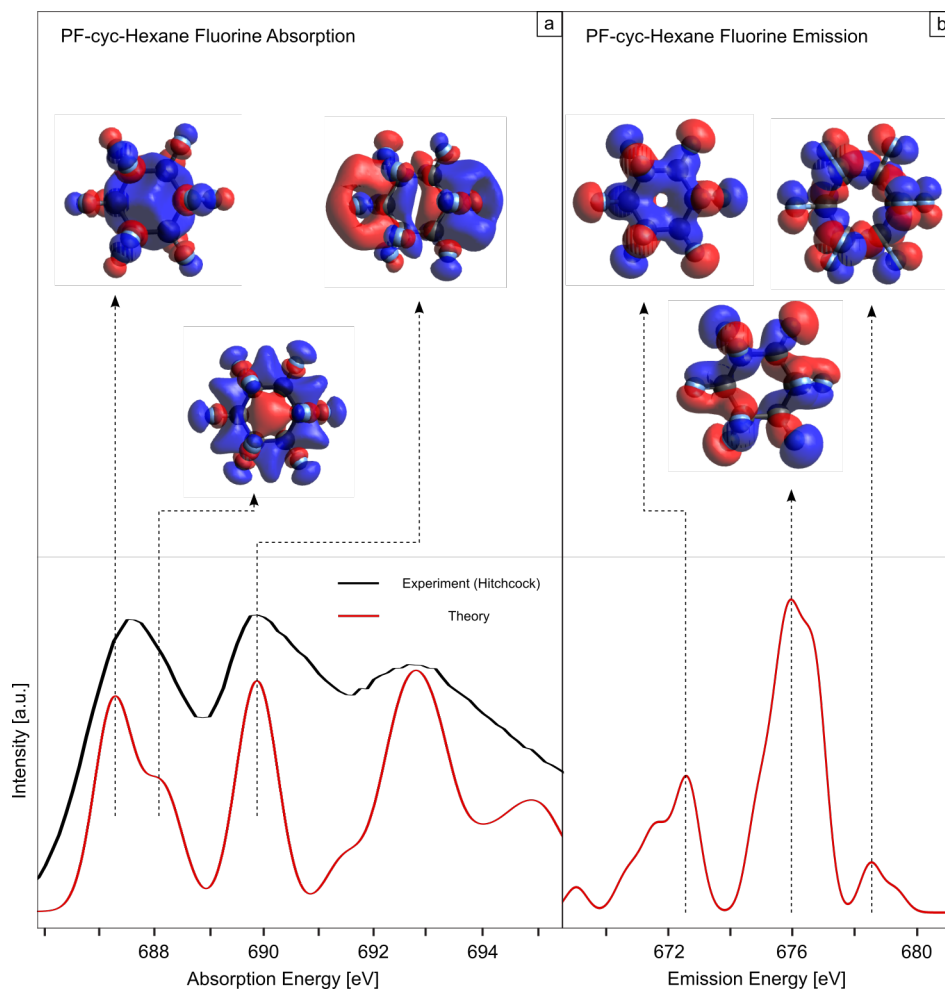


Figure 5.18: **Fluorine K-edge Data for Perfluoro-Cyclo-Hexane:** Theoretical and Experimental fluorine K-edge X-ray absorption data for perfluoro-cyclo-hexane (a) and their respective X-ray emission data (b). The experimental data was obtained through Hitchcock *et. al.* [27]. The upper area illustrates the molecular orbitals for the corresponding transitions.

Summary

I presented fundamental insight into the energetic shift induced by fluorination and a comprehensive picture of cyclo-hexane, perfluoro-cyclo-hexane and the corresponding stepwise fluorinated hydrocarbons based on XA and XE data. The addition of TD-DFT calculations gave rise towards the discovery of the MO transfer in these molecules, which is in-line with the previously observed orbital change in chain perfluorocarbons and the double-ring structure perfluorodecalin. The guess that, this MO alteration may be one of the main reasons for the chemical and biological inertness of perfluorocarbons compared to the corresponding partially fluorinated hydrocarbons and parent molecules, is therefore supported and underlined. Additionally, the validity of this concept was supported and its extension to different non-aromatic ring perfluoro systems confirmed. The idea of fluorine inhibiting interactions through a "shield"-like mechanism was also confirmed and can therefore be extended onto different non-aromatic ring-shaped perfluorocarbons. An astonishing spectral similarity towards the double-ring structure PFD was found and I proposed an MO prediction method for more complex ring-shaped fluorinated structures. Furthermore, the spectral similarity with PFD directly leads to phenomenological similarities towards chain-type perfluorocarbons. Note that, the orbital stabilising effect of fluorine was also directly observed and discussed. Overall, the extension of the previously established concepts onto more non-aromatic ring perfluorocarbons was confirmed, hinting at a generalisation of the origin of the chemical and biological inertness of perfluorocarbons.

5.4 Aromatic Ring-Shaped Hydro- and Perfluorocarbons

5.4.1 Benzene and Perfluorobenzene

The Carbon K-Edge

Until this point all presented materials were of non-aromatic character. These kinds of molecules show less delocalisation effects, a lower HOMO-LUMO gap as well as lower chemical reactivity in comparison to the aromatic counterparts [115]. An epitome of such a material is the hydrocarbon benzene. It is a ring-shaped molecule of low complexity with a free π -electron system and the subsequent heavily delocalized MOs. As the primary example, research on benzene and its fluorinated derivatives was prominent and well performed through different experimental means [25, 22, 90].

In this work I will focus on comparing the experimental results, as well as the state-of-the-art theoretical predictions, obtained on benzene and its fluorinated derivatives with existing observations and try to extend my previously reported methodology and results from the non-aromatic onto aromatic systems.

After the perfluoro effect was established by Brundle *et. al.* on non-aromatic molecules [23], they tried to extend it onto aromatic systems [22]. Problems occurred, as the free π -electron system lead to strong destabilisation of the MOs of the partially fluorinated hydrocarbons, leading to difficulties in the assignments with the fully theoretical method used in the previous chapters. Accordingly, Brundle *et. al.* utilised atomic population analyses and MO comparison methods to obtain the shifts [22].

I encountered similar problems, leading to an inability of utilising the theoretically obtained shifts of the subsequent partially fluorinated hydrocarbons. As a result, I adjust my method for aromatic molecules to the one suggested by Brundle *et. al.*

The experimental benzene carbon K-edge absorption, as well as its theoretical predictions, is depicted in Fig. 5.19a. A four-fold structure is visible with a broad band extending from 292 eV until around 295.4 eV. The first resonance occurs around 285.2 eV and is a typical π -type transition for aromatic materials. At higher energies a three-pronged structure with peaks at 287.55 eV, 289.1 eV and 290.5 eV are observed. As mentioned previously, benzene is one of the most studied materials and therefore, XA studies are available for comparisons. Plashkevych *et. al.* delivered an extensive study on benzene and its fluorinated derivatives in gas phase [90], giving an opportunity for comparison. Overall, my energetic positions and the ones presented by Plashkevych *et.*

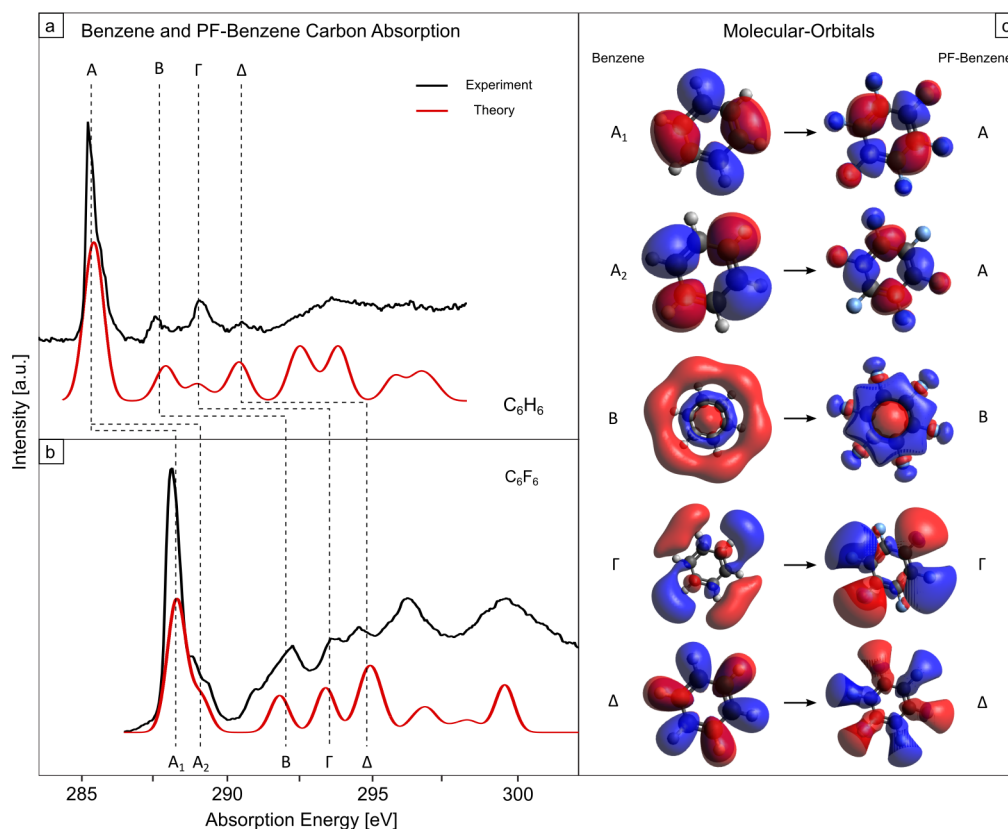


Figure 5.19: **Carbon K-edge Absorption for Benzene and Perfluorobenzene:** (a) and (b) show the experimental (black lines) and calculated (red lines) carbon K-edge X-ray absorption spectra for benzene and perfluorobenzene. Dashed lines are utilised to indicate the shifts of the spectral features. MOs for benzene and perfluorobenzene corresponding to the shifting features are labelled in (c).

al. are equal with respect to small shifts in the meV-range. As expected, the intensity ratios differ, which is a direct outcome from the different phases of matter in both investigations. Note that, feature Δ is not visible in the provided literature, but in my spectra. This, again, is an outcome due to the difference in phase, as the ionisation potential is shifted to higher energies in the correlated liquid state, compared to the one determined by Plashkevych *et. al.* (290.3 eV).

A glance at the MOs provided in Fig. 5.19c provides us with information about the orbital character of each transition, which can also be compared to literature [90]. Overall, the assignments, as provided by Table 5.7, are equivalent to literature. The only exception is transition A, which consists of two transitions originating from two similar MOs both exhibiting a π^* (C-H) orbital character. The difference can be explained through the way the assignments were obtained in literature. Plashkevych *et. al.* utilised the

perfluoro effect and previous assignments to determine the characters [90], while in this work MOs based on theoretical predictions of the XA spectra are additionally used. Through the theoretical predictions I was able to determine the two-fold character of peak *A*, which was not possible for Plashkevych *et. al.*

In Fig. 5.19b a five-fold spectral structure with a broad band extending from 298.2 eV until around 301.6 eV can be seen for perfluorobenzene. The features occur at the appropriate energetic positions: 288.1 eV (A_1), 289 eV (A_2), 292.4 eV (B), 293.6 eV (Γ), 294.6 eV (Δ) and 296.2 eV (unassigned). Comparisons to literature provide an according assignment again, albeit taking shifts in the meV-range into account [90] (see Table 5.7). A glance at the MOs (see Fig. 5.19c) suggests assignments accordingly. Notable is the structure of the first π^* feature with an attached shoulder, also of π^* character. Taking the overall similarities to the gas-phase spectra of Plashkevych *et. al.* into account [90], I conclude a behaviour as predicted by literature, but additionally confirmed by the MO pictures. Before going into more detail, the perfluoro effect should be investigated as it extends and further confirms the findings of Plashkevych *et. al.*

The shifts were obtained as described previously and summarised in Table 5.7. It was mentioned that the perfluoro effect works slightly different for aromatic molecules and Brundle *et. al.* explained that the general rules (2-4 eV corresponds to σ , 0-0.5 eV corresponds to π) are still valid, albeit π shifts are generally larger and often distorted [22]. As a direct result, π shifts are in the same range as σ shifts inhibiting observations of the perfluoro effect on most aromatic molecules.

feature	energy shift upon complete fluorination [eV]	orbital character
A_1	2.9	π^* (C-H)
A_2	3.8	π^* (C-H)
B	4.7	σ^* (C-H)
Γ	4.5	σ^* (C-C) / π^* (C-H)
Δ	4.1	σ (C-H)

Table 5.7: **Perfluorobenzene XA Carbon K-edge Character Table:** Energy shifts and derived MO characters for the XA features.

As can be observed, the shifts of all features are overemphasised. Still, a clear trend towards shifts bigger than 4 eV can be seen for σ -type transitions, with π -type ones ranging between 3 to 4 eV. Additionally, Plashkevych *et. al.* confirm the shifts included in Table 5.7 [90]. The photoelectron analysis on perfluorobenzene and its parent-hydrocarbon by Brundle *et. al.* show, in contrast to my and Plashkevych findings, that the perfluoro

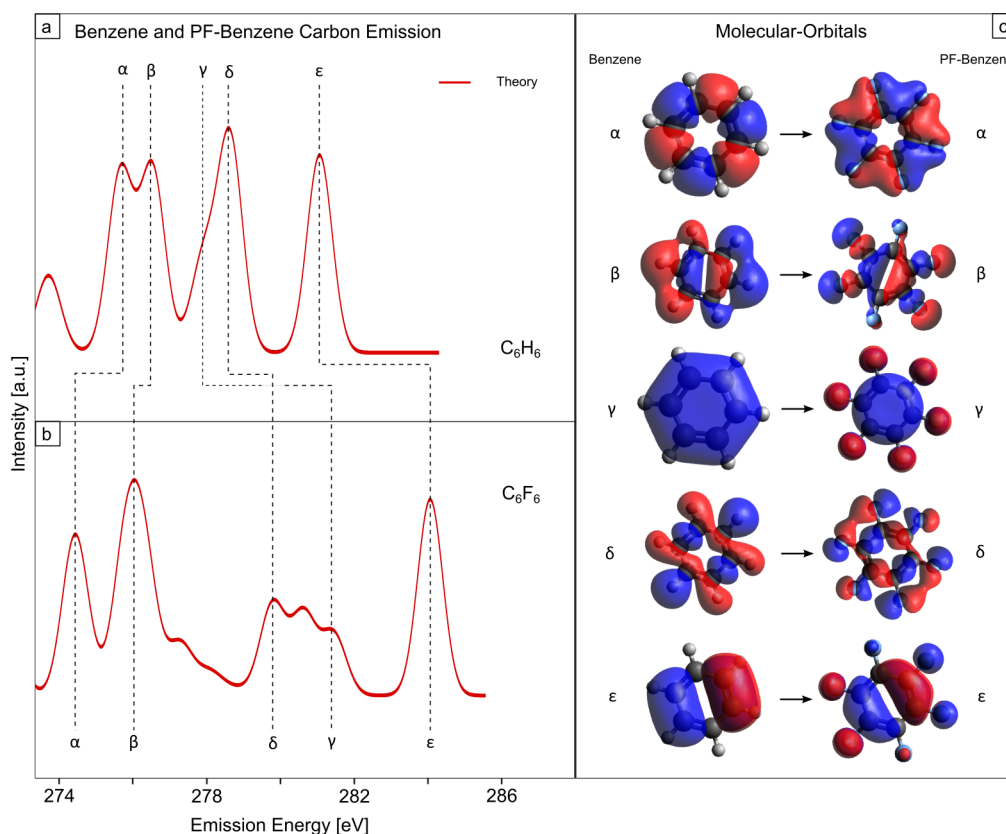


Figure 5.20: **Carbon K-edge Emission for Benzene and Perfluorobenzene:** (a) and (b) show the calculated (red lines) carbon K-edge X-ray emission spectra for benzene and perfluorobenzene. Dashed lines are utilised to indicate the shifts of the spectral features. MOs for benzene and perfluorobenzene corresponding to the shifting features are labelled in (c).

effect rules are still valid on aromatic molecules [22].

We can explain the differences through the different methods of observation used by us and Brundle (more information in chapter 3.1). In the case of photoelectron spectroscopy, the molecule is ionised in the process to obtain the spectral positions, while for XAS the electrons are promoted into empty MOs. The subsequent correlation between the MOs involved in the XA excitation process lead to a smeared out perfluoro effect for aromatic molecules, as the fluorine stabilisation effect is naturally suppressed and the higher delocalisation of the MO creates chances of overlap processes occurring. This idea is also hinted at by Plashkevych *et. al.* and further confirmed in this work [90].

The theoretically predicted benzene and perfluorobenzene XE spectra are presented in Fig. 5.20a and b respectively. In both cases a five-fold structure is visible and a glance at the MOs reveals the orbital character of each feature (see Fig. 5.20c). The energetic positions of all features are also summarised in Table 5.8. The predicted energy positions

and MO characters of the benzene features are overall in-line with literature, albeit a shift of 0.4 eV needs to be considered [92].

feature	energetic position benzene [eV]	energetic position PFbenzene [eV]	energy shift upon complete fluorination [eV]	orbital character
α	275.7	274.4	-1.3	σ (C-C) / π (C-H)
β	276.5	276.1	-0.4	π
γ	277.9	281.4	+3.5	π (C-C) / σ^* (C-H)
δ	278.3	279.8	+1.5	σ (C-C) / σ (C-H)
ε	281.1	284.1	+3.0	π^* (C-C) / σ^* (C-H)

Table 5.8: **Perfluorobenzene XE Carbon K-edge Character Table:** Energetic shifts, positions and derived MO characters for the XE features.

The obtained energetic shifts are surprisingly in-line with the perfluoro effect rules, which stands in stark contrast to the XA observations. Special attention needs to be provided towards features γ and ε , as they are also not in-line with the rules. Still, this can be explained with the intrinsic differences between occupied and unoccupied orbitals, like the electronic nodal planes and electron distribution. One should pay special attention to the differences in electron distribution. In case of occupied MOs, a more localised orbital is expected in comparison to unoccupied ones. As can be observed in Fig. 5.20c, the orbitals are more localised compared to Fig. 5.19c, underlining this argument. This results in a stronger fluorine stabilisation effect and lower chances of overlap processes occurring, directly leading to a less smeared out perfluoro effect. Nonetheless, the mentioned features γ and ε are special, in the sense that the fluorine strongly quenches, or "encases", the hydrocarbon MO upon fluorination instead of stabilising it (see Fig. 5.20c). This strong quenching still leads to a blurred out perfluoro effect in aromatic perfluorocarbons.

As a result I can declare, that the perfluoro effect of aromatic perfluorocarbons is strongly smeared out in case of XA spectroscopy leading to difficulties in utilising the subsequent investigative processes. On the other hand, due to the intrinsic differences between occupied and unoccupied orbitals, investigations of the perfluoro effect using the XE spectroscopy method are possible. Special attention needs to be provided to

orbitals that are "encased" upon fluorination, as the perfluoro effect will be smeared out.

Additionally, Plashkevych *et. al.* discussed the idea of utilising benzene and its fluorinated derivatives as fingerprint building blocks for polymeric compounds [90]. To successfully execute such fingerprint investigations the spectra of the sub-units of the polymer have to be little perturbed by the specific polymeric environment. They discovered that, only the HOMO transitions can be utilised for this, as they are energetically constant in different gas environments. I'd like to extend this onto the LUMO transitions and possibly liquid environments. From the limited experimental and complementary theoretical analysis I can confirm that, the LUMO transitions are energetically stable between gas and liquid environment. I suspect that, these transitions are the least affected by environmental changes leading to the possibility of utilising these transitions in fingerprint investigations. To generalise this argument, further investigation onto different environments and a full experimental study are required. Nonetheless, I can confirm that the HOMO transitions are energetically unaffected by the change from gas to liquid environment, supporting the findings by Plashkevych *et. al.* [90].

Note that, the investigations of the non-aromatic samples in previous chapters can also extend this discussion. A glance at the hydrocarbon and fully fluorinated derivative delivers in all cases a clear first feature associated with the HOMO and LUMO orbitals. The differences between the partly fluorinated derivatives are smaller in comparison to the reported data by Plashkevych *et. al.* [90], leading to problems in differentiating them and their use as fingerprint spectra. Nonetheless, the non-aromatic hydro- and perfluorocarbon spectra are useable as a fingerprint due to their clear distinctive features, leading to a possible extension of the discussion initiated by Plashkevych *et. al.*. Ultimately, as the *vide supra* reported non-aromatic samples rarely occur in polymeric compounds one has to test the overall utility of these findings.

The Fluorine K-Edge

In previous chapters concerning the fluorine K-edge, the possible effects of a so called "shielding" effect and the HOMO-LUMO gap differences were established and discussed. As shown in the benzene carbon data, significant differences between aromatic and non-aromatic hydro- and perfluorocarbons were discovered, which can also affect the fluorine K-edge and corresponding effects.

A four-fold structure can be seen in the fluorine K-edge XA spectrum of perfluorobenzene, while on the other hand the theoretical calculations predict a more feature rich spectrum (see Fig. 5.21a). The first, most prominent, resonance occurs around 688.7 eV and can be associated with σ^* (C-F) transitions. Reaching higher excitation energies, a broader band with two significant features can be observed. The first feature lies at 693.1 eV and can respectively be associated with π^* (C-F) transitions, with the second peak being π (C-F) type transitions around 696.8 eV. A small protrusion, slightly above the ionisation threshold, can be identified at 699.8 eV originating from a σ - π hybrid orbital. As already mentioned, the theoretical predictions deliver a more feature rich spectrum with three additional peaks. As no experimental indication for these can be found, a deeper investigation will be omitted until a spectrum with higher resolution is obtained and the existence of these peaks are confirmed. Nonetheless, the fluorine K-edge absorption spectrum of perfluorobenzene shows similarities towards the spectra of fluoroalkanes (see chapter 5.2) and non-aromatic, ring-shaped, perfluorocarbons (see chapter 5.3.1).

The similarities occur due to the similar environment of the fluorine atoms in different perfluorocarbons. In chapter 5.3.1 I already discussed the effect of fluorine being attached to different carbon sites in the same molecule and discovered that the differences are miniscule, as the nearest neighbour is always carbon and only the next nearest neighbour may differ. Such a long range effect could not be discovered and that can be utilised in explaining why the perfluorobenzene spectrum is similar to other perfluorocarbons. In all presented samples the nearest neighbour is a carbon atom, which creates a structural similarity. Minor differences between the spectra, like intensity differences or energetic positions, can therefore be attributed to the differences in carbon sites.

Especially the difference between aromatic and non-aromatic carbon sites is significant. Consequently, the fluorine spectrum of perfluorobenzene has sharper features and a more profound main resonance, in comparison to perfluoro-cyclo-hexane or perfluorodecalin. I can conclude, that the carbon π electron system affects the transitions of fluorine favourably, as the sharper features hint at greater MO overlap and transition intensity.

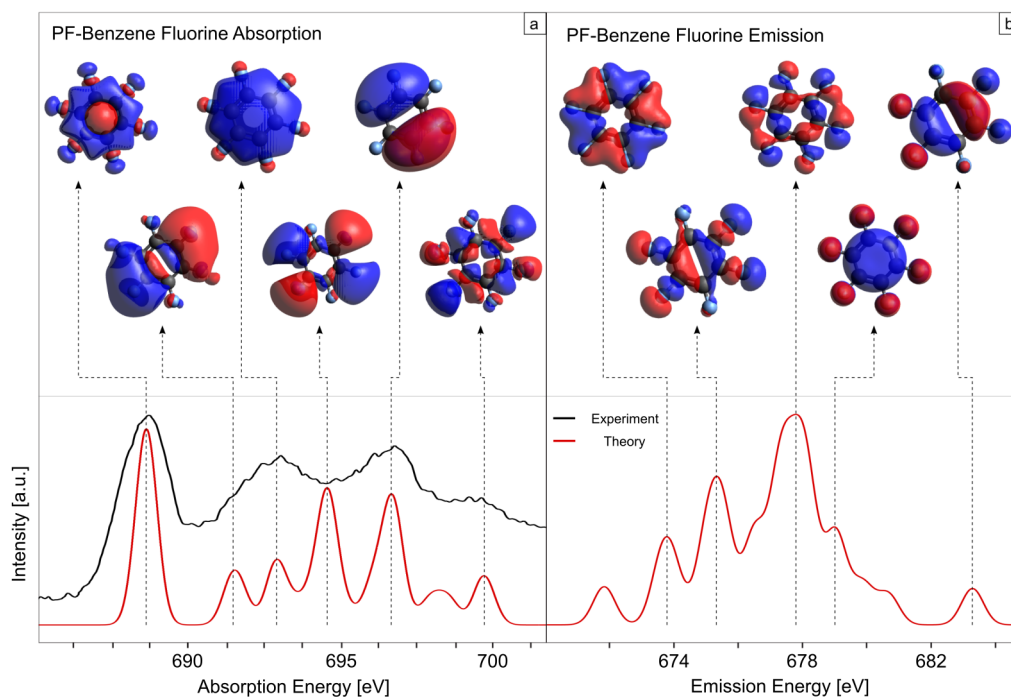


Figure 5.21: **Fluorine K-edge Data for Perfluorobenzene:** Theoretical fluorine K-edge X-ray absorption data for perfluorobenzene (a) and their respective X-ray emission data (b). The upper area illustrates the molecular orbitals for the corresponding transitions.

A glance at the theoretically predicted fluorine XE spectrum, reveals a significant difference towards the spectra of non-aromatic perfluorocarbons. In PFD for example (see chapter 5.3.1), a two-pronged structure was observed experimentally with a corresponding theoretical spectrum. Here, the theoretical spectrum does not offer a clear two-pronged structure, but, under consideration of an experimental broadening, it can be assumed that a broad peak feature spanning from around 673 eV to 680 eV will be seen in the experimental observations. The main reason for this is the feature occurring at 675.4 eV, which is shifted towards lower energies in non-aromatic samples. We also have to consider that the small feature at 683.4 eV will not be visible experimentally, if comparisons to the experimental PFD spectrum are drawn. Overall, an accurate determination of the experimental fluorine K-edge emission spectrum is recommended to confirm the differences hinted at in the theoretical predictions.

As a direct outcome of the hinted differences, the "shielding" effect is modified. I want to note that, in case of perfluorobenzene, the "shielding" effect is unlikely to occur, due to the geometrically free space for accessing the chemically active carbon atoms. Additionally, the encasing effect can not be seen in the MOs, undermining the basis for

the "shielding" in perfluorobenzene.

Still, a glance at the HOMO-LUMO gap confirms the differences between fluorine gap (≈ 8 eV) and carbon gap (≈ 4 eV) discovered in previous chapters. I can therefore conclude that, the carbon atoms are more chemically and biologically active than the fluorine atoms.

To summarise, the reason for the "shielding" effect to be diminished in perfluorobenzene is the geometrical positioning of the fluorine atoms. Nonetheless, the HOMO-LUMO gap differences could still be confirmed, essentially marking the carbon as the chemically active centres. Additionally, due to the big π electron clouds of the MOs, I conclude a significant amount of π -stacking to occur in perfluorobenzene.

Summary

I tried to extend the methodological and analytical processes found for non-aromatic perfluorocarbons in previous chapters onto aromatic samples. To achieve this, I presented fundamental insight into the energetic shift induced by fluorination and a comprehensive picture of benzene and perfluorobenzene based on XA and XE data. As concluded by Brundle *et. al.*, the free π -electron system leads to strong destabilisations of the MOs of the partially fluorinated hydrocarbons, leading to difficulties in the assignments with the fully theoretical method used in the previous chapters [22]. As a result, I obtained the information through utilising atomic population analyses and MO comparison methods to obtain the shifts. An overemphasis of the energetic shifts described by the perfluoro effect was found and discussed in detail, taking several experimental methods and literature into account.

The MO transfer, first observed in chapter 5.2, could not be confirmed for benzene and its fluorinated counterpart. The stabilisation effect upon fluorination is suppressed by the free π electron system of aromatic molecules, as already described by Brundle *et. al.* [22], leading to the dissolution of the transfer effect. The previously discovered "shielding" effect did not occur, leading to a more chemical active compound. Consequently, the validity of these concepts for aromatic systems could not be confirmed and their extension to aromatic ring perfluoro systems could not be achieved.

Finally, the proposed idea by Plashkevych *et. al.*, to use fluorinated benzene as a fingerprint building block in polymeric compounds could be confirmed [90]. Additionally, a possible extension to non-aromatic perfluorocarbons was hinted at.

5.4.2 Naphthalene and Perfluoronaphthalene

The Carbon K-edge

The principle example for aromatic ring-shaped hydrocarbons, benzene, and its fluorinated derivative revealed significant differences towards the previously reported non-aromatic samples. The MO transfer effect observed for the non-aromatic materials could not be reproduced and it can be assumed that the reason for this is the free π electron system of aromatic class molecules. Nonetheless, benzene and perfluorobenzene are rather simple aromatic molecules and an investigation of more complex fluorinated hydrocarbons could prove to be beneficial.

In a similar manner to cyclo-hexane and decalin, this chapter will focus on the extension of the single-ring observations from benzene onto the double-ring structure naphthalene (naph). Naphthalene is a double-ring compound ($C_{10}H_8$) with an aromatic system spanning over both rings. Under room temperature and normal lab conditions it's a solid with surprisingly low flash point. Overall, the perfluorinated naphthalene (PFnaph) exhibits the previously mentioned characteristics of perfluorocarbons and under liquid conditions (after heating) gas storing capabilities can be observed [19, 94].

To investigate the effects reported for benzene and extend my analysis, I underline the experimental observations of Hitchcock *et. al.* [25] with my theoretical predictions. Therefore, comparisons between my analysis and literature will lead to a more in-depth picture of the local electronic structure of naph and PFnaph, as well as proof the role of aromatic fluorinated hydrocarbons in the frame of this work.

Hitchcock *et. al.* observed a six-fold experimental structure as depicted in Fig. 5.22a [25]. The energetic positions of these features, as reported in literature, are summarised in Table 5.9. The theoretical predictions can also be found in Fig. 5.22a and reproduce the experimental spectrum well. As already performed for decalin, a distinction between the carbon sites of naph was made (see chapter 5.3.1). For naph the according assignments would be: sC for the two carbon atoms with no hydrogen attached as nearest neighbour and dC for the remaining eight carbon atoms with one hydrogen as nearest neighbour.

Overall, the orbital character assignments provided by Hitchcock *et. al.* [25] are reproduced by the theoretical predictions and MO pictures (see Fig. 5.22c and table 5.9), albeit additional information on the different carbon sites was obtained. At a glance we can observe that the whole spectrum is dominated by dC carbon transitions, with three out of the six main features being solely dC contributions (A , Γ and Δ) and the remaining ones being mixed. Note however, two of the mixed contribution transitions (B and E) show a significantly higher sC than dC contribution. Special attention needs

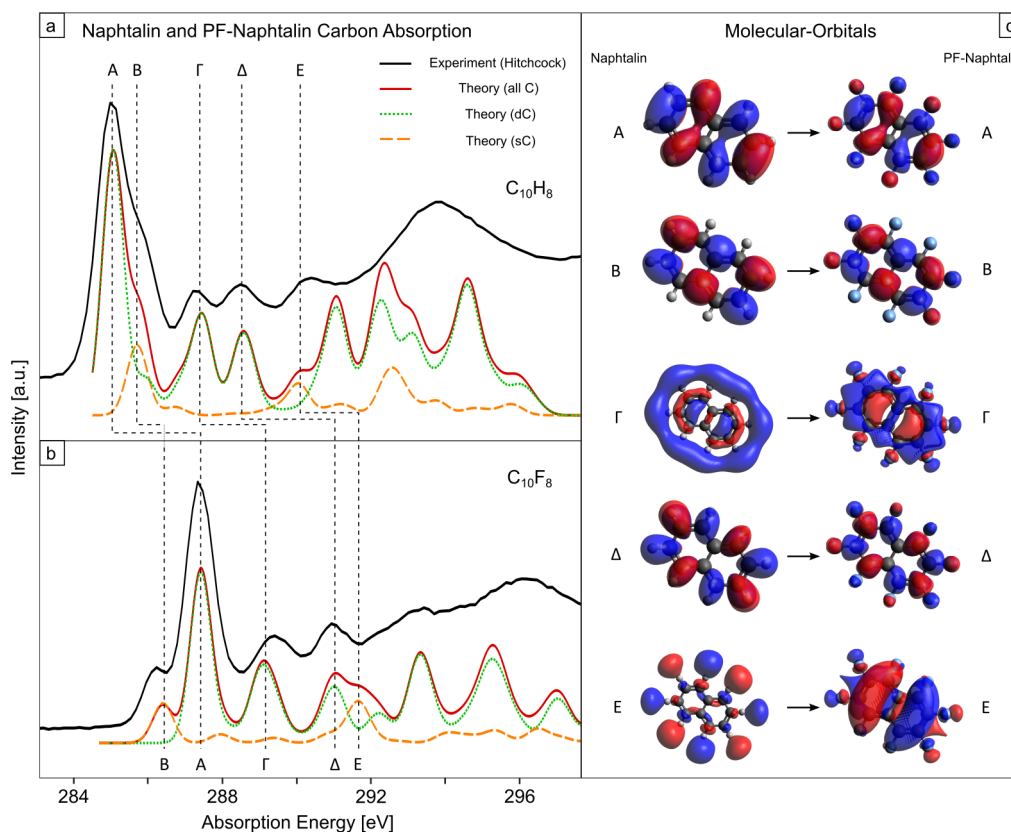


Figure 5.22: **Carbon K-edge Absorption for Naphthalene and Perfluoronaphthalene:** (a) and (b) show the experimental (black lines) and calculated (red lines) carbon K-edge X-ray absorption spectra for naphthalene and perfluoronaphthalene. The experimental data was obtained through Hitchcock *et. al.* [25]. Dashed lines are utilised to indicate the shifts of the spectral features. MOs for naphthalene and perfluoronaphthalene corresponding to the shifting features are labelled in (c).

to be given to feature *B*, as the dC contribution vanishes upon fluorination to PFnaph, which will be investigated in more detail later on.

The five-fold structure of PFNaph is significantly well reproduced by my theoretical predictions, as seen in Fig. 5.22b. The energetic positions, as well as the orbital character assignments, of the according features are summarised in Table 5.9. Similar to naph, the theoretical predictions and MO pictures (see Fig. 5.22c) reproduce the orbital character assignments provided by Hitchcock *et. al.* [25]. Thus, the whole PFNaph spectrum is dominated by dC carbon transitions, with the exception of two features. Comparable to naph, *E* is of mixed contribution, while the second special feature *B* is of sole sC contribution. Note that, *E* is of mixed π^* (C-C) and σ^* (C-H) character, while *B* is of sole π^* orbital character.

feature	energetic position naphthalene [eV]	energetic position PF- naphthalene [eV]	energy shift upon complete fluorination [eV]	orbital character
<i>A</i>	285	287.4	2.4	π^*
<i>B</i>	285.9	286.2	0.3	π^*
Γ	287.3	289.4	2.1	π^* (C-C) / σ^* (C-H)
Δ	288.5	290.9	2.4	π^* (C-C) / σ^* (C-H)
<i>E</i>	290.2	291.6	1.4	π^* (C-C) / σ^* (C-H)

Table 5.9: **Perfluoronaphthalene XA Carbon K-edge Character Table:** Energetic shifts, positions and derived MO characters for the XA features. Energetic positions are as reported by Hitchcock *et. al.* [25].

Utilising the energetic shifts obtained upon fluorination, also called the perfluoro effect, most of the MO character assignments by Hitchcock *et. al.* [25], as well as the here presented classifications through the MO picture, are confirmed (see table 5.9). To obtain the energetic shifts for the perfluoro effect, I utilised the method previously reported for benzene and PFbenzene (see chapter 5.4.1). Considering the observation made in chapter 5.4.1 for benzene, that π shifts are in the same range as σ shifts inhibiting observations of the perfluoro effect, a clearer picture can be drawn. In case of naph, two absorption features behave according to the perfluoro effect rules, which stands in contrast to the benzene observations. *B* and *E* both behave as stated by Brundle *et. al.* [22, 23], with *B* being a clear π feature and *E* a π - σ hybrid. Surprisingly, both of these features are the previously described sC contribution features.

In case of benzene and PFbenzene all carbon atoms are connected to a fluorine upon fluorination, which is different for naph and PFnaph. The difference between dC and sC carbon atoms becomes evident by calculating the partial charge distributions. The difference in distribution changes stronger for dC atoms (from -0.18 to 0.58) compared to the sC ones (from -0.06 to 0.18). As a result, we see that the dC atoms are affected stronger by the fluorination than the sC carbons, which was expected. Therefore, the dC carbons are also affected stronger by changes in the aromatic π electron system, which lead to the distortions in the perfluoro effect rules of benzene (see chapter 5.4.1). Under such circumstances I can conclude that, the perfluoro effect rules still hold true for XAS observations of aromatic perfluorocarbons, if the carbon atoms are less affected

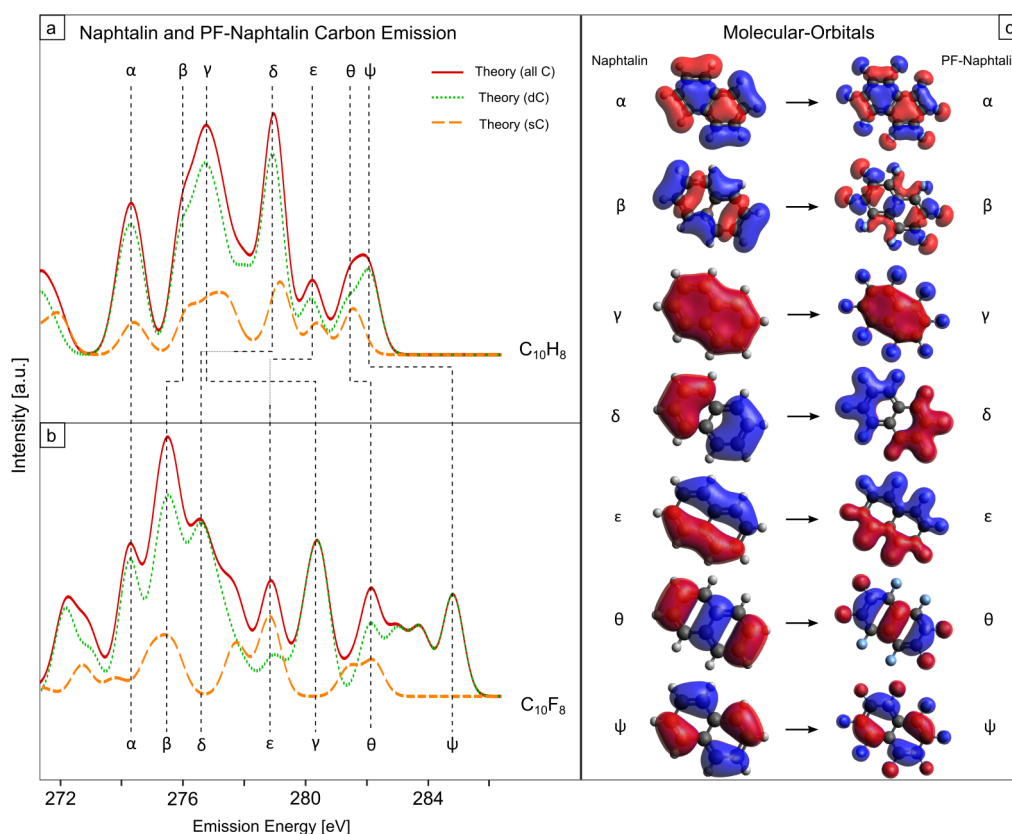


Figure 5.23: **Carbon K-edge Emission for Naphthalene and Perfluoronaphthalene:** (a) and (b) show the calculated (red lines) carbon K-edge X-ray emission spectra for naphthalene and perfluoronaphthalene. Dashed lines are utilised to indicate the shifts of the spectral features. MOs for naphthalene and perfluoronaphthalene corresponding to the shifting features are labelled in (c).

by changes in the aromatic π electron system. Investigations of more complex aromatic perfluorinated systems, with the help of theoretical predictions in similar manner to those presented here, are therefore recommended to validate this statement.

The theoretical predictions for the XE spectra of naph and PFnaph are shown in Fig. 5.23a and b respectively, with the addition of carbon dC/sC site information. Both spectra show strong similarities towards benzene and PFbenzene XE spectra predictions, albeit a higher complexity for naph and PFnaph is observed due to the double-ring structure. The information on energetic positions, as well as shifts, are summarised in table 5.10.

feature	energetic position naphthalene [eV]	energetic position PF-naphthalene [eV]	energy shift upon complete fluorination [eV]	orbital character
α	274.3	274.4	+0.1	π (C-C) / σ^* (C-H)
β	276	275.7	-0.3	π (C-C) / σ^* (C-H)
γ	276.7	280.5	+3.8	π (C-C) / σ^* (C-H)
δ	278.9	276.7	-2.2	π^* (x-axis)
ε	280.2	279	-1.2	π^* (z-axis)
θ	281.4	282.3	+0.9	π^*
ψ	282	284.9	+2.9	π^* (C-C) / σ^* (C-H)

Table 5.10: **Perfluoronaphthalene XE Carbon K-edge Character Table:** Energetic shifts, positions and derived MO characters for the XE features.

The similarity towards benzene is resumed by observing the perfluoro effect, as the energetic shifts are in-line with the rules, in contrast to the XA features. Previously, the intrinsic differences between occupied and unoccupied orbitals were discussed and found to be responsible for this difference between XE and XA spectra (see chapter 5.4.1), which is also the case for naph and PFnaph.

Even though most features were in-line with the rules, exceptions were found and discussed with regard to quenching, or "encasing", the hydrocarbon MO upon fluorination. These exceptions can also be found for naph and PFnaph, as features γ , δ , ε and ψ have shifts unexpectedly high for their orbital character. A glance at the MOs concerning these particular transitions (see Fig. 5.23c) reveals strong quenching ("encasing") effects due to the fluorination. As previously discussed, this strong quenching leads to a smeared out perfluoro effect in aromatic perfluorocarbons, resulting in unexpected energetic shifts.

As this effect appeared in both aromatic, single- and double-ring, structures, I validated the involvement of the MO quenching and conclude similar unexpected shifts for the XE spectra of other fluorinated aromatic hydrocarbons. Overall, an extension to more complex molecules, as well as a full experimental investigation, will lead to a full verification.

As can be observed in Fig. 5.23, the transitions concerning the HOMO levels are of ma-

major concern for the dC/sC observations. In naph, the HOMO transition ψ is of sole dC character, with the first sC contribution being the next feature θ . A similar observation can be made for PFnaph, however the energetic gap between ψ and the first sC contribution θ increases significantly (from 0.6 eV to 2.6 eV). Note also, the first resonance of PFnaph is of sole sC contribution. This circumstance strongly resembles the one described for PFD in chapter 5.3.1. There, a local HOMO-LUMO gap increase, as well as a site-selective RIXS excitation, was observed and discussed regarding its importance as a fingerprint investigation and role in the frontier orbital model [106]. No RIXS data could be obtained for PFnaph, but the phenomenological, as well as geometrical (both are double-ring structures), similarities lead to a similar assumption.

In chapter 5.3.2 concerning cyc-hex and PF-cyc-hex I mentioned that an increase in the number of rings will lead to an advance in the complexity of the MOs, but the MO shape of the previously less-complex (one ring less) perfluorocarbon will be observable in part. Utilising the MO pictures provided in chapter 5.4.1 for benzene and PFbenzene with the ones reported here a possible extension to aromatic perfluorocarbons can be performed. Indeed, the MOs provided in Fig. 5.19c show strong schematic similarities to the ones provided in Fig. 5.22c. To draw one example, feature *A* of benzene is the schematic equivalent to part (taking only one-ring into account) of feature *B* in naphthalene. This trend can also be confirmed for the orbitals constituting the XE spectrum, leading to a verification of this concept, as well as extending it onto aromatic perfluorocarbons.

Additionally, I want to take note of the fingerprint observation introduced in the previous chapter and discussed by Plashkevych *et al.* [90]. It was mentioned that such fingerprint investigations can be performed if the spectra of the sub-units of the polymer are little perturbed by the specific polymeric environment, as well as have a fingerprint peak. In case of naph and PFnaph, no such clear distinctive peak can be found. Even if we take the strong π^* transition, typical for aromatic molecules, into account, only PFnaph could be utilised, as the spectral positioning and shape does not resemble benzene or PFbenzene.

Therefore I conclude, that a fingerprint investigation as described by Plashkevych *et al.* [90] can not be performed.

The Fluorine K-edge

For the carbon K-edge, previously reported data by Hitchcock *et. al.* [25] was utilised to validate the theoretical prediction method provided in this work. Distortions of the perfluoro effect were found in a similar fashion to the previously reported benzene and exceptions in the XES observations were discussed with respect to MO quenching effects. The similarities found between PFD and PFnaph lead to the assumption that similar phenomenological events will be occurring in the first excitations of experimental RIXS measurements.

The fluorine K-edge of PFbenzene depicted no "shielding" effect, as discussed in chapter 5.4.1, but still exhibited the HOMO-LUMO gap differences reported for non-aromatic perfluorocarbons. As the carbon K-edge observations of PFnaph were similar to the ones reported for PFbenzene, an investigation of the fluorine K-edge is advised to prove further similarities.

Hitchcock *et. al.* report a two-fold structure for the fluorine K-edge absorption spectrum with two peaks at 689 eV and 691.7 eV respectively and the ionisation potential occurring around 693.5 eV [25] (see Fig. 5.24). On the other hand, the theoretical calculations predict a five-fold structure in this energetic region, with two features fitting to the experimental spectrum and three not being visible. In a similar way to the PFD spectrum reported in chapter 5.3.1, the experimental resolution and broadening is the most probable reason for the less feature-rich experimental spectrum. Note that, the overall spectral similarity towards PFD is astonishing and further comparisons are of interest. Still, the more meaningful comparison is with PFbenzene, as both molecules are aromatic and ring-shaped.

Through a glance at the fluorine K-edge spectrum of PFbenzene (see Fig. 5.21) similarities in the MO characters of each feature, as well as spectral shape, can be observed. The main differences between both spectra lies in intensity ratios between the features and the additional pre-peak of PFnaphthalene at 687.7 eV. Nonetheless, this pre-peak is of σ^* (C-F) character, like the main resonance of PFbenzene and PFnaphthalene, and can be seen as an extension of the main resonance due to the higher geometrical complexity. Note that, a similar pre-peak occurs for PFD in comparison with PF-cyc-hex, due to the higher complexity.

As already mentioned above and in chapter 5.4.1 concerning PFbenzene, the fluorine K-edge absorption of both single- and double-ring aromatic perfluorocarbons shows similarities towards the spectra of fluoroalkanes (see chapter 5.2) and non-aromatic, ring-shaped, perfluorocarbons (see chapter 5.3.1 and 5.3.2). In chapter 5.4.1 this phenomenon was discussed in hindsight of similar fluorine environments between all presented sam-

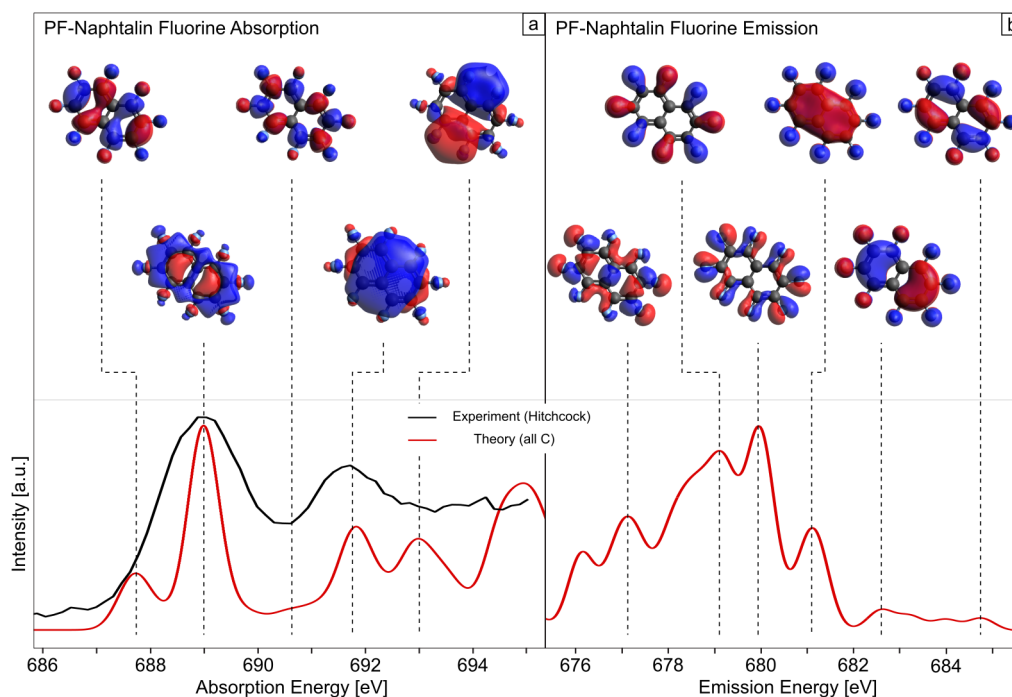


Figure 5.24: **Fluorine K-edge Data for Perfluoronaphthalene:** Theoretical fluorine K-edge X-ray absorption data for perfluoronaphthalene (a) and their respective X-ray emission data (b). The experimental data shown was obtained through Hitchcock *et. al.* [25]. The upper area illustrates the molecular orbitals for the corresponding transitions.

ples. The information on double-ring aromatic perfluorocarbons further supports this discussion and leads to a general trend for sufficiently low-complex perfluorocarbons, disregarding shape and aromatic status.

As a result I conclude that, the fluorine environment is marginally affected by the different carbons sites and geometrical shapes for sufficiently low-complex perfluorocarbons.

In a similar fashion to PFbenzene, a glance at the theoretically predicted XE spectrum reveals significant differences from spectra of non-aromatic perfluorocarbons (see Fig. 5.24). It was discussed that the spectral shape differs greatly, therefore leading to a broad experimental feature for PFbenzene in contrast to PFD or PF-cyc-hex (see chapter 5.4.1). As the spectral shape of PFnaph is comparable to PFbenzene and as similar differences towards non-aromatic perfluorocarbon spectra occur, I can conclude a similar behaviour as for PFbenzene. Nonetheless, an accurate determination of the experimental fluorine K-edge emission spectrum is recommended to confirm the differences and similarities hinted at in the theoretical predictions.

As a direct outcome from the hinted differences, the "shielding" effect was modified (see Fig. 5.4.1). Similar to PFbenzene, the "shielding" effect can not occur due to the geometrical structure of PFnaph, which allows access to the chemically active carbon centres in the molecule. The described encasing effect can also not be observed. Note however, the HOMO-LUMO gap differences are still confirmed between fluorine (≈ 7 eV) and carbon (≈ 2 eV).

Therefore, the carbon atoms are still marked as the active centres, while the reasons for the "shielding" effect are diminished in an equal manner as for PFbenzene.

Summary

The essential differences found in chapter 5.4.1 concerning aromatic and non-aromatic perfluorocarbons were confirmed through fundamental insight into the energetic shifts induced by fluorination and a comprehensive picture of naphthalene and perfluoronaphthalene based on XA and XE data. The strong MO destabilisation discovered by Brundle *et. al.* for aromatic fluorinated hydrocarbons was confirmed, albeit certain exceptions were found. These exceptions were discussed with regards to their geometrical positioning in the molecule and their subsequent molecular environment.

The missing MO transfer effect in aromatic perfluorocarbons was verified and a direct link to the free π electron system can be established. The suppressed stabilisation effect leads to the dissolution of the transfer effect, therefore also affecting the "shielding" reported for non-aromatic perfluorocarbons. With this a general trend of these concepts can be corroborated, leading to considerations of these effects only in case of non-aromatic perfluorocarbons.

The proposed idea of MO prediction through less-complex building blocks in ring-shaped fluorinated structures was additionally verified for aromatic systems.

Finally, the overall validity of concepts concerning aromatic fluorinated systems was confirmed and the proposed MO transfer and "shielding" effect ideas were refined.

5.5 Methylated Ring-Shaped Hydro- and Perfluorocarbons

The Carbon K-Edge

Perfluorocarbons are a family of molecules that come with a wide range of possible geometric structures. Beside ring- and chain-shaped structures, a few complex geometries were investigated by Brundle *et. al.* [22, 23] with special attention to structures having a "dangling" methyl group. A molecule with this methyl group will result in a "grossly non-planar system ..., for which the π - σ -distinction can no longer be made and all MOs are approximately equally stabilised by the substitution" [22]. Therefore, investigations of methylated perfluorocarbons are of interest to observe the effect of the methyl group on the perfluoro effect.

Note that, the gas dissolving capacity of methylated perfluorocarbons is higher compared to the corresponding non-methylated materials [19, 94]. This is in-line with the observations of Hamza *et. al.* that, the geometrical distortions of the fluorine substituted hydrocarbons lead to cavities in the liquid where the gas can be dissolved into [18]. Therefore, the methyl group increases the amount of distortions and extends the overall molecular surface resulting in bigger and more numerous cavities.

In this chapter I extend the benzene and cyclo-hexane molecules, as well as their fluorinated counterparts, with a methyl group (fluorinated methyl group) to observe spectral similarities and differences to non-methylated samples. Upfront I want to note that the spectral similarities are significant, which is also mirrored in the MO pictures provided. As effects due to similarities lead to equal conclusions for the methylated samples, I omit a deeper investigation of these and will refer to the corresponding non-methylated chapters 5.3.2 and 5.4.1.

As a result, this chapter will focus on the differences with appropriate referrals to previous chapters.

The experimental and theoretical XA data on methylated hydro- and perfluorocarbons is compiled in Fig. 5.25, with a clear distinction of the methyl carbon impact in the theoretical predictions. As previously stated, the energetic positioning and shifts of the XA features presented in Fig. 5.25 and table 5.11 reveal strong similarities towards the non-methylated samples (see chapter 5.3.2 and 5.4.1). Small differences in the range of several hundred meV and intensity ratios can be related to the influence of the methyl group on the geometry and MOs. Nonetheless, a huge impact can be found in the first feature of both perfluorinated samples.

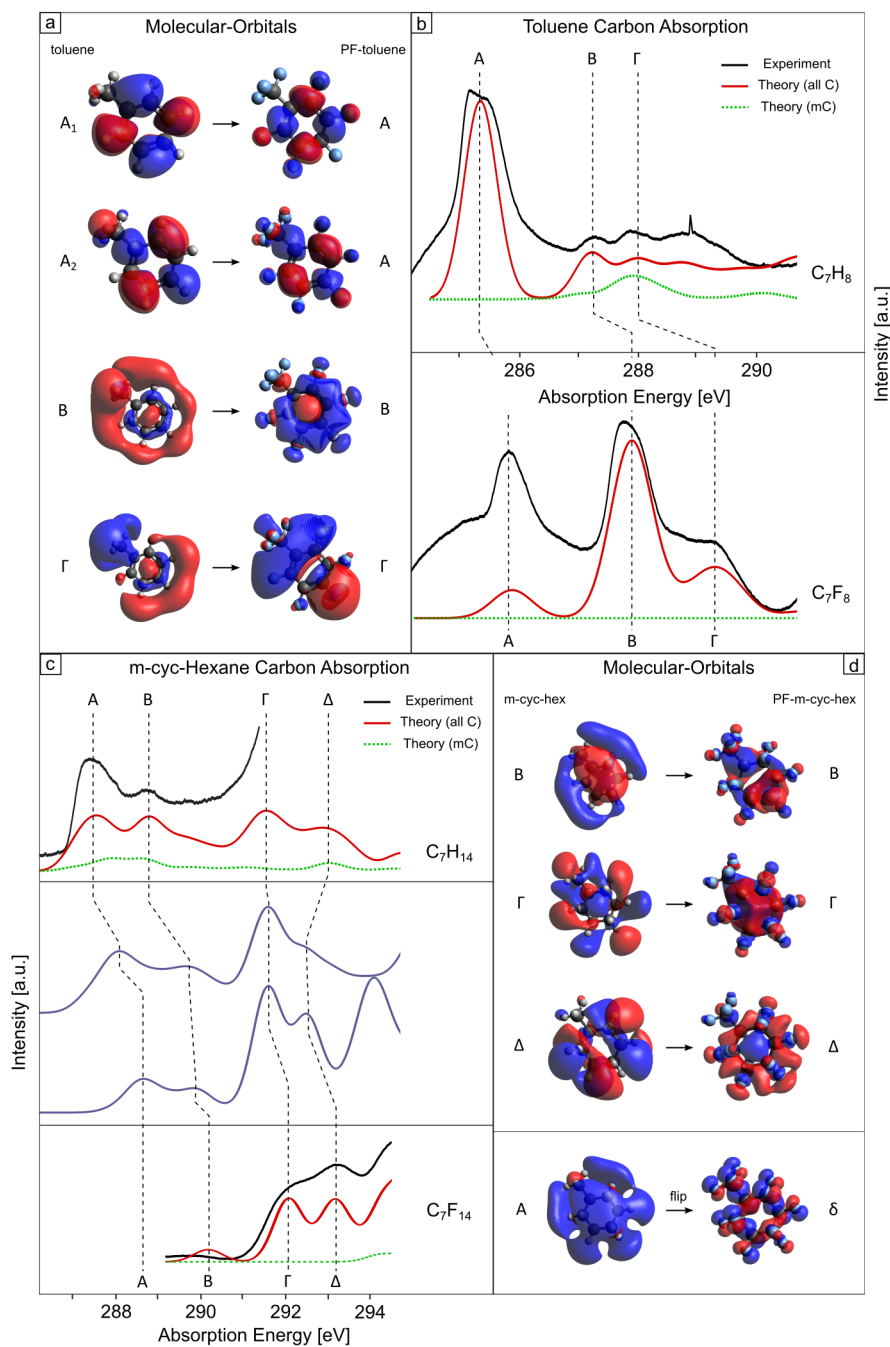


Figure 5.25: **Carbon K-edge Absorption for Methylated-Ring Perfluorocarbons:** (b) and (d) show the experimental (black lines) and calculated (red lines) carbon K-edge X-ray absorption spectra for methylated single-ring perfluorocarbons. Dashed lines are utilised to indicate the shifts of the spectral features and visualised in (c). MOs for the corresponding methylated single-ring perfluorocarbon shifting features are labelled in (a) and (e).

feature	energetic position toluene [eV]	energetic position PF-toluene [eV]	energy shift upon complete fluorination [eV]	orbital character
<i>A</i>	285.3	285.8	0.5	π^* (C-H)
<i>B</i>	287.3	287.8	0.5	π^* (C-H)
Γ	288	289.3	1.3	σ^* (C-C) / π^* (C-H)

feature	energetic position m-cyc-hex [eV]	energetic position PF-m-cyc-hex [eV]	energy shift upon complete fluorination [eV]	orbital character
<i>A</i>	287.4	-	-	not distinguishable
<i>B</i>	288.7	290.2	1.5	σ (C-C)
Γ	291.4	292.2	0.8	π
Δ	293.2	293.2	0.0	π

Table 5.11: **Methylated-Ring Perfluorocarbons XA Carbon K-edge Character Table:** Energetic shifts, positions and derived MO characters for the XA features.

In case of perfluorotoluene (PF-toluene), the first feature loses a significant amount of intensity and changes from a two-fold structure in PF-benzene to a one-peak structure with two transitions underlying. A glance at the MOs (see Fig. 5.25a and Fig. 5.19c) reveals that the orbital denoted as A_1 is unaffected by the methyl group extension, depicting an orbital equal to the PF-benzene counterpart. The A_2 MO on the other hand is extended onto the methyl group, though no direct involvement of the methyl carbon in the transition process can be found. Nonetheless, the extension of the MO lead to an energetic shift change in comparison to the PF-benzene feature, resulting in the disappearance of the shoulder feature in PF-benzene.

Additionally I want to note that the direct involvement of the methyl carbon in the transition processes can not be confirmed in the near-edge features.

For perfluoro-methyl-cyclo-hexane (PF-m-cyc-hex) the first feature alters, as an additional peak appears at 290.2 eV in comparison to PF-cyc-hex. This pre-peak feature can

be found to relate to the energetic shift induced by the perfluoro effect of the m-cyc-hex feature *B*. Referring to the previously reported PF-cyc-hex, feature *B* vanished due to the MO transfer effect and reappeared in the XE spectrum. Inspecting the corresponding MO (see Fig. 5.25e and Fig. 5.16c) reveals, similar to the toluene case, a distortion and extension of the MO onto the methyl group. Note that, the other MO transfer feature *A* is affected less by the distortion leading to similar MO pictures. Additionally, the core-level orbitals shift by several eV (≈ 2 eV) due to the methyl carbon core orbital. As mentioned in chapter 5.2 about chain-shaped perfluorocarbons, the MO transfer effect results from the MO stabilising of the perfluoro effect, the σ -shifting effect and the electronegativity of fluorine. In case of PF-m-cyc-hex, the MO stabilising effect is disturbed due to the methyl group, as previously described by Brundle *et. al.* [22]. Consequently, the MOs strongly affected by the methyl group extension can't exhibit the MO transfer, leading to the different observations for feature *B* between non-methylated and methylated perfluorocarbons.

Utilising this information, I can refine the description of the MO transfer effect to include a passage about methylated samples, creating a more general description.

For both aromatic and non-aromatic methylated samples the energetic shifts exhibited are in-line with the rules of the perfluoro effect (see table 5.11). This stands in contrast to the observations of the non-methylated samples and arguments by Brundle *et. al.* [22].

Concerning non-aromatic samples, Brundle *et. al.* discussed that the MO stabilising effect is disturbed due to the methyl group [22]. At a glance this can't be observed for m-cyc-hex, but a deeper investigation validates the literature statement. We have to differentiate between the shifts of orbitals strongly affected by the methyl group extension and those with minor changes due to the extension. Strongly affected MOs reveal energetic shifts that start to change in an unfavourable fashion for the perfluoro effect rules after adding the methyl group (e.g. Γ with 0.3 eV changes to 0.8 eV). In contrast, the less affected MOs are still, as before, in agreement with the rules (e.g. Δ). Therefore, we have to differentiate between the MOs to affirm the statement made by Brundle *et. al.*.

For aromatic perfluorocarbons, I discovered in previous chapters that the energetic shifts are overemphasised due to the free π electron system. After adding the methyl group to benzene, the energetic shifts stabilised and are comprising with the perfluoro effect rules. This correlates to the statement of Brundle *et. al.* in a different way from the non-aromatic perfluorocarbons [22]. In case of aromatic perfluorocarbons, the methyl group seems to stabilise part of the π electron system (see MOs in Fig. 5.25a) leading to a significant diminishing of the influence the π system had on the perfluoro effect.

Note that, the shifts are now in-line with the rules, but still not perfectly exhibited. Therefore, the statement by Brundle *et. al.* [22] has to be revised for the XA process for different types of perfluorocarbons.

The XE data of methylated hydro- and perfluorocarbons is compiled in Fig. 5.26, delivering an overall uneventful picture. Note that only theoretical predictions are provided with an additional clear distinction of the methyl carbon impact. The similarities towards non-methylated samples (see chapter 5.3.2 and 5.4.1) are evident and the energetic positioning and shifts are compiled in table 5.12.

feature	energetic position toluene [eV]	energetic position PF-toluene [eV]	energy shift upon complete fluorination [eV]	orbital character
α	275.6	274.6	-1.0	σ (C-C) / π (C-H)
β	276.7	275.9	-0.8	π
γ	277.8	281	+3.2	π (C-C) / σ^* (C-H)
δ	278.4	280.1	+1.7	σ (C-C) / σ (C-H)
ε	280.8	283.5	+2.7	π^* (C-C) / σ^* (C-H)

feature	energetic position m-cyc-hex [eV]	energetic position PF-m-cyc-hex [eV]	energy shift upon complete fluorination [eV]	orbital character
α_1	275.6	276.4.4	+1.3	π / not distinguishable
α_2	277.2	276.4	-0.4	π
β	279.3	277.7	-3.5	σ
γ	-	281.9	-	σ (C-C)
δ	-	284.1	-	σ (C-C)

Table 5.12: **Methylated-Ring Perfluorocarbons XE Carbon K-edge Character Table:** Energetic shifts, positions and derived MO characters for the XE features.

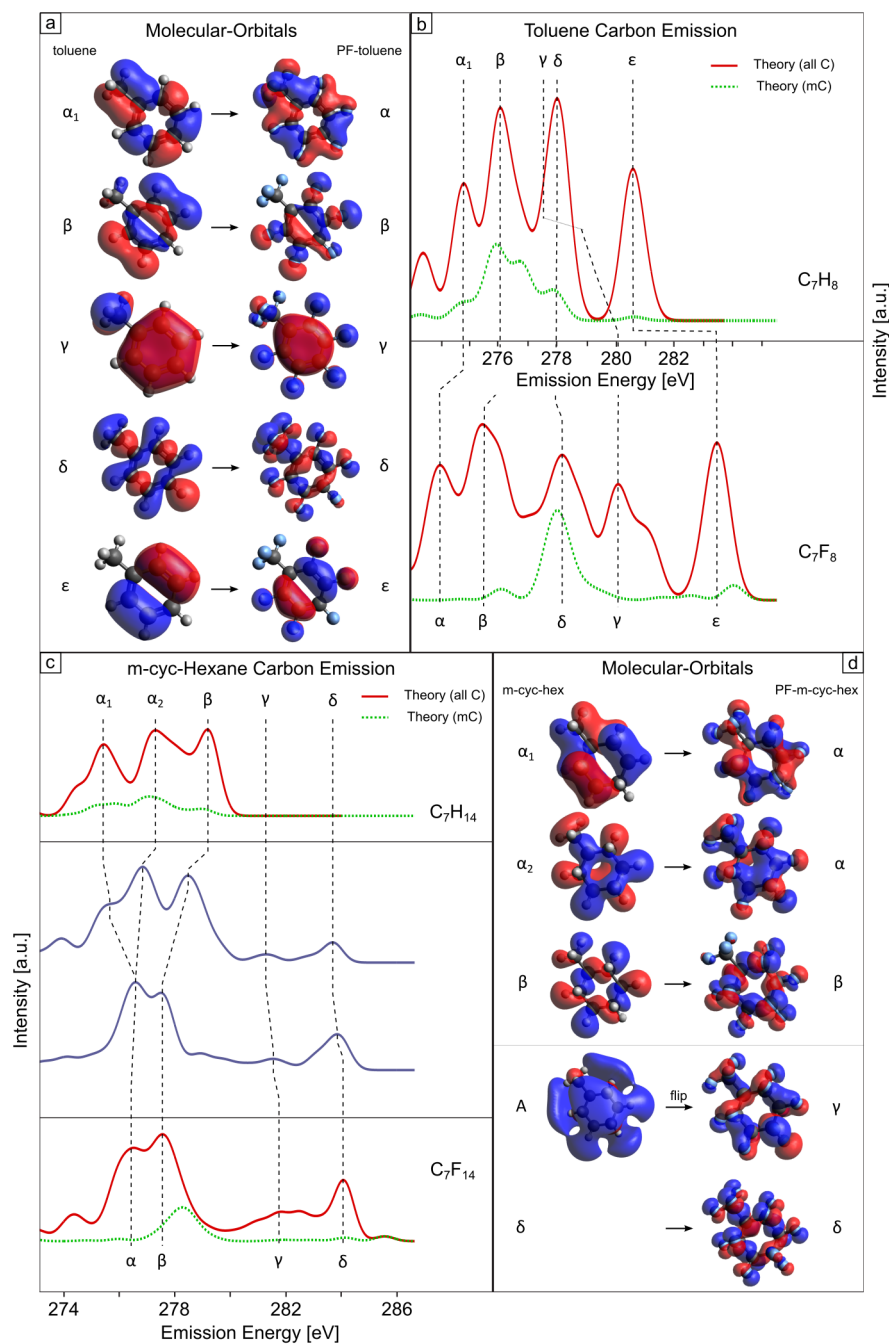


Figure 5.26: **Carbon K-edge Emission for Methylated-Ring Perfluorocarbons:** (b) and (d) show the experimental (black lines) and calculated (red lines) carbon K-edge X-ray emission spectra for methylated single-ring perfluorocarbons. Dashed lines are utilised to indicate the shifts of the spectral features and visualised in (c). MOs for the corresponding methylated single-ring perfluorocarbon shifting features are labelled in (a) and (e).

As previously stated for the non-aromatic PF-m-cyc-hex, the MO transfer effect was modified by the methyl group. On a first glance the predictions don't reveal any difference between the methylated and non-methylated specimen, but the second MO transfer feature δ , which should have vanished as B does not transfer, is still visible. Additionally, the occupied MO δ changed to a shape comparable to γ , which is involved in the transfer process of A .

I conclude that A is also the origin of δ , due to the similarities of δ and γ . Note that, the previously mentioned shift of the core-level orbitals also affects the XE spectrum significantly, leading to a shift of the relaxations, possibly resulting in the 2 eV difference between γ and δ . This is supported by the theoretical predictions of the XE spectrum further validating this statement.

The XE spectra of the aromatic methylated sample PF-toluene behaves equivalent to the previously reported PF-benzene (see chapter 5.4.1). The energetic shifts are in-line with the perfluoro effect, which was discussed with regard to the electron distribution and orbital localisation for PF-benzene. In case of PF-toluene, I established the fact that the methyl group stabilises part of the free π electron system leading to the differences between the methylated and non-methylated XA spectra. Concerning the XE energy shifts, this effect is further emphasised. Nonetheless, the previously reported exceptions γ and ε still have overemphasised shifts, albeit not as pronounced.

The reported quenching, or "encasing", of the hydrocarbon MO upon fluorination instead of stabilising for PF-benzene can also be observed for PF-toluene (see Fig. 5.26a). As a result, the corresponding MOs are affected similarly to the non-methylated ones, leading to the same smeared out perfluoro effect, albeit with a weaker quenching effect in methylated samples due to the stabilising methyl group.

In summary, the methyl group extension exhibited different effects concerning aromatic and non-aromatic perfluorocarbons. In case of aromatic perfluorocarbons the methyl group stabilised part of the free π electron system leading to a change in the previously established rules governing the perfluoro effect of aromatic non-methylated perfluorocarbons. The impact on the MOs was the strongest as the extension led to differences in energetic shifts upon fluorination and a refinement of the literature statement concerning methylated perfluorocarbons [22]. The non-aromatic samples experienced a destabilisation effect from the methyl group extension, basically affecting the MO transfer first reported in chapter 5.2 for fluoroalkanes.

The Fluorine K-Edge

The overall similarities between the carbon spectra of methylated and non-methylated samples were astonishing, but the few differences delivered a clear picture of the influence the methyl group has on the concepts found for aromatic and non-aromatic perfluorocarbons.

In a similar fashion the fluorine K-edge will be investigated, with special concern given to the differences.

The fluorine K-edge XA spectra of methylated perfluorocarbons are presented in Fig 5.27a with the respective theoretical predictions. The different fluorine sites (attached to the methyl carbon (mF) or the other carbon atoms) are also depicted and demonstrate a clear difference between aromatic and non-aromatic samples. This is a result originating from the difference in ratio between the fluorine sites, as the ratio of PF-toluene is 5:3 and for PF-m-cyc-hex 10:3. Therefore, this leads to a higher impact of the methyl fluorines for aromatic samples in comparison to non-aromatic perfluorocarbons. Note however, the spectral similarities, as well as the corresponding MO similarities, between the methylated and non-methylated samples is evident, leading to corresponding arguments.

In chapter 5.4.1 I discussed the similar environments of the fluorine atoms in different perfluorocarbons, which also holds true for methylated samples. Therefore, I can attribute the similarities between the spectral shapes of both methylated samples to the structural similarities of the fluorine atom environments, while minor differences, like the sharp valley in PF-toluene, occur due to the differences of connected carbon sites. Note that, the two-fold structure of the first feature of PF-toluene can be attributed to the previously mentioned core-level shift induced by the methyl group carbon.

The fluorine encasing, the basis for the "shielding" effect reported for non-aromatic perfluorocarbons, can also be found for non-aromatic methylated samples. A glance at the MOs (see Fig. 5.27a) validates this and hints can also be found for the aromatic PF-toluene. However, the encasing is only occurring at one edge of the hexagonal shaped structure where the methyl group is attached. This does not lead to a full "shielding", diminishing the importance of this effect in simple aromatic methylated perfluorocarbons. I assume that, three methyl groups attached to PF-benzene (one at every two carbon atoms of the ring) will lead to a full encasing and a subsequent "shielding" effect.

This "shielding" is also supported by the HOMO-LUMO gap differences between fluorine and carbon. A glance at the XE spectra of methylated perfluorocarbons reveals a gap, which is also essential for the "shielding" to occur. The energetic gap can be confirmed

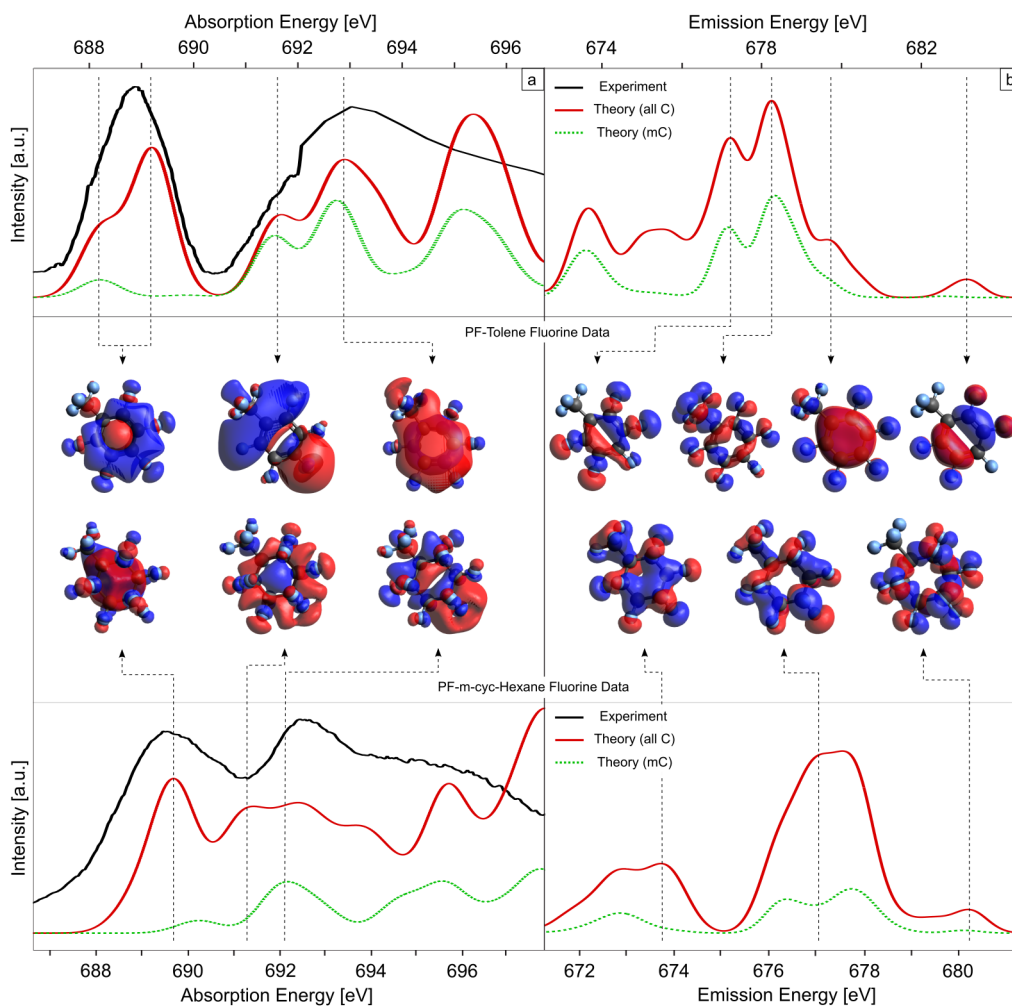


Figure 5.27: **Fluorine K-edge Data for Methylated-Ring Perfluorocarbons:** Theoretical and experimental fluorine K-edge X-ray absorption data for methylated single-ring perfluorocarbons (a) and their respective X-ray emission data (b). The middle area illustrates the MOs for the corresponding transitions.

for aromatic (C is ≈ 2.5 eV, F is ≈ 5 eV) and non-aromatic (C is ≈ 6 eV, F is ≈ 9 eV) methylated perfluorocarbons, identifying the carbon site as the chemically active centre in the frame of the frontier orbital model [106] in both cases. Nonetheless, the shielding effect can only occur in the non-aromatic PF-m-cyc-hex, as the geometrical positioning in PF-toluene is unfavourable.

Overall, the spectral and MO similarities of the fluorine studies of methylated and non-methylated samples is striking and an extension of the analytical methodology can be proposed for sufficiently small perfluorocarbons, independent of the aromatic and methylated status.

Summary

The extension of concepts and investigation of differences between non-methylated and methylated perfluorocarbons was successfully performed through fundamental insights into XA and XE data, as well as energetic shifts induced by fluorination, for aromatic and non-aromatic samples. Additional TD-DFT calculations gave rise to the discovery of impacts delivered by the methyl group to the corresponding spectra.

The surprising abiding of PF-toluene towards the perfluoro effect rules, in contrast to other aromatic perfluorocarbons, was discovered and discussed in consideration of the methyl groups stabilising effect on the free π electron system. Considering similar points, the non-aromatic PF-m-cyc-hex molecule was discussed and a direct impact on the MO transfer effect was found. Additionally, the core-level shift induced by the methyl group leads to surprising effects with regards to the MO transfer. Overall, the methyl group led to an extension and modification of most MOs, which did not lead to significant spectral differences between methylated and non-methylated perfluorocarbons.

A difference in spectral impact was discussed for aromatic and non-aromatic methylated perfluorocarbons, which resulted in the discovery of similar fluorine atom environments in both examples, comparable to observations of non-methylated samples. The "shielding" effect and corresponding HOMO-LUMO gap differences were confirmed leading to a similar behaviour as described in previous chapters.

Finally, the validation of various concepts and their extension to the corresponding methylated samples was achieved, hinting at a generalisation of the origin of the chemical and biological inertness of perfluorocarbons, as well as their other special characteristics.

6 Summary and Conclusions

Over the course of all chapters, several new and previously reported concepts were developed and refined utilising a comprehensive picture of the electronic structure of hydrocarbons and their respective fluorinated counterparts based on XA, XE and RIXS spectroscopic data. Additional TD-DFT calculations for the presented samples were also performed and presented.

Insights into the energetic shift induced by fluorination, the so-called perfluoro effect, were drawn and provided significant connections to fundamental processes. Differences regarding the perfluoro effect for variations in geometrical structure and aromatic status were established. My first observations of chain-shaped hydro- and perfluorocarbons revealed an abiding of the energetic shifts to the perfluoro effect rules drawn by Brundle *et. al.* [22, 23]. Note that, the shifts are similar for all presented chain-lengths. Incorporating investigations of other non-aromatic samples, like perfluorodecalin, further supported the known rules and extended my investigation onto ring-shaped systems. Additionally, to the best of my knowledge, the observability of the perfluoro effect *via* XE spectroscopy was confirmed for the first time.

Expected problems with regards to the perfluoro effect of aromatic perfluorocarbons were observed and the analysis proposed by Brundle *et. al.* was employed to obtain the experimental energetic shift data. Surprisingly, the energetic shifts were generally overemphasised, inhibiting the possibility of observations as the stated rules don't apply anymore. This overemphasis was reported previously in literature [90] and discussed with regards to differences in observation methods. The perfluoro effect rules were initially developed through photoelectron spectroscopy, but my and literature observations were obtained by XA processes. The difference in ionisation status between these methods leads to the perfluoro effect problems, which I address by extending the literature discussion onto more aromatic complexes and confirming their origin. Note that, later investigations on aromatic methylated samples pointed to an additional effect. I discovered that the perfluoro effect rules still hold true for XA spectroscopy observations of aromatic perfluorocarbons, if the carbon atoms are less affected by changes in the aromatic π electron system during the fluorination process. Additionally, the rules hold true for all aromatic XE measurements, due to the intrinsic differences between occupied

and unoccupied orbitals, such as the electronic nodal planes and electron distribution. Special attention was provided to the differences in electron distribution as, in case of occupied MOs, more localised orbitals are expected in comparison to unoccupied ones. Therefore, this results in a stronger fluorine stabilisation effect and lower the probability of overlap processes, directly leading to a less smeared out perfluoro effect. However, special MOs can be found, where the fluorine strongly quenches, or "encases", the hydrocarbon MO upon fluorination instead of stabilising it, still leading to a smeared out perfluoro effect.

Note that, every sample in this work is subject to the so-called " σ -shifting" effect, especially in the case of the carbon atoms having a fluorine atom as nearest neighbour. This shifting is one of the prerequisites for the MO transfer effect proposed in this work. A transfer of MOs from the unoccupied into the occupied region was observed due to the above mentioned σ -shifting, as well as the high amount of extra orbitals from substituting hydrogen with fluorine. Additionally, the partial charge distribution change, induced by the highly electronegative fluorine, played a major role. It resulted in the depopulation of most carbon orbitals, leading to a dominance of fluorine signals and a subsequent transfer of specific orbitals from the unoccupied to the occupied orbital region. My data also supports a significant increase of the HOMO-LUMO gap for the last fluorination step ($C_xF_yH_1$ to C_xF_{y+1}) in all non-aromatic samples, induced by the MO transfer. In the frame of the frontier orbital model, this suggests a higher relative inertness, giving us a hint on the origin of the strong chemical and biological inertness properties of perfluorocarbons.

Overall, this MO transfer could only be observed for non-aromatic perfluorocarbons, regardless of their methylation status. In case of aromatic systems I discovered that, the stabilisation effect upon fluorination is suppressed by the free π electron system, leading to the dissolution of the transfer effect. I additionally discussed the link to possible molecule and polymer enhancement methods through fluorination treatment.

A glance at the MOs of non-aromatic perfluorocarbons also suggested a "shielding" effect in earlier parts of this work. In case of this shielding effect, the fluorine acts like a shield (potential barrier) for the chemically active carbon site, inhibiting intermolecular interactions. One of the prerequisites for this effect was an appropriate geometry, where the fluorine are "encasing" the carbon atoms. This works especially well for non-aromatic perfluorocarbons, as such carbon structures have regularly placed fluorine atoms surrounding them (see Fig. 5.1). Regarding aromatic structures, this effect could not be confirmed. Nonetheless, through methylation a partial "encasing" could be observed, hinting at the possibility of specially manufactured aromatic perfluorocarbons utilising the "shielding" effect.

Another important concept for "shielding" is a HOMO-LUMO gap difference between carbon and fluorine sites. This is needed to confirm carbon as the chemically active site and support the intermolecular interactions inhibiting effect in the frame of the frontier orbital model. I could confirm this gap difference for all perfluorocarbons, independent of their aromatic and methylation status. In general, the HOMO-LUMO gap of the fluorine site was larger by approximately double the amount of the carbon site gap.

A special phenomenon was observed for the chain-type perfluorocarbons, perfluorohexane, -heptane and -octane. The conformation effect, resulting from different molecular conformations, was discussed with regards to the substitution of hydrogen by the more electronegative and bigger fluorine. This effect was also modified by the chain-lengths of the sample and had different impacts on the LUMO transitions. As a result, this changed the intermolecular interactions in the frame of the frontier orbital model, affecting the capacity to dissolve other liquids and gases in the perfluorocarbon. Further support from literature could also be drawn [2, 18].

The methylated groups also had to be investigated in a deeper manner. Here, the direct influence of the methyl group atoms on the near-edge transitions was found to be not very significant, but an indirect impact could be observed. The methyl group atoms had significant impact on the MOs, leading to a "quenching" of the previously non-methylated MOs and a following effect on the transitions of the transformed MOs. Additionally, the statement by Brundle *et. al.*, that "dangling" methyl groups lead to equally stabilised MOs and therefore no distinct perfluoro effect, was found in need of refinement. Overall, this statement is true for highly complex methylated perfluorocarbons, but in less complex ones, like studied here, a distinction between aromatic and non-aromatic status needs to be made. In case of non-aromatic systems, the statement is valid as the system is perturbed leading to a modification of the perfluoro effect. On the other hand, in aromatic systems the methyl group seems to stabilise part of the free π electron system, leading to a significant diminishing of the negative influence the π electron system has on the perfluoro effect, subsequently supporting it.

I also presented the utility of splitting the carbon sites according to their respective fluorine-bond number sub-species. As the amount of fluorine bonded to one carbon atom strongly affects the electron distribution and net-charges, such distinctions were deemed useful. In perfluorodecalin, this delivered deeper insight into site-selective excitations, especially in the RIXS dynamics investigations.

Note that, this site-separation is not needed for fluorine, as the fluorine environment is similar due to the nearest neighbour being carbon in all cases. Small differences can only be observed if the carbon site, where the fluorine is attached to, is vastly different from the others.

Overall, significant spectral similarities regarding energetic positions and spectral shape were discovered. Specifically, the fluorine spectra were comparable throughout all presented samples due to the structural and environmental similarities between the different fluorine atoms. In case of the carbon spectra, a separation with regards to the aromatic status had to be discussed as the carbon spectra of non-aromatic and aromatic systems were significantly different. Note that, the spectra in the frame of similar aromatic status are equivalent in most spectral parameters.

The postulation of a MO shape prediction method of ring-shaped perfluorocarbons was also achieved. It was concluded that, an increase in the number of rings will lead to an enhancement in complexity of the concerned MO, but the MO shape of the previously less-complex (one ring less) perfluorocarbons will be observable in part. A similar prediction method can also be used for chain-shape perfluorocarbons, because the MO of the previously shorter chain is only extended by the increasing chain-lengths.

Finally, the possibility of fingerprint building block investigations for polymeric compounds was discussed. This notion was first presented by Plashkevych *et. al.* [90] for HOMO to core transitions. The problem was, to successfully execute such fingerprint investigation, the spectra of the sub-units of the polymer have to be little perturbed by the specific polymeric environment and deliver a clear fingerprint feature. I extended this discussion onto the LUMO to core transitions and liquid environments, as well as non-aromatic samples. Note that, the non-aromatic systems presented in this work rarely occur in polymeric compounds and one has to test the overall utility of these observations.

To summarise, several concepts were discussed and presented with regards to fluorine electronegativity, structural shape and other argued approaches. In all cases the importance of the chemical and biological inertness of the studied perfluorocarbons was emphasised and the possibility to extend the studies onto gas loaded systems was contemplated. Direct links to the capacity of dissolving gases and other liquids were made and commented on with regards to the frontier orbital model.

Overall, a deep study establishing insight into several structurally different perfluorocarbons was performed and experimental, as well as theoretical, analysis methodologies were developed and utilised.

7 Outlook

As this work delivered part of the puzzle to solve the mysteries behind the chemical and biological characteristics of perfluorocarbons, new possible investigation methods and directions became feasible.

The first outlook onto the future would be the extension of the delivered analytical methodology onto other perfluorocarbons, possibly even highly fluorinated polymeric compounds like Teflon. This would lead to a clarification and validation of the developed concepts in this work, pointing to a possible extrapolation of the proposed explanations onto the whole family of perfluorocarbons.

Special attention should also be provided to the experimental data that could not be delivered in this work, as a fully experimental study would enrich the discussion further. I'd like to give a few examples of possible highly complex perfluorocarbons to encourage further studies in this field:

- extending the alkane chain further (longer than C_8H_{18})
- methylating the presented chain-shaped perfluorocarbons
- extending the ring structures with more rings/side-chains
- utilising different ring-shapes (bigger/smaller rings)
- increasing the number of methyl groups

I'd also like to recommend the use of molecular dynamics calculations. Such type of calculations will deliver a clearer picture of the different conformations in the chain-shaped perfluorocarbons and, if gas load can be simulated, the possibility of cavities as gas capacity origin could be confirmed. Additionally, the shape of the cavities can be estimated, especially for different kinds of gases. Therefore, this can help understand why different gases have different capacities to dissolve in differing fluorinated structural geometries.

It would also prove advantageous if other spectroscopic methods are considered, like Infrared or Raman spectroscopy. Here, the molecular vibrations are measured, which would help to understand the cavity theory further and what type of cavities can exist. The extension of the spectroscopic methodology in this work to gas loaded samples, best

case with different gases, and obtaining difference spectra would also be beneficial.

The last point I want to address is the fingerprint method proposed by Plashkevych *et al.*. The possible extension to non-aromatic samples can be investigated further and the methods utility be proven by manufacturing polymeric compounds with following spectroscopic observations.

Bibliography

- [1] K.C. Lowe. Perfluorinated blood substitutes and artificial oxygen carriers. *Blood Reviews*, 13(3):171–184, September 1999.
- [2] M.G. Freire, L. Gomes, L.M.N.B.F. Santos, I.M. Marrucho, and João A.P. Coutinho. Water Solubility in Linear Fluoroalkanes Used in Blood Substitute Formulations. *The Journal of Physical Chemistry B*, 110(45):22923–22929, November 2006.
- [3] J.G. Riess and M. Le Blanc. Solubility and transport phenomena in perfluorochemicals relevant to blood substitution and other biomedical applications. *Pure and Applied Chemistry*, 54(12), January 1982.
- [4] J.G. Riess and M. Le Blanc. Perfluoro Compounds as Blood Substitutes. *Angewandte Chemie International Edition in English*, 17(9):621–634, September 1978.
- [5] R.M. Winslow, K.D. Vandegriff, and M. Intaglietta. *Blood Substitutes: New Challenges*. Springer Science & Business Media, December 2012.
- [6] C. Cecutti, I. Rico, A. Lattes, A. Novelli, A. Rico, G. Marion, A. Graciaa, and J. Lachaise. New formulation of blood substitutes: optimization of novel fluorinated microemulsions. *European Journal of Medicinal Chemistry*, 24(5):485–492, September 1989.
- [7] S. Sarkar. Artificial blood. *Indian Journal of Critical Care Medicine : Peer-reviewed, Official Publication of Indian Society of Critical Care Medicine*, 12(3):140–144, 2008.
- [8] C.J. van Oss. *Transfusion Immunology and Medicine*. CRC Press, January 1995.
- [9] C.S. Cohn and M.M. Cushing. Oxygen Therapeutics: Perfluorocarbons and Blood Substitute Safety. *Critical Care Clinics*, 25(2):399–414, April 2009.
- [10] S.J. Urbaniak. Artificial blood. *BMJ : British Medical Journal*, 303(6814):1348–1350, November 1991.
- [11] J.-Y. Chen, M. Scerbo, and G. Kramer. A review of blood substitutes: examining the history, clinical trial results, and ethics of hemoglobin-based oxygen carriers.

- Clinics*, 64(8):803–813, 2009.
- [12] T. Suyama, K. Yokoyama, and R. Naito. Development of a perfluorochemical whole blood substitute (Fluosol-DA, 20)—an overview of clinical studies with 185 patients. *Progress in Clinical and Biological Research*, 55:609–628, 1981.
- [13] E. Nüiler. Setbacks for blood substitute companies. *Nature Biotechnology*, 20(10):962–963, October 2002.
- [14] M.C. Papo, P.R. Paczan, B.P. Fuhrman, D.M. Steinhorn, L.J. Hernan, C.L. Leach, B.A. Holm, J.E. Fisher, and B.A. Kahn. Perfluorocarbon-associated gas exchange improves oxygenation, lung mechanics, and survival in a model of adult respiratory distress syndrome. *Critical Care Medicine*, 24(3):466–474, March 1996.
- [15] P. Lynch, L. Krasner, T. Vinciguerra, and T. Shaffer. Effects of intravenous perfluorocarbon and oxygen breathing on acute decompression sickness in the hamster. *Undersea biomedical research*, 16(4):275–281, July 1989.
- [16] M. Velikay, A. Wedrich, U. Stolba, P. Datlinger, Y. Li, and S. Binder. Experimental Long-term Vitreous Replacement With Purified and Nonpurified Perfluorodecalin. *American Journal of Ophthalmology*, 116(5):565–570, November 1993.
- [17] F. Bottoni, G. Bailo, P. Arpa, A. Prussiani, M. Monticelli, and V. de Molfetta. Management of giant retinal tears using perfluorodecalin as a postoperative short-term vitreoretinal tamponade: a long-term follow-up study. *Ophthalmic surgery*, 25(6):365–373, June 1994.
- [18] M'H.A. Hamza, G. Serratrice, M.J. Stebe, and J.J. Delpuech. Solute-solvent interactions in perfluorocarbon solutions of oxygen. An NMR study. *Journal of the American Chemical Society*, 103(13):3733–3738, July 1981.
- [19] A.M.A. Dias, M. Freire, J.A.P. Coutinho, and I.M. Marrucho. Solubility of oxygen in liquid perfluorocarbons. *Fluid Phase Equilibria*, 222-223:325–330, August 2004.
- [20] J.-A. Ma and D. Cahard. Asymmetric Fluorination, Trifluoromethylation, and Perfluoroalkylation Reactions. *Chemical Reviews*, 104(12):6119–6146, December 2004.
- [21] J.T. Welch, editor. *Selective Fluorination in Organic and Bioorganic Chemistry*, volume 456 of *ACS Symposium Series*. American Chemical Society, Washington, DC, February 1991.
- [22] C.R. Brundle, M.B. Robin, and N.A. Kuebler. Perfluoro effect in photoelectron spectroscopy. II. Aromatic molecules. *Journal of the American Chemical Society*, 94(5):1466–1475, March 1972.

-
- [23] C.R. Brundle, M.B. Robin, N.A. Kuebler, and H. Basch. Perfluoro effect in photoelectron spectroscopy. I. Nonaromatic molecules. *Journal of the American Chemical Society*, 94(5):1451–1465, March 1972.
- [24] K. Fukui, T. Yonezawa, and H. Shingu. A Molecular Orbital Theory of Reactivity in Aromatic Hydrocarbons. *The Journal of Chemical Physics*, 20(4):722–725, April 1952.
- [25] M.B. Robin, I. Ishii, R. McLaren, and A.P. Hitchcock. Fluorination effects on the inner-shell spectra of unsaturated molecules. *Journal of Electron Spectroscopy and Related Phenomena*, 47(0):53–92, 1988.
- [26] P. Decleva, M. Stener, D.M.P. Holland, A.W. Potts, and L. Karlsson. Perfluoro effects in the occupied and virtual valence orbitals of hexafluorobenzene. *Journal of Physics B: Atomic, Molecular and Optical Physics*, 40(14):2939, July 2007.
- [27] I. Ishii, R. McLaren, A.P. Hitchcock, K.D. Jordan, Y. Choi, and M.B. Robin. The sigma* molecular orbitals of perfluoroalkanes as studied by inner-shell electron energy loss and electron transmission spectroscopies. *Canadian Journal of Chemistry*, 66(8):2104–2121, August 1988.
- [28] F. Neese. The ORCA program system. *Wiley Interdisciplinary Reviews: Computational Molecular Science*, 2(1):73–78, January 2012.
- [29] C. Jung, F. Eggenstein, S. Hartlaub, R. Follath, J.S. Schmidt, F. Senf, M.R. Weiss, T. Zeschke, and W. Gudat. First results of the soft X-ray microfocus beamline U41-PGM. *Nuclear Instruments and Methods in Physics Research Section A: Accelerators, Spectrometers, Detectors and Associated Equipment*, 467-468, Part 1:485–487, July 2001.
- [30] M. Nagasaka, H. Yuzawa, T. Horigome, A.P. Hitchcock, and N. Kosugi. Electrochemical Reaction of Aqueous Iron Sulfate Solutions Studied by Fe L-Edge Soft X-ray Absorption Spectroscopy. *The Journal of Physical Chemistry C*, 117(32):16343–16348, 2013.
- [31] F. Gel'mukhanov and H. Agren. Resonant X-ray Raman scattering. *Physics Reports*, 312(3-6):87–330, May 1999.
- [32] L.C.Jr. Clark. *Introduction to Fluorocarbons*. International Anesthesiology Clinics, 1 edition, March 1985.
- [33] H. Haken and H.C. Wolf. *The Physics of Atoms and Quanta: Introduction to Experiments and Theory*. Springer, Berlin ; New York, 7th rev. and enlarged ed. 2005 edition, September 2005.

- [34] C.R. Nave. *Hyperphysics: Electromagnetic Spectrum*.
- [35] D.J. Griffiths. *Introduction to Quantum Mechanics*. Pearson Prentice Hall, Upper Saddle River, NJ, 2nd edition edition, April 2004.
- [36] M. van Veenendaal. *Theory of Inelastic Scattering and Absorption of X-rays*. Cambridge University Press, Cambridge, United Kingdom, January 2015.
- [37] W.W. Parson. *Modern Optical Spectroscopy: With Exercises and Examples from Biophysics and Biochemistry*. Springer Berlin Heidelberg, Dordrecht ; New York, 1st ed 2007. 2nd printing 2009 edition, October 2008.
- [38] G.H. Zschornack. *Handbook of X-Ray Data*. Springer, New York, 2007 edition edition, March 2007.
- [39] A. Thompson, D. Attwood, E. Gullikson, M. Howells, K.-J. Kim, J. Kirz, J. Kortright, I. Lindau, Y. Liu, P. Pianetta, A. Robinson, J. Scofield, J. Underwood, G. Williams, and H. Winick. *X-Ray Data Booklet*. Lawrence Berkeley National Laboratory, University of California, 3 edition, October 2009.
- [40] F. Jensen. *Introduction to Computational Chemistry: Second Edition*. JW, Chichester, England ; Hoboken, NJ, 2 edition, December 2011.
- [41] P. Day. *The Philosopher's Tree: A Selection of Michael Faraday's Writings*. CRC Press, February 1999.
- [42] J.C. (1831-1879) Maxwell. *A treatise on electricity and magnetism. Vol. 2*. Cambridge University Press, September 2014.
- [43] P.A.M. Dirac. *The Principles of Quantum Mechanics*. Clarendon Press, 4th edition edition, February 1982.
- [44] C. Cohen-Tannoudji, B. Diu, and F. Laloe. *Quantenmechanik*. Gruyter, October 1999.
- [45] J.J. Sakurai. *Advanced Quantum Mechanics*. Addison-Wesley Educational Publishers Inc, June 1967.
- [46] T. Brandenburg, T. Petit, A. Neubauer, K. Atak, M. Nagasaka, R. Golnak, N. Kosugi, and E.F. Aziz. Fluorination-dependent molecular orbital occupancy in ring-shaped perfluorocarbons. *Physical Chemistry Chemical Physics*, 17(28):18337–18343, July 2015.
- [47] M.O. Krause. Atomic radiative and radiationless yields for K and L shells. *Journal of Physical and Chemical Reference Data*, 8(2):307–327, April 1979.
- [48] H.A. Kramers and W. Heisenberg. Über die Streuung von Strahlung durch Atome.

- Zeitschrift für Physik*, 31(1):681–708, February 1925.
- [49] T. Brandenburg, M. Agaker, K. Atak, M. Pflüger, C. Schwanke, T. Petit, K.M. Lange, J.-E. Rubensson, and E.F. Aziz. The electronic structure of perfluorodecalin studied by soft X-ray spectroscopy and electronic structure calculations. *Physical Chemistry Chemical Physics*, 16(42):23379–23385, October 2014.
- [50] K. Atak, R. Golnak, J. Xiao, M. Pflüger, T. Brandenburg, B. Winter, and E.F. Aziz. Co(III) protoporphyrin IX chloride in solution: spin-state and metal coordination revealed from resonant inelastic X-ray scattering and electronic structure calculations. *Physical Chemistry Chemical Physics*, 17(5):3409–3414, January 2015.
- [51] Y. Zhao and D.G. Truhlar. Density Functional for Spectroscopy: No Long-Range Self-Interaction Error, Good Performance for Rydberg and Charge-Transfer States, and Better Performance on Average than B3lyp for Ground States. *The Journal of Physical Chemistry A*, 110(49):13126–13130, December 2006.
- [52] Y. Zhao and D.G. Truhlar. The M06 suite of density functionals for main group thermochemistry, thermochemical kinetics, noncovalent interactions, excited states, and transition elements: two new functionals and systematic testing of four M06-class functionals and 12 other functionals. *Theoretical Chemistry Accounts*, 120(1-3):215–241, July 2007.
- [53] P. Hohenberg and W. Kohn. Inhomogeneous Electron Gas. *Physical Review*, 136(3B):B864–B871, November 1964.
- [54] W. Kohn and L.J. Sham. Self-Consistent Equations Including Exchange and Correlation Effects. *Physical Review*, 140(4A):A1133–A1138, November 1965.
- [55] A.D. Becke. Density-functional exchange-energy approximation with correct asymptotic behavior. *Physical Review A*, 38(6):3098–3100, September 1988.
- [56] J.P. Perdew and Y. Wang. Accurate and simple analytic representation of the electron-gas correlation energy. *Physical Review B*, 45(23):13244–13249, June 1992.
- [57] A.D. Becke. Density functional thermochemistry. III. The role of exact exchange. *The Journal of Chemical Physics*, 98(7):5648–5652, April 1993.
- [58] E. Runge and E.K.U. Gross. Density-Functional Theory for Time-Dependent Systems. *Physical Review Letters*, 52(12):997–1000, March 1984.
- [59] A. Schäfer, H. Horn, and R. Ahlrichs. Fully optimized contracted Gaussian basis sets for atoms Li to Kr. *The Journal of Chemical Physics*, 97(4):2571–2577, August

- 1992.
- [60] F. Weigend and R. Ahlrichs. Balanced basis sets of split valence, triple zeta valence and quadruple zeta valence quality for H to Rn: Design and assessment of accuracy. *Physical Chemistry Chemical Physics*, 7(18):3297, 2005.
- [61] E.J. Baerends, D.E. Ellis, and P. Ros. Self-consistent molecular Hartree-Fock-Slater calculations I. The computational procedure. *Chemical Physics*, 2(1):41–51, September 1973.
- [62] B.I. Dunlap, J.W.D. Connolly, and J.R. Sabin. On some approximations in applications of theory. *The Journal of Chemical Physics*, 71(8):3396–3402, July 2008.
- [63] O. Vahtras, J. Almläf, and M.W. Feyereisen. Integral approximations for LCAO-SCF calculations. *Chemical Physics Letters*, 213(5-6):514–518, October 1993.
- [64] K. Eichkorn, O. Treutler, H. Öhm, M. Häser, and R. Ahlrichs. Auxiliary basis sets to approximate Coulomb potentials. *Chemical Physics Letters*, 240(4):283–290, June 1995.
- [65] K. Eichkorn, F. Weigend, O. Treutler, and R. Ahlrichs. Auxiliary basis sets for main row atoms and transition metals and their use to approximate Coulomb potentials. *Theoretical Chemistry Accounts*, 97(1-4):119–124, October 1997.
- [66] F. Weigend. Accurate Coulomb-fitting basis sets for H to Rn. *Physical Chemistry Chemical Physics*, 8(9):1057, 2006.
- [67] K.-J. Kim, S.V. Milton, and E. Gluskin. *Free Electron Lasers 2002: Proceedings of the 24th International Free Electron Laser Conference and the 9th FEL Users Workshop, Argonne, Illinois, U.S.A., September 9-13, 2002*. Elsevier Science & Technology, Amsterdam ; Boston, August 2003.
- [68] P. Wilmott. *An Introduction to Synchrotron Radiation: Techniques and Applications*. John Wiley and Sons, Ltd, 2011.
- [69] W.B. Peatman. *Gratings, Mirrors and Slits: Beamline Design for Soft X-Ray Synchrotron Radiation Sources*. Taylor & Francis Ltd, Amsterdam, April 1997.
- [70] D. Attwood. *Soft X-Rays and Extreme Ultraviolet Radiation*. Cambridge University Press, 1999.
- [71] N. Yamamoto, H. Zen, M. Hosaka, T. Konomi, M. Adachi, K. Hayashi, J. Yamazaki, Y. Takashima, and M. Katoh. Beam injection with pulsed multipole magnet at UVSOR-III. *Nuclear Instruments and Methods in Physics Research Section A: Accelerators, Spectrometers, Detectors and Associated Equipment*, 767:26–33, December 2014.

-
- [72] J. Larmor. LXIII. On the theory of the magnetic influence on spectra; and on the radiation from moving ions. *Philosophical Magazine Series 5*, 44(271):503–512, December 1897.
- [73] P.J. Nahin. *Oliver Heaviside: The Life, Work, and Times of an Electrical Genius of the Victorian Age*. JHU Press, October 2002.
- [74] M.R. Weiss, R. Follath, F. Senf, and W. Gudat. Comparative monochromator studies for a soft x-ray microfocus beamline for BESSY-II. *Journal of Electron Spectroscopy and Related Phenomena*, 101-103:1003–1012, June 1999.
- [75] T. Hatsui, E. Shigemasa, and N. Kosugi. Design of a transmission grating spectrometer and an undulator beamline for soft x-ray emission studies. In *AIP Conference Proceedings*, volume 705, pages 921–924. AIP Publishing, May 2004.
- [76] S.C. Leemann. *Detailed Design Report on the MAX IV Facility*. MAX-Lab, August 2010.
- [77] R. Reininger. The in-focus variable line spacing plane grating monochromator. *Nuclear Instruments and Methods in Physics Research Section A: Accelerators, Spectrometers, Detectors and Associated Equipment*, 649(1):139–143, September 2011.
- [78] H. Bluhm, K. Andersson, T. Araki, K. Benzerara, G.E. Brown, J.J. Dynes, S. Ghosal, M.K. Gilles, H.-Ch. Hansen, J.C. Hemminger, A.P. Hitchcock, G. Ketterer, A.L.D. Kilcoyne, E. Kneidler, J.R. Lawrence, G.G. Leppard, J. Majzlam, B.S. Mun, S.C.B. Myneni, A. Nilsson, H. Ogasawara, D.F. Ogletree, K. Pecher, M. Salmeron, D.K. Shuh, B. Tonner, T. Tylliszczak, T. Warwick, and T.H. Yoon. Soft X-ray microscopy and spectroscopy at the molecular environmental science beamline at the Advanced Light Source. *Journal of Electron Spectroscopy and Related Phenomena*, 150(2-3):86–104, February 2006.
- [79] B.L. Henke, E.M. Gullikson, and J.C. Davis. X-Ray Interactions: Photoabsorption, Scattering, Transmission, and Reflection at $E = 50\text{--}30,000$ eV, $Z = 1\text{--}92$. *Atomic Data and Nuclear Data Tables*, 54(2):181–342, July 1993.
- [80] M. Nagasaka, T. Hatsui, T. Horigome, Y. Hamamura, and N. Kosugi. Development of a liquid flow cell to measure soft X-ray absorption in transmission mode: A test for liquid water. *Journal of Electron Spectroscopy and Related Phenomena*, 177(2-3):130–134, March 2010.
- [81] M. Nagasaka, K. Mochizuki, V. Leloup, and N. Kosugi. Local Structures of Methanol-Water Binary Solutions Studied by Soft X-ray Absorption Spectroscopy. *The Journal of Physical Chemistry B*, 118(16):4388–4396, April 2014.

- [82] S. Eisebitt, T. Böske, J.-E. Rubensson, and W. Eberhardt. Determination of absorption coefficients for concentrated samples by fluorescence detection. *Physical Review B, Condensed Matter*, 47(21):14103–14109, June 1993.
- [83] M. Faubel and T. Kisters. Non-equilibrium molecular evaporation of carboxylic acid dimers. *Nature*, 339(6225):527–529, June 1989.
- [84] M. Faubel, S. Schlemmer, and J.P. Toennies. A molecular beam study of the evaporation of water from a liquid jet. *Zeitschrift für Physik D Atoms, Molecules and Clusters*, 10(2-3):269–277, June 1988.
- [85] K.M. Lange, A. Kothe, and E.F. Aziz. Chemistry in solution: recent techniques and applications using soft X-ray spectroscopy. *Physical chemistry chemical physics: PCCP*, 14(16):5331–5338, April 2012.
- [86] C. Weber. Zum Zerfall eines Flüssigkeitsstrahles. *ZAMM - Journal of Applied Mathematics and Mechanics / Zeitschrift für Angewandte Mathematik und Mechanik*, 11(2):136–154, January 1931.
- [87] H.A. Rowland. XXXIX. Gratings in theory and practice. *Philosophical Magazine Series 5*, 35(216):397–419, May 1893.
- [88] K.M. Lange, R. Könnecke, S. Ghadimi, R. Golnak, M.A. Soldatov, K. F. Hodeck, A. Soldatov, and E.F. Aziz. High resolution X-ray emission spectroscopy of water and aqueous ions using the micro-jet technique. *Chemical Physics*, 377(1-3):1–5, November 2010.
- [89] K.M. Lange, R. Könnecke, M. Soldatov, R. Golnak, J.-E. Rubensson, A. Soldatov, and E.F. Aziz. On the Origin of the Hydrogen-Bond-Network Nature of Water: X-Ray Absorption and Emission Spectra of Water-Acetonitrile Mixtures. *Angewandte Chemie*, 123(45):10809–10813, November 2011.
- [90] O. Plashkevych, L. Yang, O. Vahtras, H. Agren, and L.G.M. Pettersson. Substituted benzenes as building blocks in near-edge X-ray absorption spectra. *Chemical Physics*, 222(2-3):125–137, October 1997.
- [91] R. Manne. Molecular Orbital Interpretation of X-Ray Emission Spectra: Simple Hydrocarbons and Carbon Oxides. *The Journal of Chemical Physics*, 52(11):5733–5739, June 1970.
- [92] E.Z. Kurmaev, V.R. Galakhov, S. Shimada, T. Otsuka, K. Endo, S. Stadler, D.L. Ederer, A. Moewes, H. Schuerman, M. Neumann, S. Tomiyoshi, N. Azuma, and M. Iwami. Soft-x-ray fluorescence study of the quasi-one-dimensional Heisenberg antiferromagnet tetraphenylverdazyl. *Physical Review B*, 62(23):15660–15665, De-

- cember 2000.
- [93] A.P. Hitchcock, D.C. Newbury, I. Ishii, J. Stöhr, J.A. Horsley, R.D. Redwing, A.L. Johnson, and F. Sette. Carbon K-shell excitation of gaseous and condensed cyclic hydrocarbons: C₃H₆, C₄H₈, C₅H₈, C₅H₁₀, C₆H₁₀, C₆H₁₂, and C₈H₈. *The Journal of Chemical Physics*, 85(9):4849–4862, November 1986.
- [94] E.P. Wesseler, R. Iltis, and L.C. Clark Jr. The solubility of oxygen in highly fluorinated liquids. *Journal of Fluorine Chemistry*, 9(2):137–146, February 1977.
- [95] R.A.L. Vallee, G.J. Vancso, N.F. van Hulst, J.-P. Calbert, J. Cornil, and J.L. Brädas. Molecular fluorescence lifetime fluctuations: on the possible role of conformational effects. *Chemical Physics Letters*, 372(1-2):282–287, April 2003.
- [96] J. Israelachvili. *Intermolecular and Surface Forces*. Academic Press, 3rd edition edition, 2011.
- [97] R. Flesch, N. Kosugi, I.L. Bradeanu, J.J. Neville, and E. Rühl. Cluster size effects in core excitons of 1s-excited nitrogen. *The Journal of Chemical Physics*, 121(17):8343–8350, November 2004.
- [98] L. Salem. Attractive Forces between Long Saturated Chains at Short Distances. *The Journal of Chemical Physics*, 37(9):2100–2113, November 1962.
- [99] F. Sette, J. Stöhr, and A.P. Hitchcock. Determination of intramolecular bond lengths in gas phase molecules from K shell shape resonances. *The Journal of Chemical Physics*, 81(11):4906–4914, December 1984.
- [100] A.P. Hitchcock and I. Ishii. Carbon K-shell excitation spectra of linear and branched alkanes. *Journal of Electron Spectroscopy and Related Phenomena*, 42(1):11–26, January 1987.
- [101] M. Nagasaka, T. Hatsui, H. Setoyama, E. Rühl, and N. Kosugi. Inner-shell spectroscopy and exchange interaction of Rydberg electrons bound by singly and doubly charged Kr and Xe atoms in small clusters. *Journal of Electron Spectroscopy and Related Phenomena*, 183(1-3):29–35, January 2011.
- [102] X. Ma and F. Wang. Gamma-ray spectra of hexane in gas phase and liquid phase. *arXiv:1211.0097 [astro-ph, physics:physics, physics:quant-ph]*, November 2012. arXiv: 1211.0097.
- [103] F. London. The general theory of molecular forces. *Transactions of the Faraday Society*, 33(0):8b–26, January 1937.
- [104] F. London. Zur Theorie und Systematik der Molekularkräfte. *Zeitschrift für Physik*, 63(3-4):245–279, March 1930.

- [105] J. Stöhr. *NEXAFS Spectroscopy*, volume 25 of *Springer Series in Surface Sciences*. Springer Berlin Heidelberg, Berlin, Heidelberg, 1992.
- [106] K. Fukui, T. Yonezawa, and H. Shingu. A Molecular Orbital Theory of Reactivity in Aromatic Hydrocarbons. *The Journal of Chemical Physics*, 20(4):722–725, April 1952.
- [107] P. Glans, R.E. La Villa, Y. Luo, H. Agren, and J. Nordgren. X-ray emission spectroscopy measurements of fluorine substituted methanes. *Journal of Physics B: Atomic, Molecular and Optical Physics*, 27(15):3399, August 1994.
- [108] J. Guo, P. Resnick, K. Efimenko, J. Genzer, and J.M. DeSimone. Alternative Fluoropolymers to Avoid the Challenges Associated with Perfluorooctanoic Acid. *Industrial & Engineering Chemistry Research*, 47(3):502–508, 2007.
- [109] L.J. Gamble, B. Ravel, D.A. Fischer, and D.G. Castner. Surface Structure and Orientation of PTFE Films Determined by Experimental and FEFF8-Calculated NEXAFS Spectra. *Langmuir*, 18(6):2183–2189, 2002.
- [110] A. Tressaud, E. Durand, C. Labrugere, A.P. Kharitonov, and L.N. Kharitonova. Modification of surface properties of carbon-based and polymeric materials through fluorination routes: From fundamental research to industrial applications. *Journal of Fluorine Chemistry*, 128(4):378–391, April 2007.
- [111] R.G. Haverkamp and B.C.C. Cowie. C K-edge NEXAFS study of fluorocarbon formation on carbon anodes in molten NaF-AlF-CaF₂. *Surface and Interface Analysis*, 45(13):1854–1858, 2013.
- [112] S. Eisebitt, T. Böske, J.-E. Rubensson, and W. Eberhardt. Determination of absorption coefficients for concentrated samples by fluorescence detection. *Physical Review B*, 47(21):14103–14109, June 1993.
- [113] J. Jaklevic, J.A. Kirby, M.P. Klein, A.S. Robertson, G.S. Brown, and P. Eisenberger. Fluorescence detection of exafs: Sensitivity enhancement for dilute species and thin films. *Solid State Communications*, 23(9):679–682, September 1977.
- [114] K. Ueda, Y. Shimizu, H. Chiba, M. Okunishi, K. Ohmori, Y. Sato, E. Shigemasa, and N. Kosugi. C 1s and F 1s photoabsorption and subsequent electronic decay of CH₄, CH₃F, CH₂F₂, CHF₃, and CF₄. *Journal of Electron Spectroscopy and Related Phenomena*, 79:441–444, May 1996.
- [115] A.W. Hofmann. On Insolinic Acid. *Proceedings of the Royal Society of London*, 8:1–3, January 1856.

8 Appendix

8.1 Benzene Calculations with Different Parameter Configurations

As discussed in chapter 3.2 regarding the basics of theoretical modelling, investigations into different basis sets and functional methods are necessary to find the best fitting theoretical configuration. The primary functional method found in literature is the B3LYP hybrid functional [57]. It provides fitting postulations with acceptable computation time. The basis sets are the second important piece. In this work the Ahlrich basis set compilation was employed as it is one of the best fitting for hydrocarbon calculations [59, 60].

In a direct comparison of the different levels of basis set depth (see Fig. 8.1), its evident that especially the def2-TZVP and higher level sets are the best performing. Under consideration of appropriate computation times, the def2-TZVP basis set was chosen as it incorporates sufficient accuracy and a computation time of several hours (QZVP had several days for equal calculations).

The second step was to observe the differences in functionals as the basis set is fixed (see Fig. 8.1). Taking literature comparisons of different functionals into account, the M06 functional [51] was discovered as one of the most promising functional sets for hydro- and fluorocarbon calculations [52].

My observations indeed confirmed this performance, leading to the best theoretical predictions if the M06 functional was employed together with the def2-TZVP basis set. Lastly, the def2-TZVP (-f) sub-set was chosen from the wide range of def2-TZVP sub-sets, as it includes descriptions up to d-orbital character, which is sufficient for carbon and fluorine based theoretical predictions.

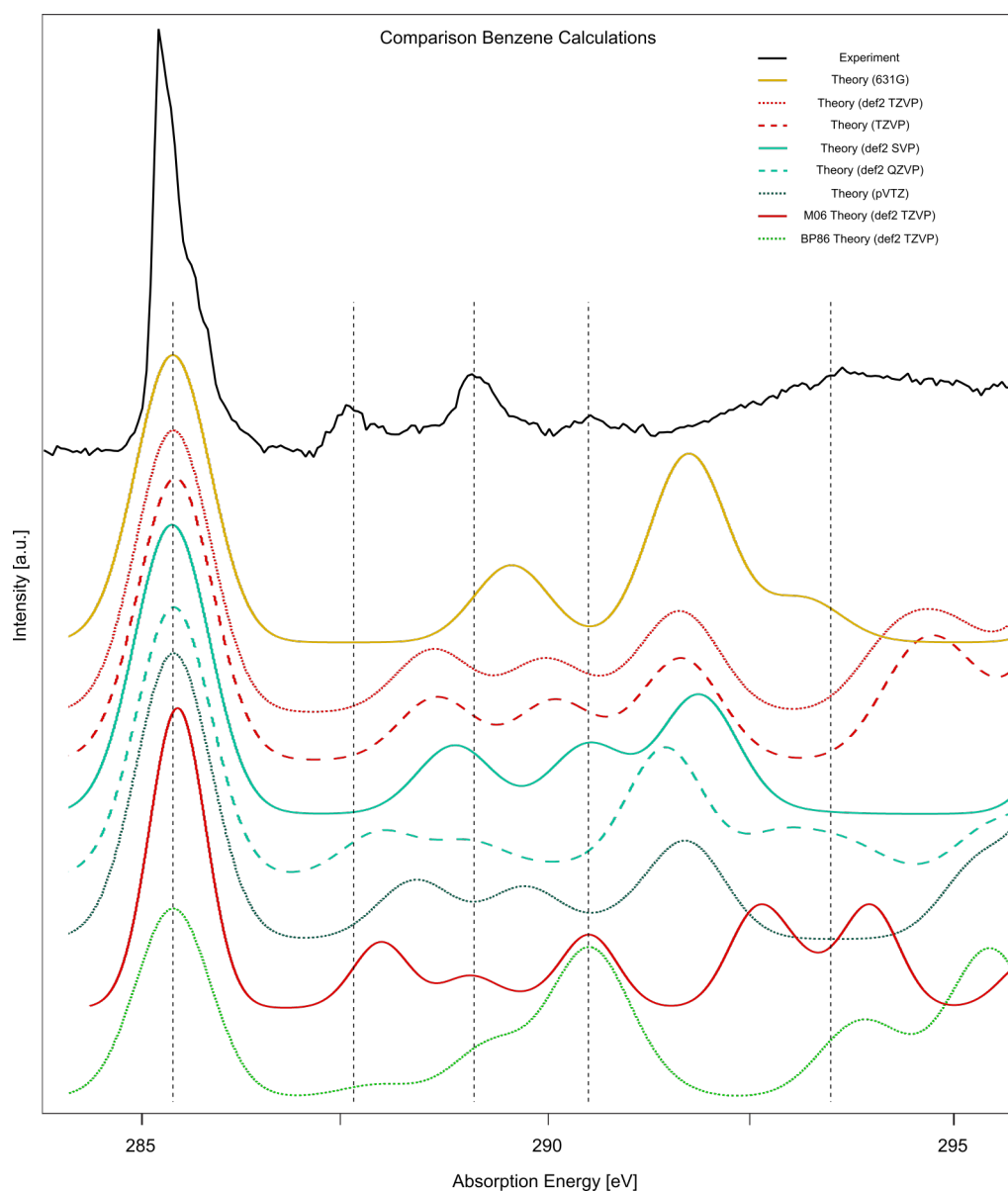


Figure 8.1: **Benzene Calculations with Different Parameter Configurations:** Different theoretical predictions are underlining the experimental spectrum of benzene. When not denoted otherwise, the calculations were performed employing the B3LYP hybrid functional. Dashed lines indicate the appropriate energetic positions of the experimental features. The different levels of theory (basis sets and functionals) show significant spectral differences, with the best fitting spectrum utilizing the def2-TZVP basis set and M06 hybrid functional.

8.2 Supplementary Materials from the Contributed Articles

8.2.1 Impacts of Conformational Geometries in Fluorinated Alkanes

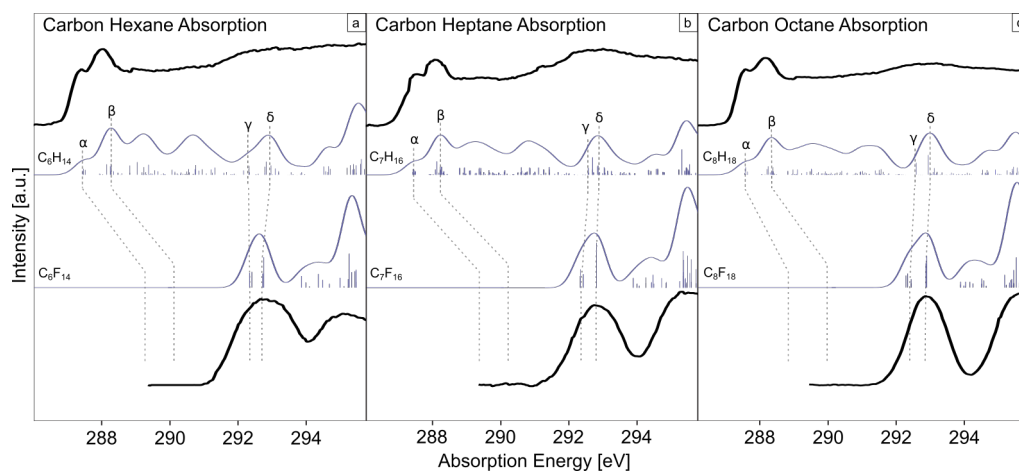


Figure 8.2: **Impacts of Conformational Geometries in Fluorinated Alkanes - Sup1:** Experimental (black lines) and calculated (blue lines and transition bars) carbon K-edge X-ray absorption spectra for hexane (a), heptane (b), octane (c) and their respective fluorinated compounds. Dashed lines indicate the shifts of the spectral features. [46]

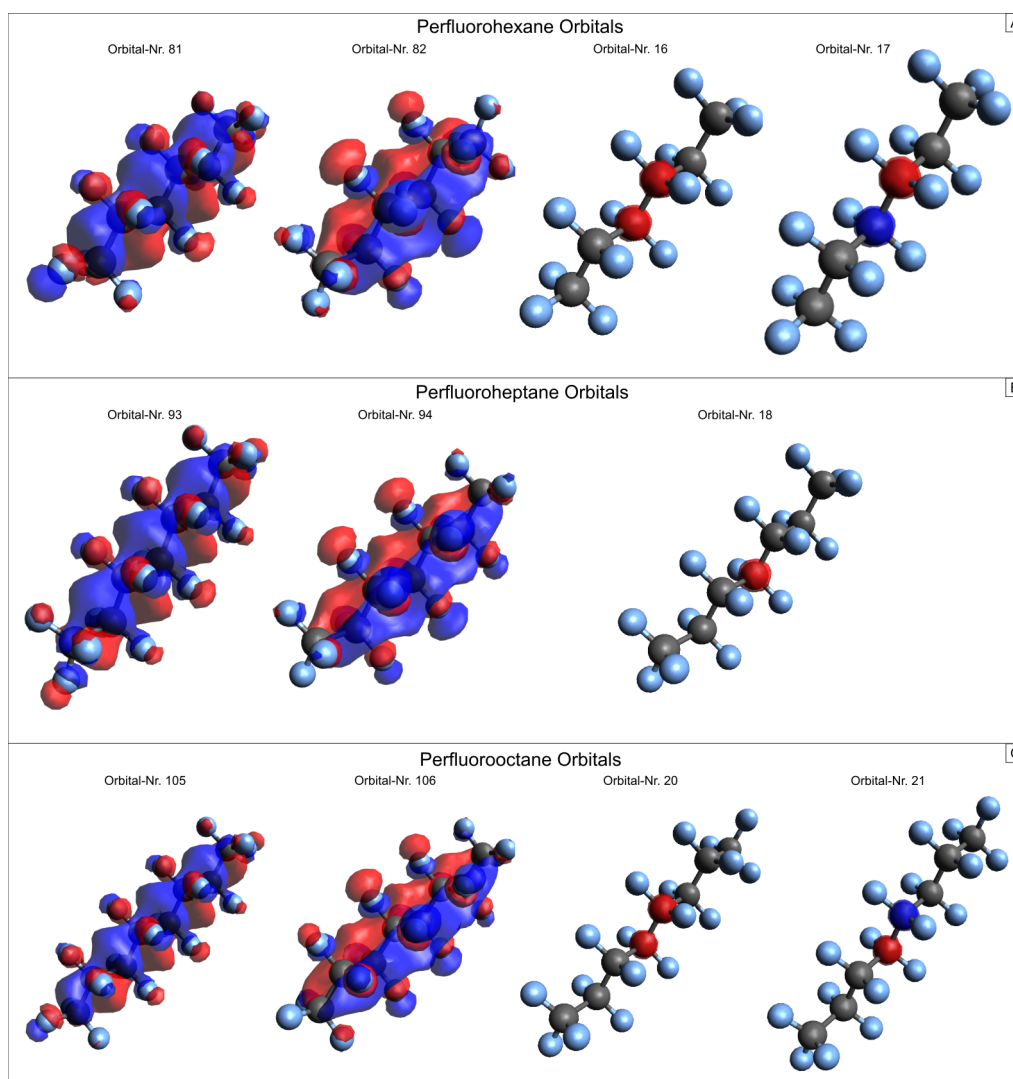


Figure 8.3: **Impacts of Conformational Geometries in Fluorinated Alkanes - Sup2:** Molecular orbitals involved in the main resonance of the perfluorocarbon X-ray absorption spectra at 292.8 eV. Similar orbitals can be found for each molecule. The core orbitals represent the innermost carbon atoms (for even number of (CF_2) -chains two carbons, for uneven number of (CF_2) -chains one carbon). The unoccupied orbitals represent π_z (C-C) and π_x (C-C) resonances. [46]

8.2.2 Fluorination-Dependent Molecular Orbital Occupancy in Ring-Shaped Perfluorocarbons

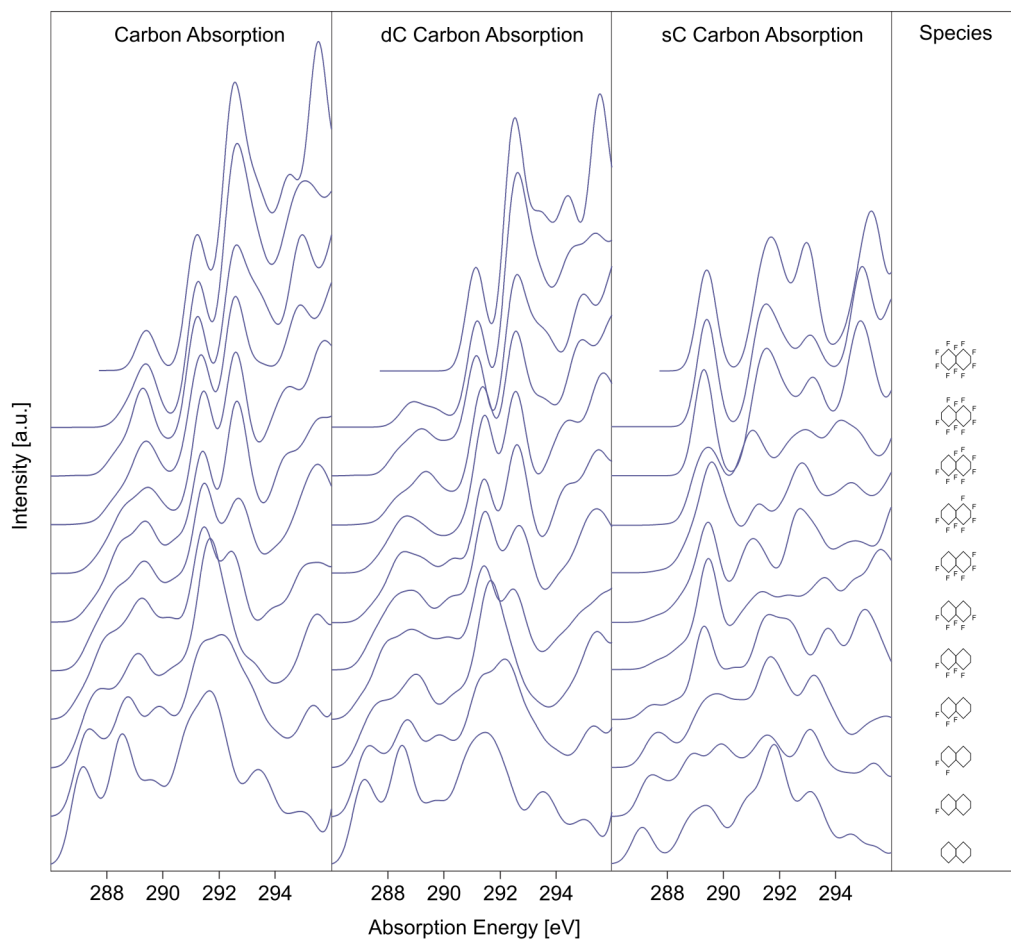


Figure 8.4: **Fluorination-Dependent Molecular Orbital Occupancy in Ring-Shaped Perfluorocarbons - Sup1:** Carbon K-edge absorption calculations for all fluorination stages between decalin and PFD. [46]

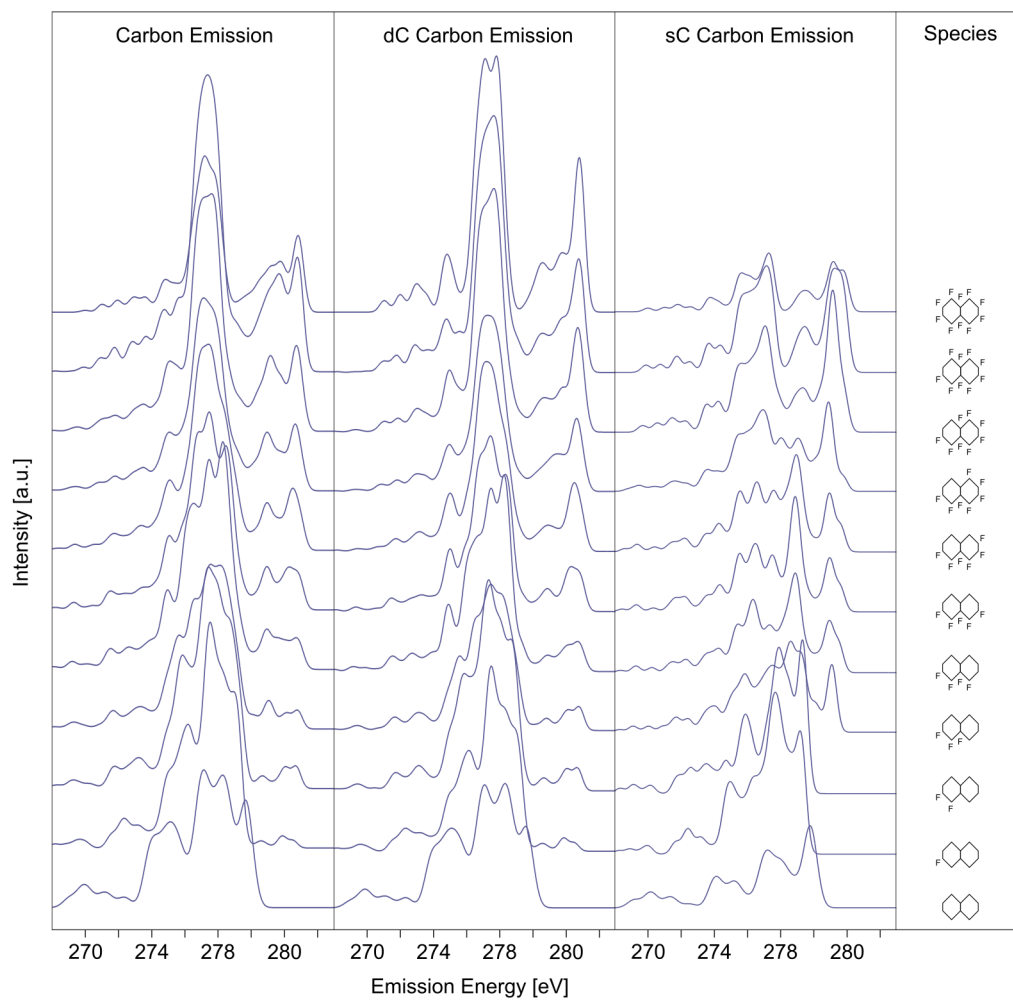


Figure 8.5: **Fluorination-Dependent Molecular Orbital Occupancy in Ring-Shaped Perfluorocarbons - Sup2:** Carbon K-edge emission calculations for all fluorination stages between decalin and PFD. [46]

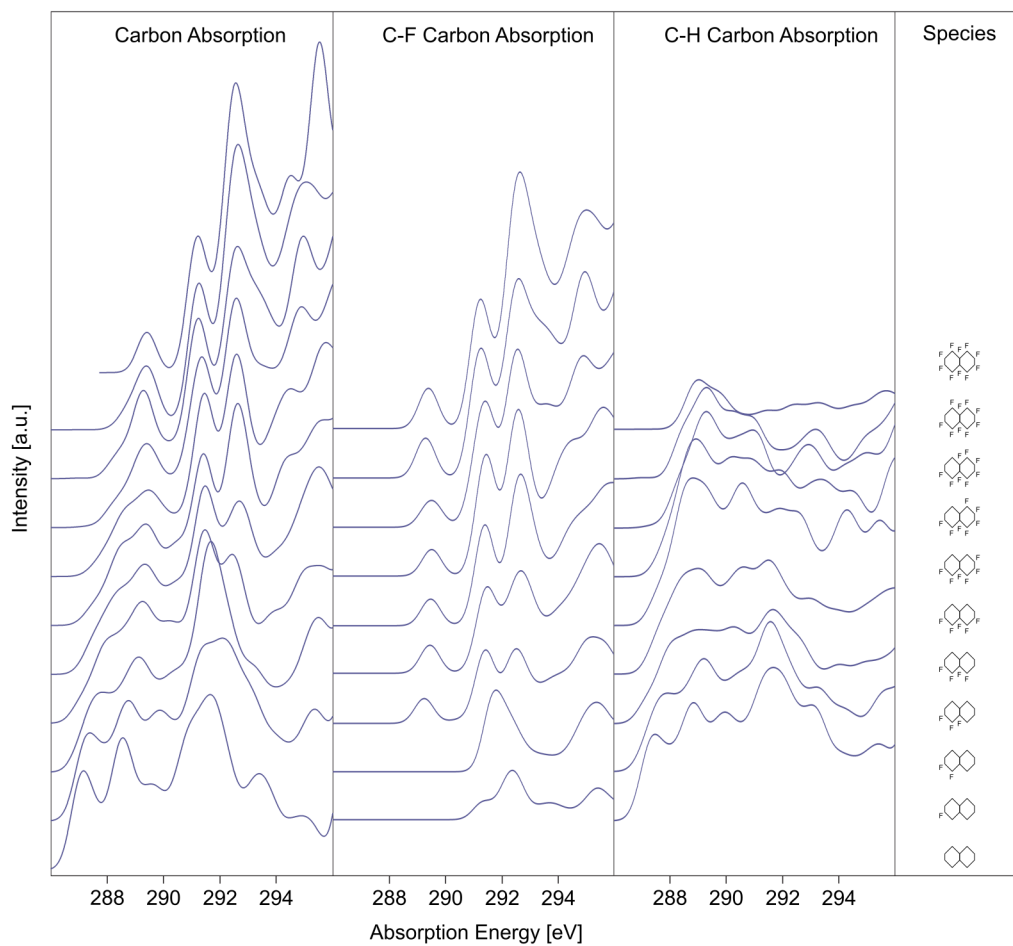


Figure 8.6: **Fluorination-Dependent Molecular Orbital Occupancy in Ring-Shaped Perfluorocarbons - Sup3:** Carbon K-edge absorption calculations for all fluorination stages between decalin and PFD, separated in absorption spectra of carbons with fluorine nearest neighbours and carbons with hydrogen nearest neighbours. [46]

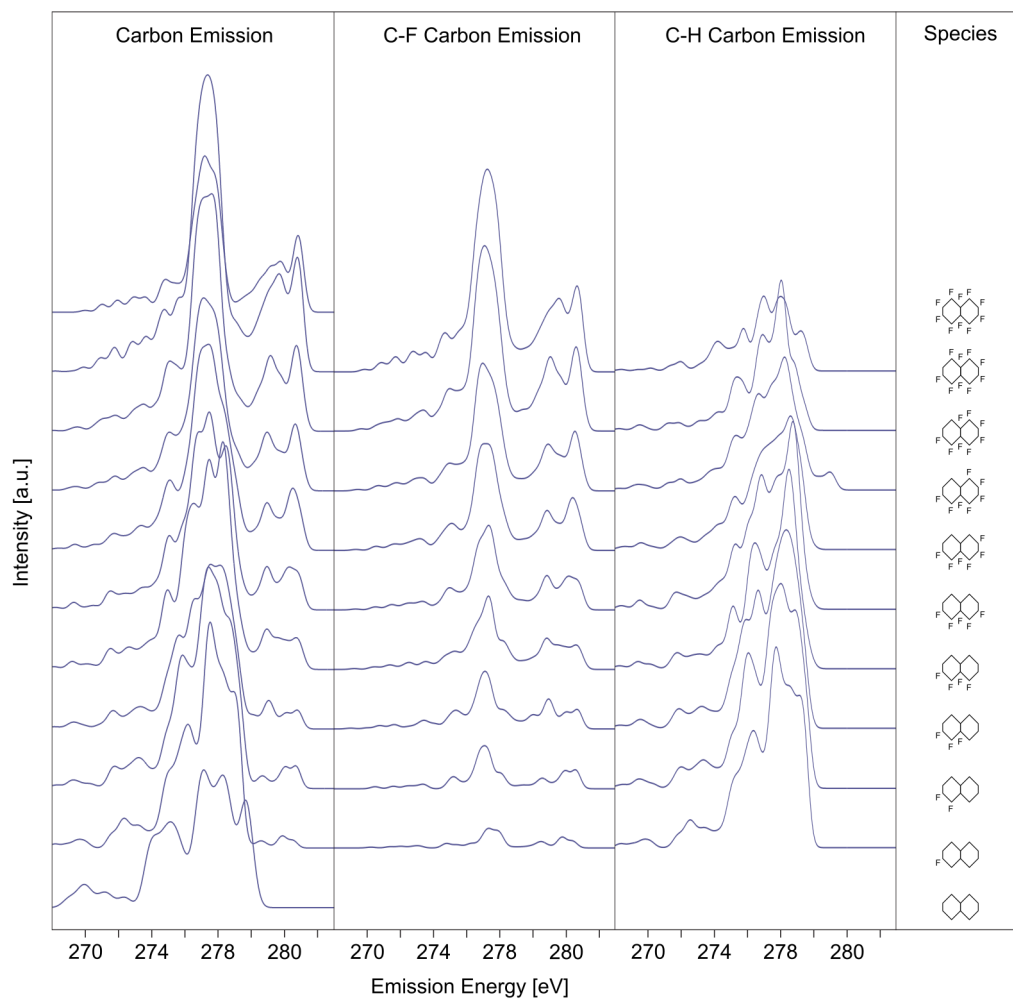


Figure 8.7: **Fluorination-Dependent Molecular Orbital Occupancy in Ring-Shaped Perfluorocarbons - Sup4:** Carbon K-edge emission calculations for all fluorination stages between decalin and PFD, separated in emission spectra of carbons with fluorine nearest neighbors and carbons with hydrogen nearest neighbors. [46]

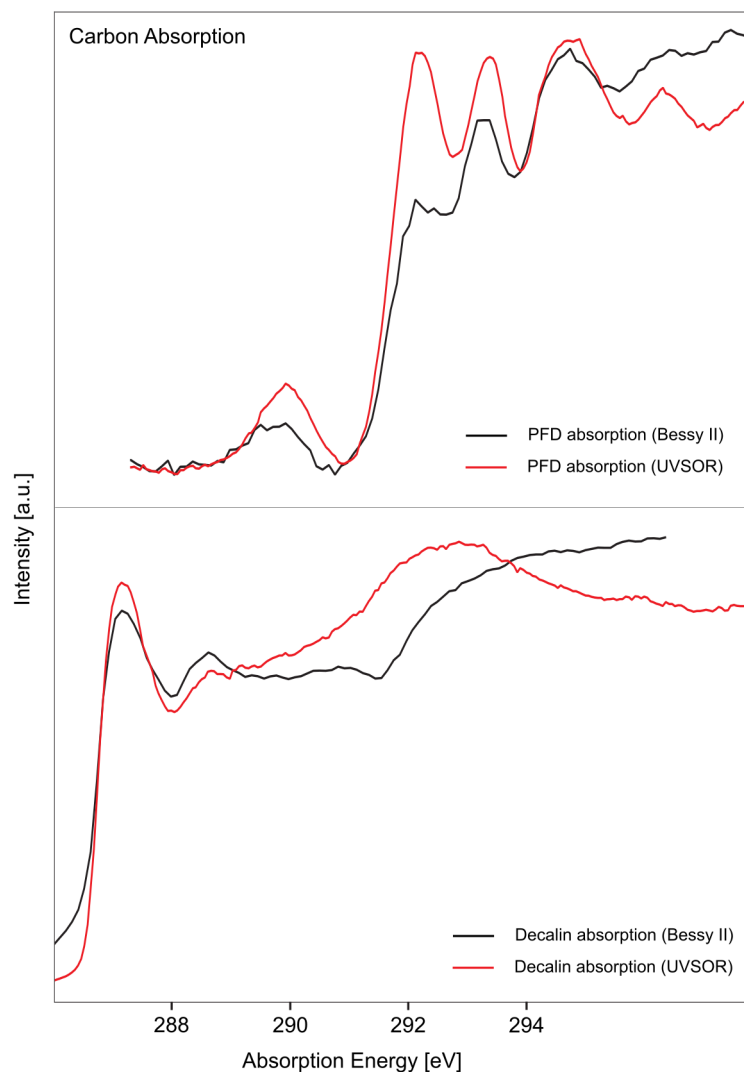


Figure 8.8: **Fluorination-Dependent Molecular Orbital Occupancy in Ring-Shaped Perfluorocarbons - Sup5:** Comparison of absorption spectra obtained at both Synchrotron facilities (Bessy II and UVSOR). The spectra obtained at Bessy show clear effects of self-saturation, which result from the technique used to obtain these spectra (Total Fluorescence Yield). To circumvent this effect, another technique (Transmission) was employed where self-saturation effects do not occur. [46]

8.2.3 The Electronic Structure of Perfluorodecalin studied by Soft X-Ray Spectroscopy and Electronic Structure Calculations

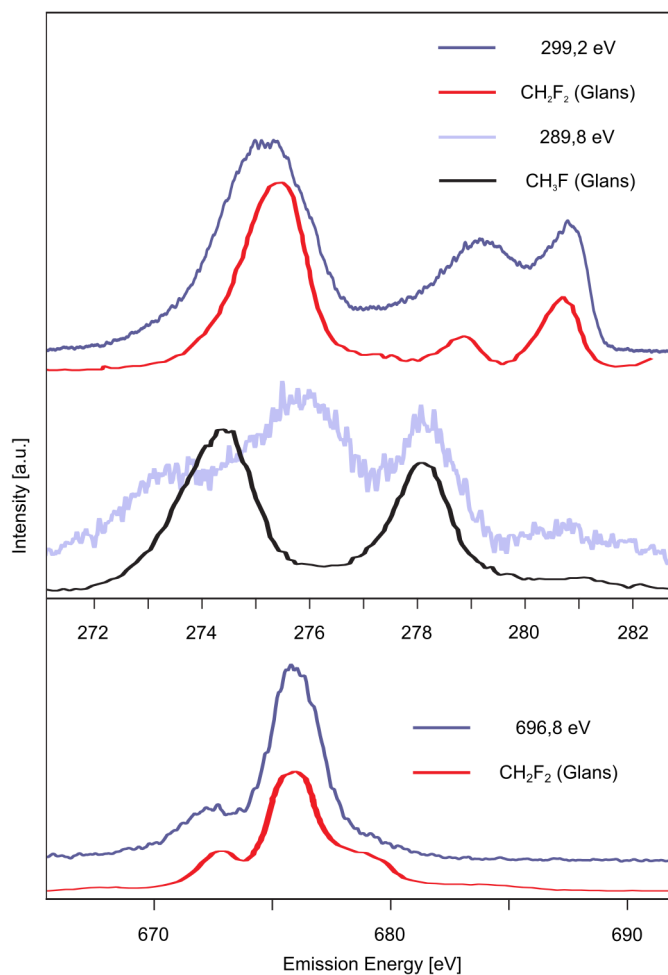


Figure 8.9: **The Electronic Structure of Perfluorodecalin studied by Soft X-Ray Spectroscopy and Electronic Structure Calculations - Sup1:** Perfluorodecalin carbon and fluorine K-edge emission compared to gas phase reference data of fluoromethanes [107]. The reference data was shifted by 2.3 eV to fit with the experimental features. Comparison shows striking resemblance between reference and experimental data. [49]

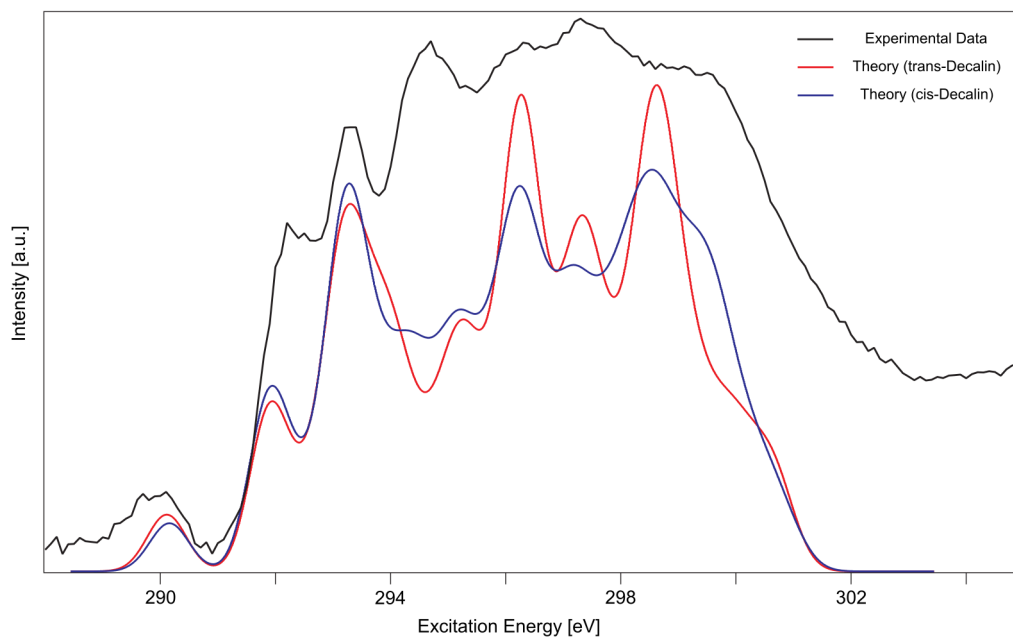


Figure 8.10: **The Electronic Structure of Perfluorodecalin studied by Soft X-Ray Spectroscopy and Electronic Structure Calculations - Sup2:** Perfluorodecalin carbon K-edge absorption compared to theoretical data of trans- and cis-PFD (see Fig. 5.11). Both isomers exhibit similar spectra concerning peak positions and intensity. Therefore, a discussion of the influence of either isomer is not needed. [49]

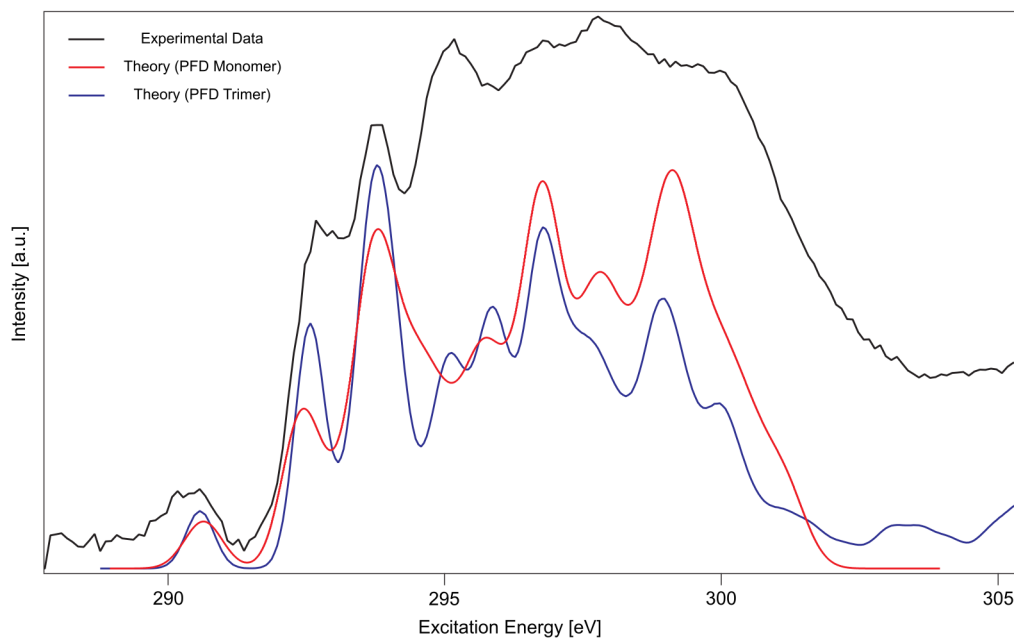


Figure 8.11: **The Electronic Structure of Perfluorodecalin studied by Soft X-Ray Spectroscopy and Electronic Structure Calculations - Sup3:** Perfluorodecalin carbon K-edge absorption compared to theoretical calculations of monomer and trimer configurations. Both configurations exhibit similar spectra concerning peak positions and intensity. [49]

Acknowledgments

In this chapter I'd like to give honorary mentions for everyone who supported me in the process of creating this work.

Special thanks go to Prof. Emad F. Aziz for the chance to write this interesting work in his group and providing me with opportunities for conferences and experiments outside of BESSY. Another special mention will be given to Prof. Jan-Erik Rubensson, who accepted to be my second examiner and is the main starting point of this work through his experimental suggestions and idea of investigating perfluorocarbons.

I'd also like to thank Prof. Nobuhiro Kosugi for the experimental opportunities given to me at his beamline in Japan.

A big help in the three years were Dr. Kaan Atak and Dr. Ronny Golnak who supported me in experiments, article writing and every other possible way. Special thanks also for the great help in the articles and times long forgotten.

Special mentions should also go to Dr. Iain Wilkinson and Sreeju Sreekantan Nair Lalithambika (long name ... I know) for their help, as they were forced to listen to my complains and cries of help through sitting in the same office. Special thanks also goes to Maha Dürr for introducing myself to bouldering, a sport I will hopefully enjoy for a long time.

Additional thanks go to the group of Prof. Kosugi and the UVSOR team, especially Dr. Masanari Nagasaka for his support in the Japanese beamtimes.

I'd also like to thank the group of Prof. Aziz and the BESSY team for their support, with special mentioning to Dr. Jie Xiao, Daniela Schön, Dr. Tristan Petit, Dr. Marc Tesch and several more whose name I may have forgotten.

Eidesstattliche Erklärung

Hiermit versichere ich, Tim Brandenburg, die vorliegende Dissertation mit dem Titel "The Electronic Structure of Fluorinated Systems in the Liquid Phase" selbständig und ohne unerlaubte Hilfe angefertigt zu haben. Bei der Verfassung der Dissertation wurden keine anderen als die im Text aufgeführten Hilfsmittel verwendet.

Ein Promotionsverfahren zu einem früheren Zeitpunkt an einer anderen Hochschule oder bei einem anderen Fachbereich wurden nicht beantragt.

Berlin, den 24.01.2017

Tim Brandenburg